Understanding Thickness Dependent Magnetic Properties of Ultra-Thin Films

A Dissertation Presented

by

Kathryn Lynn Krycka

to

The Graduate School

in Partial Fulfillment of the Requirements

for the Degree of

Doctor of Philosophy

in

Physics

Stony Brook University

August 2007

StonyBrookUniversity

The Graduate School

Kathryn Lynn Krycka

We, the dissertation committee for the above candidate for the Doctor of Philosophy degree, hereby recommend acceptance of the dissertation.

Chi-Chang Kao - Advisor
Professor, Department of Physics and Astronomy
Senior Scientist, Brookhaven National Laboratory

Christopher Jacobsen - Chairperon
Professor, Department of Physics and Astronomy

Philip Allen
Professor, Department of Physics and Astronomy

Kenneth Evans-Lutterodt
Senior Scientist, Physics, Brookhaven National Laboratory

This dissertation is accepted by the Graduate School.

Lawrence Martin
Dean of the Graduate School

Abstract of the Dissertation

Understanding Thickness Dependent Magnetic Properties of Ultra-Thin Films

by

Kathryn Lynn Krycka

Doctor of Philosophy

in

Physics

Stony Brook University

2007

Spin-transfer devices utilize both the charge and spin nature of electron transport and show great promise for highly compact magnetic memory. The degree to which spin-polarized transport can proceed, characterized by magnetic Gilbert damping, is strongly dependent on the thickness of the ferromagnetic layer(s) involved. However, without detailed knowledge of the ferromagnetic structure it is very difficult to distinguish between magnetic damping related to interface effects and to intrinsic magnetocrystalline anisotropy changes.

As layered systems become ultra-thin, x-ray diffraction becomes more challenging due to Debye broadening and to the often polycrystalline nature of ultra-thin films. Additionally, ultra-thin layers can acquire both induced strain and produce significant interlayer interference not normally observed in thicker samples. The combination of these effects can cause the Bragg peaks of two distinct, but closely lattice matched layers to significantly overlap. Motivated by the need for a general, minimal assumption method to handle such situations, multi-energy, element sensitive anomalous diffraction has been developed. It was successfully applied to solve the structure and trigonal strain of single cobalt layers 12 to 65 $\AA$ thick buried within a Pt|Cu|Co|Cu|Pt structure. The method is sensitive to texture and lattice spacing of $\pm$ 0.01 $\AA$. The anomalous results are compared with extended x-ray absorption fine structure (EXAFS) measurements.

Magnetic orbital and spin moments examined with x-ray magnetic circular dichroism (XMCD) are correlated with the strain induced structural distortion measured. In Co ultra-thin films the trigonal strain appears to be responsible for the increased orbital to spin moment ratio observed far a range of ultra-thin film thicknesses. In t Co$|2t$ Ni multilayers the strain is great enough to potentially negate the perpendicular magnetic anisotropy associated with the enhancement of Co to Ni interface in ultrathin layers with $t = 4\ \AA$ or less. In both cases combining detailed structural characterization with magnetic spectroscopy proves to be a powerful approach in understanding the origin of magnetic behavior.

To my parents and husband whose unending support has made this possible

Contents

List of Figures

List of Tables

Acknowledgements

To my advisor, Chi-Chang Kao, thank you for all your support and frank discussions over the past years! I've truly enjoyed the freedom you gave me to try out my ideas (even the less than great ones). You've taught me so much about the way to approach a project, planning for the future, and making contacts. It's always amazed me that whenever I've had a question you always knew exactly which paper, or even person, to refer to. Thank you for always making time for me in your busy schedule when I needed it, and in helping prepare me for a career after graduate school.

The environment created by so many supportive, creative, and energetic people here at the National Synchrotron Light Source has been wonderful. I owe thanks to many, but in particular I wish to acknowledge Cecilia Sanchez-Hanke, Joe Dvorak, Dario Arena, Steve Hulbert, and Ken Evans-Lutterodt for answering many questions and pointing me in the right direction on numerous occasions. Elaine DiMasi, thank you so much for your patience while I repeatedly took beamtime at X6B in learning about anomalous interference and getting my method to finally work out! Joe Woicik, Peter Stephens, Jae-Hyuk Her, Christie Nelson, James Abblett, and Wolfgang Calibe thank you for the extra experimental time and help you've given me. A special thank you to Doug Robinson, Philip Ryan, and Joe Dvorak for putting in extra effort at 6-ID-D and U4B, and helping make those last needed measurements happen! And thanks to the many others who have offered friendship, scientific knowledge, and a helping hand freely.

To my sample providers and collaborators, Andrew Kent, Jean-Marc Beaujour, Sarah Majetich, and Madhur Sanchan, thank you so much for the high quality samples. I have really appreciated your willingness to include me in your research, and for your responsiveness and the extra effort of producing tailor-made samples that I could best use. Without your help the work completed within this dissertation truly would not have been possible!

I wish to thank my parents for their unconditional support and for the many, many hours you've listened to all the small exciting successes and the depressing disappointments along the way. You have been a much needed sounding board more times than I can count.

To my husband, Cosmin, I thank you for being my pillar of support. Your unwavering confidence in me, and in us, has been invaluable.

The majority of the work contained within this dissertation was performed at the National Synchrotron Light Source beamlines U4B, X6B, X16B, X16C, and X23A. Use of the National Synchrotron Light Source, Brookhaven National Laboratory, was

supported by the US department of energy, office of science, office of basic energy sciences, under Contract No. DE-AC02-98CH10886.

A key set of experiments were taken at 6-ID-B at the Advanced Photon Source. Use of the Advanced Photon Source was supported by the US department of energy, office of science, office of basic energy sciences, under Contract No. DE-AC02-06CH11357.

Chapter 1

Overview

1.1 Top-Down Motivation

In attaining the eventual goal of creating magnetic memory on the order of terabytes per square inch, ever-shrinking devices of increased density face challenges associated with the ability to reproducibly pattern and subsequently address individual bits. These devices must also provide the control required to magnetically switch a single desired bit while leaving its neighbors unperturbed. In response many unique solutions have been proposed that include (but are not limited to) manipulating of electronic spin states in order to increase possible bit values beyond bilateral zeros and ones (quantum computing), patterning of self-assembled ultra-small core-shell magnetic nanospheres or inert viral cages filed with magnetic materials of interest, and better lithographical patterning of various nanoshape arrays. Additionally, the spin-polarized nature of electrons has been utilized along with their conventional charge properties in a growing field known as spintronics [1].

Spin-torque devices rely heavily on the fact that ferromagnetic materials can take on roles as both spin current polarizers and spin filters. Figure 1.1 shows a typical arrangement consisting of a thicker, fixed ferromagnetic layer separated from a thinner, free ferromagnetic layer by a nonmagnetic conducting region. The conducting region's purpose is to allow spin transfer to take place between the ferromagnetic layers, while physically separating them such that the magnetic orientation of the thinner layer may differ from the thicker ferromagnet. This fixed ferromagnetic layer takes on the role of a spin polarizer, while the direction of magnetization of the thinner layer dictates which spin orientation is preferentially scattered over the other (*i.e.* the thinner ferromagnet becomes a spin filter). The net spin flip at the interface of the thinner ferromagnetic creates a magnetic torque of the form [2]

$$\frac{d\vec{m}_{\text{thin}}}{dt} \propto \frac{\zeta I}{\vec{m}_{\text{thin}}} \times (\vec{m}_{\text{thin}} \times \vec{m}_{\text{thick}}), \tag{1.1}$$

where $\vec{m}_{\text{thin}}$ and $\vec{m}_{\text{thick}}$ represent the directions of the net respective ferromagnetic spin (magnetic) orientations, and I is the applied spin current. ζ is a scalar function of the natural spin polarization within the ferromagnets and determines the degree of spin transfer. Referring again to Figure 1.1, a current polarized perpendicular to

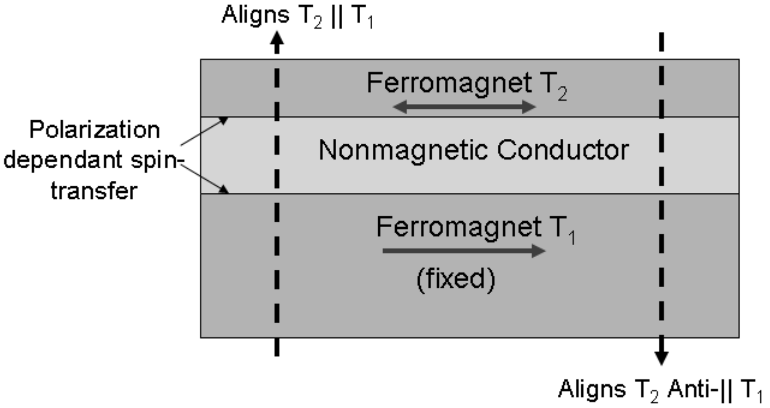

Figure 1.1: Current Perpendicular to Plane Spin-Torque Schematic. Current becomes partially spin polarized during passage through a thicker, fixed ferromagnetic layer (refer to left hand side). Due to preferential scattering of one spin polarization over another at the interface of second, thinner ferromagnetic layer a magnetic torque is created. If the spin-torque is sufficiently strong spin reorientation of the thinner layer can occur, aligning it with the thicker reference layer. Current reversal has the opposite effect and tends to align the free ferromagnetic layer anti-parallel to the reference ferromagnet (refer to right hand side).

the interface plane and passing from the fixed ferromagnetic into the free region has the tendency to align the two regions, while the opposite flow drives the free layer toward an anti-ferromagnetic orientation with respect to the fixed ferromagnet. Thus, two magnetic configurations could in principle be achieved solely by application of an electric current rather than by brute magnetic force. This would greatly reduce the likelihood of accidental perturbation and unintended switching of nearest neighbor bits. In addition the magnetic orientation of the free layer can also be probed electrically as a function of giant magneto resistance.

So far an idealized system has been described where no polarization loss or magnetic damping occurs. A better representation of the situation is given by the Landau-Lifshitz-Gilbert equation of motion,

$$\frac{d\vec{m}}{dt} = -\gamma\left(\vec{m} \times \vec{H}_{\text{eff}}\right) + \frac{G}{\gamma M_{\text{sat}}}\left(\vec{m} \times \frac{d\vec{m}}{dt}\right). \tag{1.2}$$

As before $\vec{m}$ represents the direction of magnetization, γ is the gyromagnetic ratio, H_{eff} is the applied field minus sample demagnetization, and M_{sat} is the magnetic saturation value. The first term of the right hand side indicates that a perturbed magnetic moment precesses at the Larmor frequency until fully damped into a static condition. The second term on the right hand side has a similar structure to equation 1.1, and this reflects the fact that both spin-pumping and viscous-like magnetic damping play a part in determining the net magnetic torque experienced by the free ferromagnetic layer. The two effects can be lumped together into a combined scalar term, G, coined Gilbert damping. An important point to notice is that only when a critical current threshold is met or exceeded will the magnetic torque be sufficient for magnetic reorientation to occur.

The mechanism of spin-pumping as discussed above was first proposed in 1996 by Slonczewski [2] and Berger [3]. Yet, the exact nature of spin-pumping and the related (also more easily observed) magnetic damping isn't fully resolved. Although considerable evidence for spin-pumping exists [4–6], polarized spin current has yet to be observed directly traversing a nonmagnetic layer. The possibility of ballistic transport (direct electron transfer from the ferromagnetic into the nonmagnetic conduction band) of spin-polarized electrons hasn't been ruled out, although it is commonly believed that in transition metals the $3d$-electrons couple with unpaired nonmagnetic conduction electrons (s-electrons in the case of Cu). This results in angular momentum transfer via spin-flip scattering across the interface [7]. Another scenario involves defect induced two-magnon scattering along the interface [8]. Additional mechanisms that further cloud the damping picture include incoherent elastic scattering at lattice defects, increased scattering from interface roughness, quantum confinement effects across ultra-thin layers, and non-uniform structural changes within the ferromagnetic layer. An increase in spin-orbit coupling is thought to provide a means for additional intrinsic magnetic damping in the form of incoherent phonon and magnon transfer to the parent lattice.

The observed magnetic Gilbert damping,

$$G = G_o + \frac{(g\mu_B)^2 G^{\uparrow\downarrow}}{2\pi\hbar t A}, \tag{1.3}$$

can be broken down into intrinsic, G_o, and extrinsic, $G^{\uparrow\downarrow}$, contributions where the latter characterizes the desired polarized spin transfer. The Lande g-factor, g for short, in $3d$ transition metals is a function of their relative spin and orbital magnetic moments, t is the thickness of the ferromagnetic layer in which spin-pumping originates, and A is the contact area between the ferromagnet and the region into which spin polarized current flows. Varying ferromagnetic thickness allows the intrinsic and extrinsic damping to be separated provided the structure of the typically ultra-thin ferromagnetic does not change with variation in thickness [9]. Although this assumption is commonly made to extract magnetic parameters from ferromagnetic resonance measurements, under strained and possibly lattice-matched conditions only direct structural measurement can verify the validity of this practice for a range of ferromagnetic thicknesses. Understanding the mechanisms responsible for Gilbert damping is interesting not only from a scientific standpoint, but is also of immediate technological importance because it intimately affects the current needed for spin-torque reorientation and ultimately dictates the speed at which magnetic bits can be written.

Additionally, predicting magnetic anisotropy, and in particular tailoring easy-axis perpendicular anisotropy in thin films of more than a few monolayers thick, is also of high importance. Not only would perpendicular magnetic orientation allow for a denser packing geometry, but in most thin film spin-torque systems magnetization reversal involves precession out of the film plane. Thus, the degree of difficulty in magnetizing the film along its perpendicular direction intimately affects threshold current required and, therefore, the energy consumed in switching a spin-torque device. Even if complete perpendicular magnetic anisotropy was not achieved due to overwhelming large dipole-dipole shape anisotropy, finding a means to reduce the difference between the easy and hard magnetic axes would help.

Magnetic anisotropy, however, is challenging to predict because it is the culmination of many magnetic interactions. For example anisotropy includes intrinsic magnetocrystalline anisotropy which is highly dependent on crystalline symmetry, strain, and distortion. Additionally, geometrical effects such as dipole-dipole determined shape anisotropy and reduced coordination at interfaces and surfaces where direct exchange-coupling affects the net spin moment also play a role. Even *s*-*d* indirect exchange along transition and nonmagnetic metal interfaces is thought to play a significant part in mediating both polarized spin-transport and perpendicular anisotropy. Gaining insight into the potential contributions from these different effects is important in fully understanding any thin-film magnetic device.

1.2 Influences on Ferromagnetism

If unpaired electrons remain after orbital filling proceeds according to the Aufbau (building-up) principle, spontaneous atomic magnetism may occur. Being fermions, electrons cannot doubly occupy the same state (Pauli Exclusion Principle), and their wave functions must be anti-symmetric upon exchange. This means that either the spin or the spatial portion of their wave functions must be anti-symmetric. Due to decreased nuclear shielding and inter-electronic Coulomb repulsion, anti-symmetric wave functions with increased spatial spread are preferred in ferromagnetic systems, and these produce triplet states lower in energy than singlet states (Hund's First Rule of maximized multiplicity). The result is a maximization of unpaired electrons within the valance bands.

The Weiss model of dipole-dipole interactions, however, is quite insufficient to explain the high Curie temperatures of transition metals such as Co, Ni, and Fe [10]. A shorter-range direct exchange ($\propto e^{-R}$ where R is the distance between electrons) resulting from wave function overlap could account for such energies in principle. A more complete description of this type of ferromagnetism is described by Freeman and Watson [11]. The exponentially decaying nature of direct exchange limits it to only nearest-neighbor electrons in the form of

$$H_{\text{exchange}} = -\mathbb{J}\left(R_{ij}\right)\vec{S}_i \cdot \vec{S}_j \tag{1.4}$$

where

$$\mathbb{J}\left(R_{ij}\right) = E_{\text{singlet}} - E_{\text{triplet}}. \tag{1.5}$$

$\vec{S}$ represents each interacting electron spin, while E_{singlet} and E_{triplet} are the energies of different electron configurations. If the coupling constant, $\mathbb{J}$, is positive ferromagnetism proceeds; if negative anti-ferromagnetism. Its sign results from the interplay between degree of wave function overlap and the spin wave function symmetry. For example in atomic configurations such as Mn where valence electrons reside in orbitals compressed by relatively close nuclei, symmetric spatial wave functions with anti-symmetric spins (anti-ferromagnetism) are preferred. In systems of larger nuclear spacing, like Fe, a decrease in nuclear shielding with larger anti-symmetric spatial wave forms and symmetric spin functions (ferromagnetism) is preferred. This underscores how altering atomic distance not only changes the density of states, but can even tip the balance between ferromagnetism and anti-ferromagnetism.

For this dissertation, however, the only ferromagnetic materials, specifically Co and Ni, will be dealt with in a magnetic context. Assuming unpaired spins align, the total spin moment per atom is expressed as

$$\mu_S = -2\left\langle S_Z \right\rangle \mu_B/\hbar = \mu_B\left(N^{\uparrow} - N^{\downarrow}\right). \tag{1.6}$$

S_Z is the spin moment expectation along z, and is a function of the number of spin-up minus spin-down $(N^{\uparrow} - N^{\downarrow})$ moments within the $3d$ valance band. Additionally, by virtue of having charge and moving within a confined orbital the electrons also acquire a magnetic orbital moment,

$$\mu_L = -\left\langle L_Z \right\rangle \mu_B/\hbar, \tag{1.7}$$

where L_Z is the angular expectation value projected along z. Electrons within a common orbital that travel in the same direction (and thus have similar momentum) tend to overlap less, reducing Coulomb repulsion. This leads to the second of Hund's Rules which states that the configuration resulting in the largest value of L, while still obeying the first of Hund's rules and the Exclusion Principle, is lowest in energy.

An electron's net magnetic moment, μ_e, subject to an external magnetic field, $\vec{B}$, experiences a magnetic torque that tends to align it parallel to that field [12]. Its energy is given by

$$H = -\mu_e \cdot \vec{B}. \tag{1.8}$$

The electron's orbital motion about a positively charged nucleus, however, also generates a magnetic field in the electron's rest frame and exerts a magnetic torque on its spin. This spin-orbit coupling correction to the Hamiltonian becomes

$$H_{so} = \left(\frac{e^2}{8\pi\epsilon_o}\right)\frac{\vec{S}\cdot\vec{L}}{m^2c^2R^3}. \tag{1.9}$$

This results not in the separate conservation of L and S, but of total angular momentum, $J = L \pm S$. It is the basis of magnetic sensitivity of circular dichroism (next chapter) and is also the root of Hund's third rule which states that for less than half-filled shells the lowest energy is achieved from minimizing $J = |L - S|$. The opposite is true for more than half-filled shells.

1.3 Magnetic Anisotropy

Within standard, unstrained lattices the density of states and spin moments, dependent on the exchange interaction of about an eV, are roughly equal in all directions due to a high degree of crystalline symmetry. Small differences in net magnetic moments between different crystallographic structures are expected. For example bulk hexagonal close packed, body centered cubic, and face centered cubic Co moments have been calculated at 1.57 [13], 1.646 [14], and 1.56 [15] μ_B, respectively. For thin films it is usually the dipole-dipole shape anisotropy that produces the typical in-plane preferred magnetization.

Spin-orbit coupling, particularly noticeable at interfaces where asymmetry reduces the spin-orbit quenching found in bulk transition metals, is thought to be the primary source of magnetocrystalline anisotropy energy [16] rather than orbital moment anisotropy alone as previously suggested [17]. For a monolayer of Co the calculated difference between in and out-of-plane [111] face centered cubic orbital moments, for example, is a striking 0.32 and 0.08 μ_B [16], respectively.

In general, broken symmetry has the largest impact on magnetocrystalline anisotropy as it dictates the order to which spin-orbit coupling terms must be carried out before anisotropy can be observed. For example [13] the magnetocrystalline anisotropy of cubic crystalline structures is determined by

$$\mathbb{M}_{\text{cubic}} \propto \frac{\lambda_{\text{so}}^4}{W^3}, \tag{1.10}$$

while the magnetocrystalline anisotropy of a uniaxially symmetric structure is expressed as

$$\mathbb{M}_{\text{uniaxial}} \propto \frac{\lambda_{\text{so}}^2}{W}. \tag{1.11}$$

For transition metals the spin-orbit coupling, λ_{so} is typically on the order of 50 meV, while the bandwidth, W, is on the order of a few eV [18]. The magnetocrystalline anisotropy for these two cases is therefore approximately several hundred times different.

It is interesting to ponder the idea of breaking symmetry not just at an interface, but rather from strain induced distortion. It is not uncommon for thin films to form polycrystalline, textured structures with a preferred out-of-plane orientation which provides an intrinsic uniaxial asymmetry. In general the net magnetic moments of transition metals have been found to decrease with high-pressure induced compression [19] and are predicted to increase (both spin and orbital moments) with isotropic expansion. For example spin and orbital magnetic moments of face centered cubic Co were found to theoretically increase on average (over all crystallographic orientations) by 43 and 31 %, respectively, upon increasing the face centered cubic lattice constants from 2.2 to 2.3 $\mathring{A}$ along a theoretical unit-cell wide wire [20]. Studying the effect of strain induced distortion on magnetocrystalline anisotropy (with the eventual aim of being able to tailor samples to achieve perpendicular magnetic anisotropy) would incorporate aspects of both expansion and compression, while also achieving a uniaxial asymmetry needed for enhanced magnetocrystalline anisotropy. The results of such an approach could be most interesting.

Adequate magnetic measurement methods and limited theory already exist, but correlating these with measurable, detailed structural changes within thin, and often polycrystalline, films is the next difficult step which needs to be undertaken. Perhaps this sentiment is best embodied by Daalderop *et al.* [13] who wrote,

> More recently it has been pointed out that magnetoelastic energy could manifest itself as an interface anisotropy if the lattice misfit strain of the Co layer were inversely proportional to its thickness. Experimentally, however, the structures of the multilayers are not well known, so that the importance of the magnetoelastic contribution to the measured interface anisotropy is still unclear.

This statement exemplifies the need for a better non surface constrained, element specific tool to fully characterize strain and distortion. This aim will be explored and developed further in chapter 3.

1.4 Spin-Torque Sample Specifics and Open Questions

The spin-transfer systems studied in this dissertation have been reduced to a single ferromagnetic layer surrounded by nonmagnetic, Cu regions with a long spin diffusion length scale of 250 nm. These are followed by Pt spin-sinks preventing spin backflow from the outermost edges. Although similar samples have been studied within dual ferromagnetic layer, spin-torque devices [21], studying just one magnetic layer at a time reduces ferromagnetic cross-talk and allows for a clearer understanding of the damping process itself.

The ferromagnetic layer for the simplest series discussed within this dissertation is composed of textured, polycrystalline Co ranging from 12 to 66 $\AA$ in thickness. First studied with ferromagnetic resonance [22] these samples were found to have an overall increase in magnetic orbital to spin moment ratio compared with bulk face centered cubic Co for all thicknesses examined. This discrepancy was further enhanced by decreasing the Co thickness, but leveled off at a healthy 25 % orbit:spin increase for even the thickest ferromagnetic layers. The thickness-dependent portion was attributed to a lowering of symmetry at the Cu-Co interfaces, while the intrinsic elevated orbit:spin ratio was not fully explained. Additionally, the extrinsic magnetic damping was found to increase substantially with decreasing thickness, shown in Figure 1.2. This was taken as enhanced Gilbert damping due to the increased surface to bulk ratio.

Lacking a clear consensus about the crystalline structure and strain of ultra-thin Co sandwiched between much thicker [111]-textured face centered cubic Cu layers, the first priority was to devise a method to accomplish the structural characterization

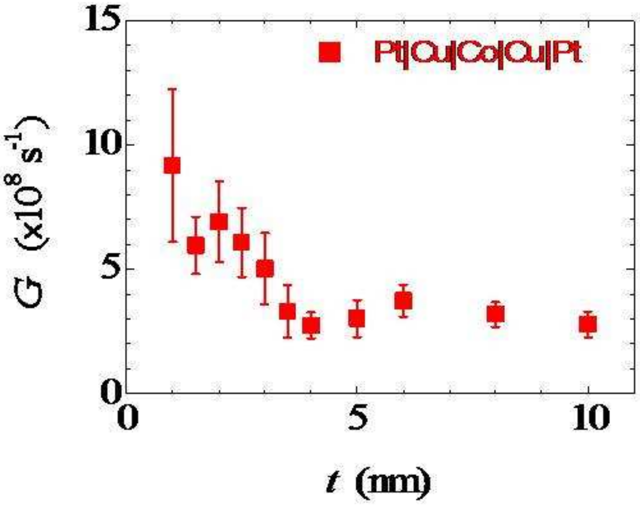

Figure 1.2: Extrinsic Gilbert Damping. The values shown were extracted from ferromagnetic resonance measurements performed on ultra-thin Co samples [22].

of the Co. The second task was to look for any structural changes from induced strain originating from the reasonably well-matched Cu layers as a function of Co thickness. The idea was to verify whether the thickness-dependent magnetic changes observed by ferromagnetic resonance were indeed attributable to differences in the interface:bulk ratio, as opposed to structural changes between ultra-thin ferromagnetic layers of different thicknesses.

Tetragonal strain and changes in nearest-neighbor distance on the order of a percent have been theoretically predicted to have a significant impact on both spin and orbital magnetic moments [20, 23]. However, measuring such systems experimentally to test theoretical prediction is a challenge, especially for ultra-thin thicknesses which are likely to experience the highest degree of strain and possible lattice matching to neighboring regions. After determining the degree and orientation of trigonal strain within the ultra-thin Co layers using anomalous x-ray diffraction (chapter 4), x-ray magnetic circular dichroism provided a good opportunity to measure spin and orbital moments separately (chapter 5). This in turn also provided a rough measure of whether the increase in orbit:spin ratio was substantially affected by deviation in spin, orbital, or both magnetic moments from their bulk values.

In the interest of achieving perpendicular magnetic anisotropy, repeating multilayers consisting of a given thickness of Co, t, and twice that thickness of Ni, $2t$, were substituted for the pure Co ferromagnetic layer. For the rest of this dissertation the shorthand notation used will be [t Co|$2t$ Ni] x n, where n is the number of repeats and happens to be set to twelve. (The exact number of repeats is unimportant for magnetic properties, but it does affect the total amount of material and, therefore, the signal observed when probed with ferromagnetic resonance or x-rays.) The individual Co layer thicknesses, t, range from 1 to 6 $\mathring{A}$, all being equal within a given sample. The particular ratio of t Co:$2t$ Ni has been predicted to have maximal anisotropy arising from both Co-Ni interface anisotropy and from a Fermi energy close to the $3d$-bands in which spin-orbit interaction favors out-of-plane magnetization. For thicknesses of $t = 4$ $\mathring{A}$ or less the predicted out-of-plane anisotropy should be sufficient to overcome the in-plane dipole-dipole shape anisotropy, resulting in net perpendicular magnetization.

Although perpendicular magnetization was both predicted and experimentally observed [24] for such layers, it was not observed in our samples. Both the cited literature and our own samples consisted of polycrystalline, face centered cubic Co and Ni layers textured with the [111] orientation aligned along the sample perpendicular. However, in literature the multilayers were grown atop [111]-textured Au grown with e-beam evaporation, while our samples were grown atop [111]-textured Cu over Pt by the NYU Kent group using a sputtering technique [25]. The magnetic anisotropy difference then be due to either changes in strain or to variations in roughness between the Co and Ni layers in comparison to the cited samples. Therefore, anomalous diffraction and extended x-ray absorption fine structure were both applied in order to get a structural explanation as to where the lack of perpendicular magnetic anisotropy might have originated. Additionally, x-ray magnetic circular dichroism was used to further explore the individual Co and Ni magnetic behavior. It was also used to measure their orbital moments which would be expected to be influenced by any strain induced structural distortion.

1.5 Organization of Dissertation

In order to answer the questions posed above it is evident that both detailed magnetic and structural characterization are required. As will become clear in chapter 3, however, solving non-surface ultra-thin structure is a demanding task, especially so because interlayer interference is enhanced with diminishing thickness. Beyond the fitting parameter based technique of extended x-ray absorption fine structure (described in chapter 2 along with other available methods and the x-ray processes on which they are based), adequate structural methods not limited to surface layers are lacking. Therefore, a major aim of this dissertation has been the development of a novel, anomalous x-ray diffraction method that incorporates information from multi-energy diffraction patters simultaneously to uniquely solve structures in an element specific manner. The technique will be referred to as MOIDS (Multi-wavelength Overlapping and Interfering Diffraction Separation) and will be described in detail along with its limitations in chapter 3.

Chapter 4 is devoted to experimentally measuring strain-induced distortion within polycrystalline ultra-thin films. This was accomplished applying a limited version of MOIDS to a series of spin-torque samples to solve the structure and strain of single ferromagnetic layers ranging from 65 to just 12 $\mathring{A}$ in thickness buried within a

Pt|Cu|ferromagnet|Cu|Pt sandwich. The results are compared with the established extended x-ray absorption fine structure method, and the complementary nature of the two methods is discussed.

Chapter 5 presents the element specific and orientation sensitive x-ray magnetic circular dichroism measure of spin and orbital magnetic moments for samples with structure similar to that described in chapter 4. Replacing the Co with Co|Ni multilayers with a 1:2 ratio of Co to Ni has been shown to increase perpendicular anisotropy [24]. The magnetic properties and anisotropy from a series of thickness varied (*i.e.* interface:bulk varied) Co|Ni multilayers were explored in detail using this method.

Chapter 6 summarizes the findings of this dissertation. In particular it discusses the combination of structural and magnetic findings of chapters 4 and 5. Together these measurements shed light into the role that strain and ferromagnetic interfaces play in regard to spin and orbital magnetic moments, magnetic anisotropy, and magnetic damping. Additionally, the practice of assuming that ultra-thin ferromagnetic structure does not change as function of thickness, for purposes of extracting Gilbert damping, is examined for a range of Co thicknesses.

Chapter 2

X-Ray Processes, Experimental Methods, and Beamline Considerations

2.1 Charge Scattering

X-rays, loosely defined as electromagnetic radiation with wavelengths between 0.01 and 10 nanometers, interact with matter based on a quantum mechanically determined probability of absorption or scattering, which are intimately related processes. A reasonable starting point is the Hamiltonian of charged electrons within a radiation field [26],

$$H = H_o + \frac{e^2 A^2}{2m} + \frac{e\vec{A} \cdot \vec{p}}{m} \tag{2.1}$$

with

$$\vec{A} = \hat{\epsilon} A_o \left[a_k e^{i(\vec{k} \cdot \vec{R} - \omega t)} + a_k^\dagger e^{-i(\vec{k} \cdot \vec{R} - \omega t)} \right]. \tag{2.2}$$

$\vec{A}$ is the vector potential of the radiation field, $\vec{p}$ is the momentum, and a_k, $a_k^\dagger$ are the standard photon annihilation and creation operators. $\hat{\epsilon}$ describes polarization of the incident photon electric field. Assuming the electron cross-sections are small enough so as to act as a perturbation on the radiation field (Born approximation), Fermi's golden rule can be used to calculate the transition probability per unit time, W [27], as

$$W = \frac{2\pi}{\hbar} \overline{|V_{fi}|^2} \rho\left(E_f\right), \tag{2.3}$$

where ρ is the density of final states and $E_f \cong E_i$. The subscripts i and f refer to initial and final states. The first term of equation 2.1, quadratic in annihilation and creation operators, intuitively leads to a scattering process equivalent to classical Thomson scattering. Independent of incident photon energy, its cross-section is simply proportional to the number of electrons encountered by the radiation field. The second term of equation 2.1, linear in annihilation and creation operators, can either destroy or create a photon, but not both. This represents the photoelectron absorption of a bound electron. If the bound electron is a core electron then subsequent de-excitation proceeds by ejection of an Auger electron or through reshuffling of occupied electron states accompanied by emission of fluorescent radiation.

Taking the perturbation to second order produces

$$W = \frac{2\pi}{\hbar} \left| \langle f|H|i\rangle + \sum_n \frac{\langle f|H|n\rangle\langle n|H|i\rangle}{E_i - E_n} \right|^2 \times \delta\left(E_i - E_f\right). \tag{2.4}$$

In this context the second term of equation 2.1 also becomes quadratic in $\vec{A}$. This leads to a new form of scattering, resonant elastic scattering, which is also commonly referred to as anomalous scattering for historical reasons. Its cross-section is greatly enhanced when the incident radiation energy nearly matches that of an allowed electronic transition to an unfilled state or to the continuum. Like photoelectric absorption, the energy dependence of anomalous scattering provides a route for achieving element specificity.

A pure cross-section can be derived from

$$\frac{d\sigma}{d\Omega} = \int_E \left(\frac{W\rho\left(E_f\right)}{I_o}\right) dE, \tag{2.5}$$

where I_o is the incident flux. In experimental terms it is often convenient to recast the cross-section in terms of a generic atomic scattering factor, f, such that

$$\frac{d\sigma}{d\Omega} = \left| r_o \hat{\epsilon}_f^{\dagger} \cdot f \hat{\epsilon}_i \right|^2. \tag{2.6}$$

f is typically expressed as a unitless factor which expresses the value of an atomic cross-section in proportion to that of a single electron, $r_o^2 = 2.82 \times 10^{-5}$ $\mathring{A}$. Notice that for charge scattering the maximum intensity is observed when the incident and scattered electric field directions, $\hat{\epsilon}_i$ and $\hat{\epsilon}_f$, align and decreases as the cosine of angle squared between them otherwise. (This is why for horizontally polarized light detectors sensitive to scattering are set to rotate within a vertical plane normal to the incident beam, while isotropic fluorescence is conversely measured at 90° horizontal to the incident photon polarization in order to minimize any scattered light contamination.)

The elastic atomic scattering factor is composed of terms relating to Thomson scattering, f_o, a resonant correction, f_{res}, and an absorption term, f_{abs}. For experimental purposes it is often convenient to rewrite the scattering into terms containing the real and imaginary parts of the resonant scattering amplitude,

$$f = f_o + f_{\text{res}} + i f_{\text{abs}} \equiv f' + i f''. \tag{2.7}$$

Complex notation is used because real and imaginary parts are shifted in phase by $\frac{\pi}{2}$ radians from one another. In this dissertation the convention used will be that single and double primes denote the real and imaginary components of a given term, respectively.

Well away from a resonant transition, the atomic scattering factor is well approximated by the single-atom based Henke data tables [28,29]. These have been tabulated from compiled experimental absorption data where smoothing has been used to remove the observed effects of solids (the origin of which will be described shortly). Interpolation using theoretical atomic absorption theory is used to fill in gaps. A Kramers-Kronig transform can be applied to derive the real part of the scattering amplitude from measured absorption data (discussed in more detail below).

Atoms within solids, unlike single atoms, often exhibit an overshoot just beyond a cross-section jump which corresponds in part to transitions into bound states just below the continuum. Additional oscillatory behavior in the near-energy region following the transition edge is a quantum mechanical effect described further in section 2.6. If the these two effects significantly alter the absorption profile, or if the obtaining variations in shape is spectroscopically important (oxidation, ionic versus covalent bonding, crystal structure, *etc.*), then experimental absorption data is required.

The simplest way to determine these constants directly is from a transmission experiment when possible. The change in photon intensity at a given energy before and after propagation through a sample of known thickness, t, and density, ρ, is given by

$$\frac{I}{I_o} = e^{-\mu\rho t} \tag{2.8}$$

where the absorption is given by

$$\mu = 2r_o\lambda f_{\text{abs}}. \tag{2.9}$$

and is dependent on the photon wavelength, λ. The part of the resonant scattering amplitude may now be determined using

$$f_{\text{res}}(\omega) = -\frac{1}{\pi}\wp\int_{-\infty}^{+\infty}\frac{f_{\text{abs}}(\omega)}{\omega' - \omega}d\omega' \tag{2.10}$$

where $\wp$ stands for the principle value of the integral, and means that the integration is to be performed in two parts from $-\infty$ to $\omega-\xi$ and from $\omega+\xi$ to $+\infty$ with $\xi \to 0$ [26]. Alternatively, in cases where direct transmission measurements cannot be performed electron-yield measurement of secondary Auger electrons or fluorescence also provide a measurement directly proportional to absorption as long as self-absorption effects are negligible or are explicitly accounted for.

Non-oxidized transition metal absorption cross-sections from the innermost shell, K-edge transitions, however, differ minimally from the atomic Henke scattering factors. Thus, for purposes of anomalous diffraction where diffraction was performed at either the minima of scattering or well away from resonance, the Henke data adequately represent the true scattering factors and were used in place of experimentally determined factors, which for ultra-thin films on thick substrates would have been difficult to perform.

2.2 Magnetic Scattering

Thus far the Hamiltonian given has not included the spin associated with electrons. This can be added as a perturbation of the form [26]

$$H_{\text{spin}} = -\frac{e\hbar}{2mc}\sum_j \vec{S}_j \cdot \nabla \times \vec{A}\left(\vec{R}_j\right). \tag{2.11}$$

X-rays, being electromagnetic in nature, experience both charge and (magnetic) spin scattering, and as such in 1954 it was theoretically predicted that magnetism in free atoms could be probed by x-rays [30, 31]. In 1970 [32] this idea was extended to magnetism in solids. By 1972 deBergevin and Brunel obtained the first experimental observation of magnetic x-ray diffraction on antiferromagnetic NiO [33], and by 1981 they investigated the polarization dependence of magnetic scattering on antiferromagnetic Fe_2O_3 [34]. To order

$$\tau = \frac{\hbar\omega}{mc}, \tag{2.12}$$

the polarization-dependent magnetic scattering arising from spin is given by [35]

$$f = -r_o\left[(\hat{\epsilon}_f \cdot \hat{\epsilon}_i)F_c(\vec{k}) - i\tau\vec{F}_s(\vec{k})\cdot\vec{B}\right] \tag{2.13}$$

with

$$\vec{B} = (\hat{\epsilon_f} \times \hat{\epsilon_i}) - (\hat{k_f} \times \hat{\epsilon_f}) \times (\hat{k_i} \times \hat{\epsilon_i}) + (\hat{k_f} \cdot \hat{\epsilon_i})(\hat{k_f} \times \hat{\epsilon_f}) - (\hat{k_i} \cdot \hat{\epsilon_f})(\hat{k_i} \times \hat{\epsilon_i}). \tag{2.14}$$

F_c and F_s are the Fourier transforms of the change and spin densities per unit cell, and $\hat{k}$ is the direction of photon propagation.

As noted previously materials can also have an orbital magnetic moment associated with the motion of their unpaired electrons. This type of x-ray magnetic scattering can be expressed similarly to equation 2.14 by addition of

$$r_o\left[i\tau\vec{F}_l(\vec{k})\cdot\left\{(\hat{\epsilon}_f \times \hat{\epsilon}_i) - \hat{k}(\hat{k}\cdot(\hat{\epsilon}_f \times \hat{\epsilon}_i))\right\}\right]. \tag{2.15}$$

to the atomic scattering factor [36]. F_l is the Fourier transform of the orbital magnetic moment density per unit cell.

Pure magnetic scattering, however scales as $|f|^2 \propto \tau^2$, which at 8 keV, for example, is reduced by $\sim 2.5 \times 10^{-4}$ from charge scattering. The cross-term arising from charge and magnetic interference is reduced by only a single factor of τ, but even so spin scattering scales with the net spin polarization, which even in ferromagnets is considerably smaller than charge scattering, proportional to number of electrons. It is interesting to note, that unlike charge scattering, spin scattering can rotate the plane of polarization and this provides a mechanism for separating the two with appropriate use of polarizers. The experiments above relied on observing the much smaller magnetic scattering at places where charge scattering was forbidden. This explains why the materials first explored magnetically using x-rays were antiferromagnetic rather than ferromagnetic.

It 1985 it was discovered [37] that magnetic sensitivity could be enhanced at the K-shell absorption edge of ferromagnetic nickel, the first case of resonantly enhanced magnetic scattering. The following year it was predicted that a large magnetic enhancement would be observed on the $M_{4,5}$ edges of rare earths [38], and was experimentally confirmed in 1986 [39]. Shortly thereafter hard x-ray circular dichroism was observed in both transition metals and rare earths [40]. In 1988 a huge resonant enhancement of 50 x's was observed from the L_3 edge of holuminum [41], and this was explained theoretically [42] by a multipolar expansion of the transform. In 1990 several more exciting developments occurred. McWhan *et al.* found an unprecedented six orders of magnitude enhancement of magnetic scattering at the M_4 edge or uranium [43], Kao *et al.* measured magnetic exchange along the L_3 and L_2 edges of Fe using linearly polarized light [44], and Chen *et al.* used soft, circularly polarized x-rays to magnetically probe Ni [45]. In 1992 a method was outlined for probing orbital magnetic moments [46] with circularly polarized light, and by 1995 Chen *et al.* applied sum rules that allow both spin and orbital magnetic moments of the $3d$ transition metals to be measured with circularly polarized x-rays using L-edge transitions [47]. The method is still heavily used today, and its details will be discussed further in the next section. More recently x-ray magnetic linear dichroism has been revisited as a means of measuring the magnetocrystalline anisotropy energy through the spin-obit interaction more directly than with x-ray magnetic circular dichroism [16, 48, 49].

2.3 X-Ray Magnetic Circular Dichroism

The basic principle for x-ray magnetic circular dichroism is that photoabsorption of electrons into spin-polarized valance bands (which give rise to ferromagnetism via exchange coupling on the order of 1 eV) is sensitive to the absorbing electron's state of polarization. The naturally spin-orbit split core electrons (such as $2p$ electrons of the transition metals), therefore, make for good polarized probes. As noted previously, large dichroism magnetic enhancement has been observed at dipolar $2p \rightarrow 3d$ resonant transitions, making the experiment much easier to perform than away from resonance. Transitions described in terms of K, L, and M shells, based on the principal quantum numbers, are shown in Figure 2.1. The magnetic materials studied in the dissertation are Co and Ni, and as such their bound energies with respect to the fermi surface are also given in Figure 2.1 [50] along with the bulk-valued number of holes within their $3d$ valence bands [51]. The number of unpaired $3d$ holes are responsible for observed ferromagnetism.

Photoabsorption is primarily mediated by interaction between the electric field of a photon and an electron dipole moment. This results in an odd parity change that is manifested as a unit change in orbital angular momentum (dipole selection rule). In practical terms this means allowed dipole transitions occur from the s to p and p

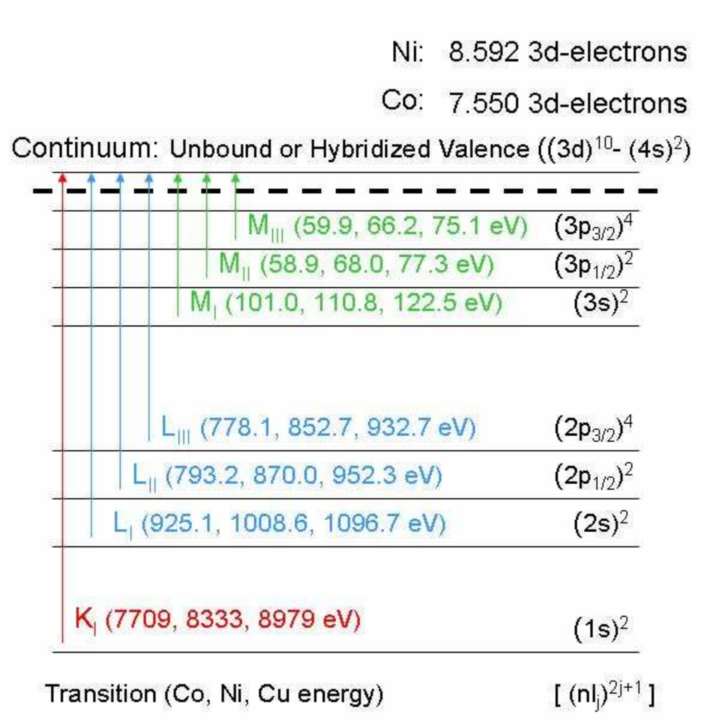

Figure 2.1: The L, M, and K shell transitions and their associated energies for Co and Ni. Upper right gives the bulk-valued number of $3d$ electrons for each element.

to d orbital, but not from the s to d orbital for example. Thus, in transition metals the most sensitive magnetic transitions are the L_3 and L_2 edges, and these outweigh the L_1 absorption by a factor of about 20 for the transition metals [18].

Photons transfer their momentum, $\pm\hbar$ for right and left circularly polarized light (0 for linearly polarized light), to an absorbing electron though spin-orbit coupling. Spin couples to orbital momentum oppositely in the originating electrons of the L_3 and L_2 bands as $(L+S)$ and $(L-S)$, respectively. (Note that in this context L and S refer to orbital and spin angular momentum.) Opposite spin polarization between the two states is achieved for photoelectron absorption from any given circular polarization. Now the polarization of photoelectrons matters in order for them to complete their transition into the spin-split valance $3d$ band. Therefore, the net spin of the $3d$ band is roughly related to the number of L_3 - $2L_2$ transitions, where the factor of two comes from the fact that there are twice as many electrons originating in the $2p_{\frac{3}{2}}$ state than from $2p_{\frac{1}{2}}$ [18]. The total number of holes available is related to the non-polarized sum of the L_3 and L_2 transitions. Rewritten explicitly for $3d$ transition metals this is given in the first of two sum rules as [47]

$$\mu_S = (N^{\uparrow} - N^{\downarrow})\mu_B = -\frac{(6P - 4Q)(10 - n_{3d})}{R} \tag{2.16}$$

where

$$P = \int_{\mathrm{L3}} (\mu^+ - \mu^-) dE, \tag{2.17}$$

$$Q = \int_{\mathrm{L3+L2}} (\mu^+ - \mu^-) dE, \tag{2.18}$$

and

$$R = \int_{\mathrm{L3+L2}} (\mu^+ + \mu^-) dE. \tag{2.19}$$

n_{3d} is the number of effective $3d$ electrons, thus, 10 - n_{3d} describes the number of effective valance band holes. Note that R is the integral sum of left and right circularly polarized light after the Henke [28, 29] atomic absorption profile has been fit to the data and removed.

The $3d$ electrons also experience spin-orbit coupling on the order of 50 meV. Due to crystallographic quenching in solids this is typically about an order of magnitude smaller than exchange energy, and this produces the correspondingly larger spin to orbital magnetic moments. Summation of the circularly polarized absorption of the spin-orbit split L_3 and L_2 core electrons is proportional to the orbital moment of the $3d$-electrons. This is the basis for the second transition metal sum rule [47],

$$\mu_L = \frac{(-4Q) \times (10 - n_{3d})}{3R}. \tag{2.20}$$

Due in part to the difficulty of normalizing measured transmission by less than perfect background scans, fitting Henke absorption to the measured absorption spectra, and to any non-linear scaling problems, it is often experimentally easier to obtain the spin to orbit ratio rather than the individual spin and orbital moments. (Details of the actual data fitting procedure will be explained more fully in Chapter 5.) Combining equations 2.16 and 2.20 yields

$$\frac{\mu_S}{\mu_L} = \frac{(9P - 6Q)}{2Q}. \tag{2.21}$$

If one assumes that the spin does not change for magnetization along different directions, this method effectively probes the magnetic anisotropy in terms of changes in orbital moments for different crystallographic directions.

Magnetically, x-ray magnetic circular dichroism spectroscopy is a valuable tool that is can be used to separately measure spin and orbital moments in an element specific manner. Sum rules are generally thought to be able to yield spin and orbital moments within a 10 % uncertainty, and orbit:spin ratios within 5 % uncertainty under good experimental conditions [52].

2.4 Diffraction

Whether performed away from or near a resonance edge (the latter termed anomalous diffraction), the diffracted intensity is dependent on the summed amplitude (superposition of coherent waves whose phase varies as a function of spatial position

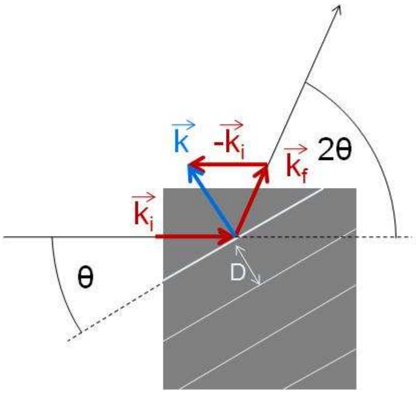

Figure 2.2: Diffraction probes only atomic planes perpendicular to $\vec{k}$ which is defined by the incident and scattered photon wavevectors. Note the angle between the incident x-rays and the surface of the sample need not be set equal to one-half of 2θ.

relative to the viewer) from x number of scattering centers. This can be expressed as

$$I = I_o n \Delta\Omega \left| \sum_x \left(f'_x + i f''_x\right) e^{i\vec{k}\cdot\vec{r}_x} \right|^2 \tag{2.22}$$

with

$$\vec{k} = \frac{2\pi}{\lambda}\left(\hat{k}_f - \hat{k}_i\right). \tag{2.23}$$

Here the single and double primes refer to real and imaginary parts of the atomic scattering factor as defined in equation 2.7. The exponential portion takes into account contributing phase differences [26, 53]. $\vec{k}$ is a wave vector, the magnitude of which depends on the radiation wavelength, λ, and whose direction is determined by the direction of photon propagation.

Since it is the spatial arrangement of the scattering atom (or molecules) that is typically of interest, the corresponding structure factor, $\mathbb{S}$, will be explicitly defined from here on as

$$\mathbb{S} = \sum_x e^{i\vec{k}\cdot\vec{r}_x} \equiv \mathbb{S}' + i\mathbb{S}''. \tag{2.24}$$

In a periodic structure with repeating lattice planes oriented perpendicular to $\vec{k}$, Figure 2.2, the difference in x-ray path length difference between two scattering planes, Δ, is given by $2Dsin(\theta)$. Here θ is the angle $\vec{k}$ makes with the scattering plane, and D is the periodic spacing probed. Coherent wave summation results when Δ is equivalent to an integer number of wavelengths. Since it is ultimately the wavelength and angle of the detector with respect to the beam that defines the planar distances for which coherent scattering may occur, it is often convenient to write this in reciprocal space notation as

$$Q \equiv \frac{4\pi\sin(\theta)}{\lambda} = \frac{2\pi}{D}. \tag{2.25}$$

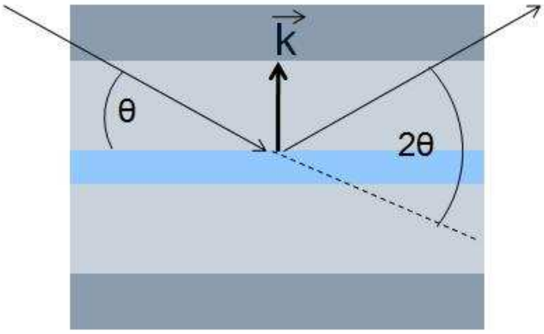

Figure 2.3: Specular reflectivity is a subset of diffraction where θ is typically set to one-half of 2θ in order to probe distances along the sample normal. In the lowest region of reciprocal space total external reflection occurs, and just beyond that multiple scattering within each layer must be accounted for. This is typically done using Parratt's recursive method [54] in order to measure planar layer thicknesses and roughness.

The only distances which can contribute to a Bragg peak are those, or their projections along $\vec{k}$, which follow the above equation.

2.5 Specular Reflectivity

This is special case of diffraction where a planar, layered sample is oriented such that $\vec{k}$ points along its sample normal. The condition is referred to as specular reflectivity and is shown in Figure 2.3). Small-angle scattering is measured in order to probe the layer thicknesses (usually on the order of nanometers to microns) rather than the inter-atomic spacings (angstroms) found at higher Q. An example of an experimentally measured specular reflectivity patterns is shown in Figure 2.4 for a samples of 50 $\AA$ Pt|100 $\AA$ Cu|65 $\AA$ Co|100 $\AA$ Cu|50 $\AA$ Pt atop a thick Si wafer.

At very low scattering angles total external reflection occurs. Beyond this narrow region the reflectivity of nearly perfect crystals is usually so high that the typical diffraction assumption of constant flux throughout the entire sample depth is no longer valid. However, when the sample region of interest lies atop a thick substrate (taken to be infinite), multiple reflections below the topmost surface of the infinite slab may be neglected. The idea then is to calculate the reflectivity for the bottom-most interface, and recursively do the same for all the remaining layers up to the topmost layer. The process known as Parratt's recursive method [26, 54]. The reflectivity between the jth and $jth + 1$ layers is then calculated by

$$\mathbb{R}_{\mathrm{j,j+1}} = \frac{Q_{\mathrm{j}} - Q_{\mathrm{j+1}}}{Q_{\mathrm{j}} + Q_{\mathrm{j+1}}} \tag{2.26}$$

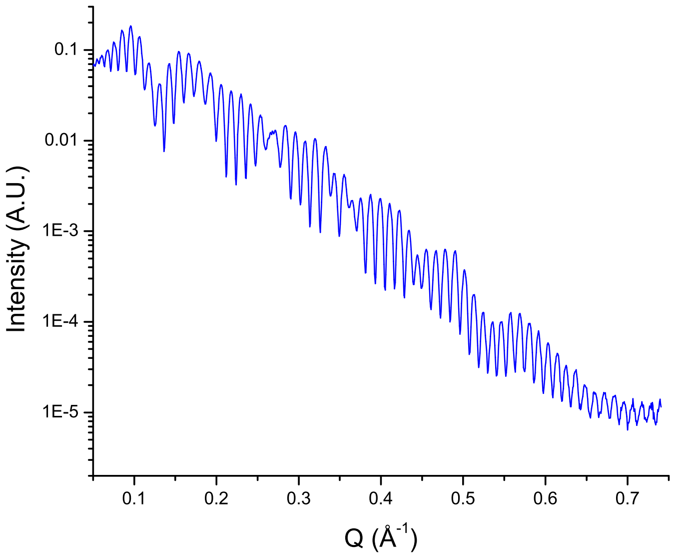

Figure 2.4: An example of experimental specular reflectivity taken on a repeating 6 $\AA$ Co | 12 $\AA$ Ni multilayer, capped on both sides by 100 $\AA$ Cu and 50 $\AA$ Pt. Notice the many orders of magnitude over which the reflected intensity can be measured. In general, the farther out in reciprocal space the pattern is observable, the smoother the constituent sample layers are.

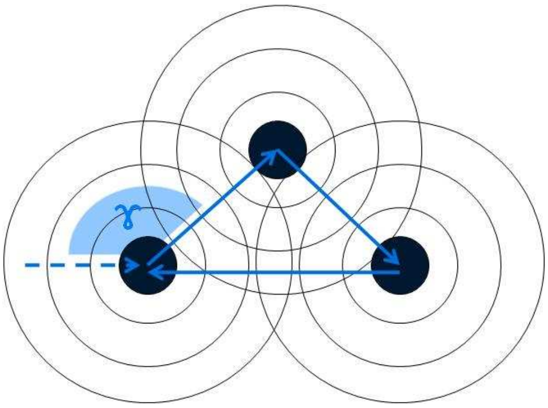

Figure 2.5: Extended X-ray Absorption Fine Structure (EXAFS) is based on the idea that an excited photoelectron can scatter off nearest-neighbor atoms, and in so doing cause interference. This can be used to gain information about the atomic arrangements in an element specific manner. The cosine of the angle, Υ, made by the incident and scattered $\hat{\epsilon}$'s determines the amplitude of a particular scattering path.

where

$$Q_j = \sqrt{Q^2 - 4k^2\rho r_o\lambda^2(f_j' + f_j'')/\pi}. \tag{2.27}$$

Here the f' and f'' refer to real and imaginary parts of the atomic scattering factor as defined in equation 2.7. In terms of the index of refraction, η, equation 2.27 can be rewritten as

$$Q_j = \sqrt{Q^2 - (8k^2\delta_j + i8k^2\beta_j)}. \tag{2.28}$$

where δ and β of the jth layer are determined from the index of refraction using the following relationship,

$$\eta = 1 - \delta + i\beta. \tag{2.29}$$

With known energy-dependent scattering factors, densities, and a guess about the thickness and content of each layer, a reasonable model can be created. Parameters such as individual layer thickness and roughness can then be tweaked until a best fit with experimental data is achieved. Several freeware programs exist for this purpose, but the one employed for specular reflectivity fitting within this dissertation is Parratt32 [55]. Only roughness on a scale less than the thickness of each individual layer can be fit accurately within this model.

2.6 Extended X-Ray Absorption Fine Structure

The extended x-ray absorption fine structure method, EXAFS, analyzes the oscillations of declining magnitude about the Henke atomic absorption for photon energies up to 1 keV beyond the atomic transition [57, 58]. These oscillations, a consequence

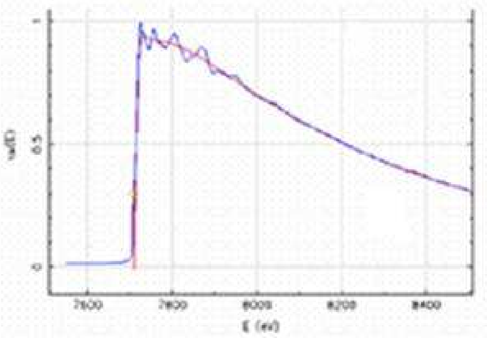

Figure 2.6: An experimental absorption profile for a very thin film of Co about its K-edge. Blue indicates real data and red the background fit. The small oscillations observed are due to nearest-neighbor atomic interference. The phase and magnitude of this interference depends on the amount of energy a liberated photoelectron carries with it.

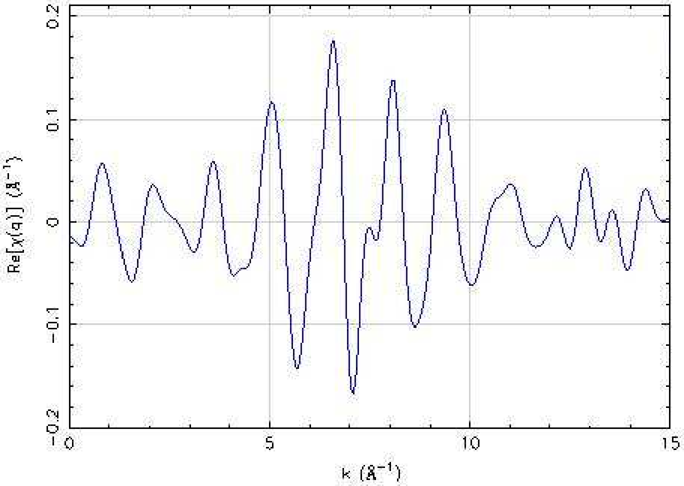

Figure 2.7: The oscillations of Figure 2.6 are shown here converted into reciprocal space. Compared with a theoretical model using a program such as Artemis [56], they can be used to refine the three dimensional atomic arrangement of a crystal or even a powder sample.

of having near-neighbor atoms present, do not occur in isolation. They can simplistically be described as the re-scattering of liberated photoelectrons emitted from an atomic center and backscattered off nearest neighbors, as shown in Figure 2.5.

The energy-dependent oscillations about the single-atom absorption curve, χ, can be expressed as $(\mu - \mu_o)/\mu_o$ where μ is the measured absorption and μ_o is a smoothed background. See Figures 2.6 and 2.7 for further details. These oscillations can then be transformed from energy-space into reciprocal or real-space which corresponds an effective path length an emitted photoelectron would have traveled if backscattered by various near neighbors. By calculating (or measuring on a similar sample) the effective phase shift that scattering from a particular atomic species produces, a real space picture on the arrangement of atoms within a material may be produced. Tweaking a reasonable starting model to match data is typically done with a fitting program such as Artemis [56, 59] which finds the best fit by varying a series of user defined variables (energy shift, roughness, lattice spacing, and bond angle adjustment) within the best guess input model. The method is element specific and elegant, and it has been used to understand many buried thin-film or lattice structures. On the other hand the solution is not guaranteed to be unique and is only as good as the input model used. The method is typically better at refining bond lengths and angles within a known crystal structure rather than solving a completely unknown structure.

2.7 Ferromagnetic Resonance

Although ferromagnetic resonance was not performed directly by the author, much incentive for studying the spin-torque samples came from results obtained by the NYU Kent group using this method. Additionally, the structural findings within this dissertation have implications regarding common practices used to extract ferromagnetic resonance determined values based on thickness variation. Therefore, an explanation of the method will be given here.

A magnet moment, $\vec{\mu}$, subjected to an applied magnetic field, $\vec{B}$, experiences torque, $\vec{\mu} \times \vec{B}$. This results in the precession of $\vec{\mu}$ around $\vec{B}$ at the Larmor frequency, $\omega = \gamma B$, where γ is the gyromagnetic ratio. Materials respond to external magnetic fields by rearranging their moments in opposition to or alignment with it, adding an additional effective demagnetization field, M_{eff}. Thus, B is replaced by $H_{\text{eff}} = B + M_{\text{eff}}$. When a transverse microwave (rf-) field is tuned to energetically match the Larmor precession frequency strong absorption occurs, resulting in magnon excitation. Under this resonance condition the corresponding magnetic field is denoted H_{res}, and is wholly dependent on the rf-frequency applied. Magnetic moments experience short-range nearest neighbor dipolar interactions, and in ferromagnetic materials the extended shape of the material determines (unless perfectly symmetric) the overall preferred alignment direction in ferromagnetic materials. Except for ultra-thin films in which interfaces have a substantial influence, this tends to align the magnetic moments within the sample plane of films. With H_{res} and the external rf-field applied

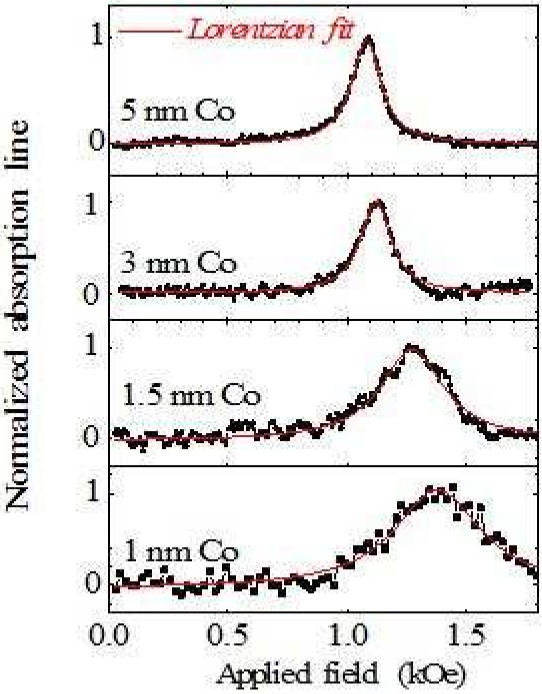

Figure 2.8: Ferromagnetic Resonance Example. Both the value and width of H_{res} contain information about the Lande-g value and Gilbert damping.

along the sample plane [60],

$$\omega = \gamma\sqrt{H_{\mathrm{res}}(H_{\mathrm{res}} + M_{\mathrm{eff}})}. \tag{2.30}$$

A plot of ω versus H_{res} over a range of applied rf-fields (typically 5 to 25 GHz) yields γ from the slope and M_{eff} from the H_{res} intercept. M_{eff} can be broken down further as [61],

$$M_{\mathrm{eff}} = M_{\mathrm{sat}} + \frac{2K_{\mathrm{surface}}}{tM_{\mathrm{sat}}}. \tag{2.31}$$

If the magnetic saturation value, M_{sat}, is known then the surface anisotropy constant, K, a measure of in the difference in ease of magnetization in and out of plane, can be obtained by measuring a series of samples with known ferromagnetic thickness. In more complicated experiments beyond the scope of this work a vectorial anisotropy constant can be fit as a function of applied rf-angle about in and out of the sample plane directions. This can then used to obtain more detailed information about the magnetic anisotropy of the sample.

γ can provide magnetic spin and orbital angular momentum information as

$$\gamma = \frac{g\mu_B}{\hbar}, \tag{2.32}$$

where μ_B is the Bohr magneton, and g is the Lande g-factor (also called the spectroscopic splitting factor). In 3d transition metals it is possible to reduce g to [61]

$$g = 2 + 2\frac{\mu_L}{\mu_S}. \tag{2.33}$$

So far we have assumed all magnetic spins process coherently and have considered only the average of H_{res} as a function of ω. H_{res}, however, has finite full width half maximum (FWHM), ΔH_{res}, and this contains information about non-uniform magnetic damping. The motion of excited magnetic moments can be described by the Landau-Lifshitz-Gilbert equation of motion. In practical terms G can be extracted from the slope of H_{res} versus ω as

$$\Delta H_{\text{res}} = \Delta H_o + \frac{2\pi\omega G}{\gamma^2 M_{\text{sat}}}. \tag{2.34}$$

As noted in section 1.1 damping can be further characterized as intrinsic, G_o, and extrinsic, $G^{\uparrow\downarrow}$, contributions where the latter characterizes the polarized spin loss into a heterogeneous layer. $G^{\uparrow\downarrow}$ is of the particular importance in understanding the process of polarized spin-transfer in spin-torque systems as its dependence on thickness [9] can be used to distinguish between various spin-transfer mechanisms. Note that the determination of both $G^{\uparrow\downarrow}$ and K depend on the assumption that increasing thickness of ultra-thin ferromagnetic layers does not structurally change them in any significant way - a common practice whose applicability on strained, ultra-thin Co layers of 12 to 65 $\AA$ will be examined further in chapter 4.

2.8 Synchrotron Beamlines and Data Collection

All experimental data was collected at one of six synchrotron source beam lines from either the X-ray or Violet-Ultraviolet (VUV) National Synchrotron Light Source (NSLS) storage rings or at the Advanced Photon Source (APS). Synchrotrons produce high brilliance x-rays by acceleration of charged particles (electrons in both cases) kept on a nearly circular path with a series of bending magnets. The acceleration caused by these magnets naturally results in x-ray production, but even higher brilliance can be achieved by use of insertion devices. These consist of a series of alternating magnets placed along straight sections of a synchrotron that force charged particles to oscillate rapidly. They fall into the categories of undulators and wigglers, the difference being that that first has a wider angular emission range while the latter produces highly collimated x-rays. The natural (bending magnet) opening cone angle, ς, is given by the ratio of the resting mass of an electron compared to the energy it acquires when accelerated within a synchrotron as [26]

$$\varsigma = \frac{0.511\text{MeV}}{E_{\text{synchrotron}}}. \tag{2.35}$$

The synchrotron energies are 2.8 Gev, 808 MeV, and 7 GeV for the NSLS X-ray, NSLS VUV, and APS storage rings, respectively. For an undulator the cone angle is

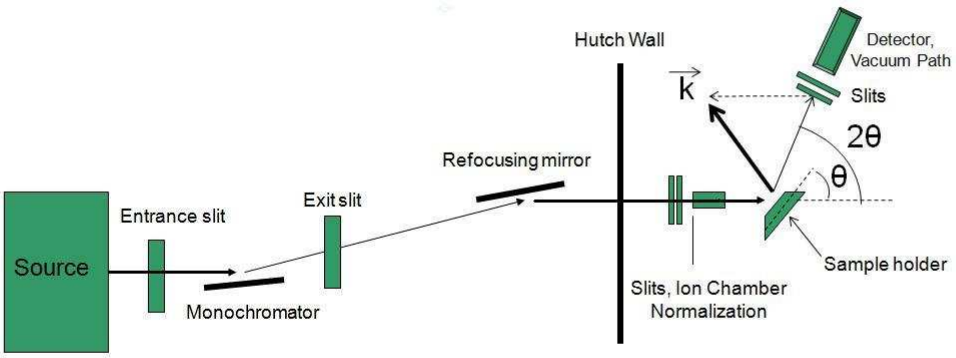

Figure 2.9: Beamline Set-Up

reduced by an additional factor of $\frac{1}{\sqrt{N}}$ where N is the number of periods formed by the insertion device. Within the horizontal plane the radiation is linearly polarized, acquiring more circular polarization of opposite helicities with increasing distance above and below the horizontal plane. This is one method of obtaining circular polarization for x-ray magnetic circular dichroism measurements, and it is utilized at NSLS beamline U4B.

The NSLS x-ray sources used for experiments contained within this dissertation all happen to utilize bending magnets, while only 6-ID-B (APS) used an undulator source. Beam lines X6B, X16B, X16C, X23A, and 6-ID-B (all hard x-ray sources providing photon energies within the 7 to 12 keV region of interest covering Co, Ni, Cu, and Pt K-edges) share a similar configuration shown specifically for X6B in Figure 2.9. Not drawn to scale, it includes all the basic components which will be discussed in general terms. The primary difference in the APS 6-ID-B beamline from the others is that is has a significantly higher flux of 7.1×10^{12} photons per second (measured at 8 keV) compared with 4×10^{10} photons per second (at 10 keV) at X16C, for example. It also has a feedback system in which its entrance and exit slits are constantly repositioned to remain at maximum intensity to nullify the effect of small spatial beam drifts. Beyond θ and 2θ, additional motions, χ and ϕ, are available on a six-circle Huber diffractometer, as shown at X6B in Figure 2.10.

A monochromator, or diffraction grating, selectively scatters photons with an energy that follows the Bragg law, equation 2.25. It is tuned by varying the angle of incidence between its surface and the incoming beam, and has a resolution of $\frac{\Delta E}{E} = 2 \times 10^{-4}$ at 8 keV consistent with a Si [111] reflection on which it is based. Note that higher odd-order harmonics will also meet the Bragg reflection condition. Special care such as using an energy-selective detector and/or a higher-harmonic rejection mirror coated with rhodium for which only low-enough energy photons experience total external reflection and are not attenuated (as done at X23B) is needed if having a single energy is experimentally important. Additionally, in order to keep the photon energy selected as constant as possible water-cooling is typically employed to reduce monochromator lattice expansion due to heating caused by the x-rays.

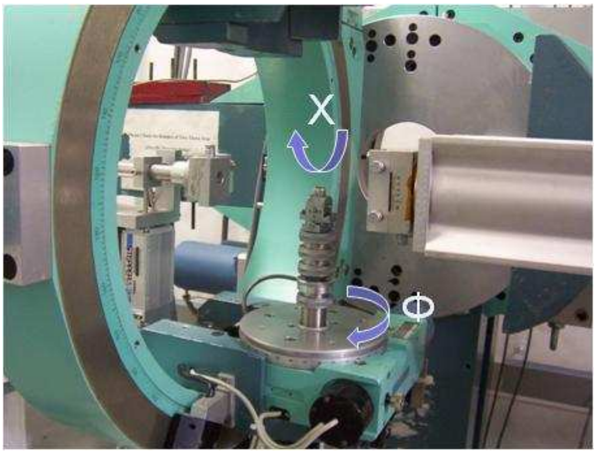

Figure 2.10: Additional Beamline Rotations

Entrance and slits just before the monochromator limit the total angular acceptance (3 and 1 milliradians at X6B and X16C, respectively, for example). Choosing the acceptance is a trade off between coherence length of the selected photons and the flux. Exit slits after the monochromator also limit angular dispersion observed at the sample, and are typically set equal to the entrance slits.

It's useful to keep the transverse and longitudinal coherence lengths in mind when looking at signature peaks from a spatially extended object. These are expressed as [26]

$$C_{\text{longitudinal}} = \frac{\lambda}{2\Delta\lambda} \tag{2.36}$$

and

$$C_{\text{transverse}} = \frac{\lambda R}{2D}. \tag{2.37}$$

R is the distance from the source to the point of detection, while D is the transverse distance between points within the source.

Since the beam is divergent one or more vertical and or horizontal refocusing mirrors are typically added. In the case of X6B a single cylindrically bent mirror allows the beam to be refocused to 0.3 mm^2 at a sample position 22.6 m downstream of the synchrotron exterior. Similar beam sizes exist at the sample holders of X16B and X16C, while the unfocused beam at 6-ID-B is roughly equivalent to the focused beam at X16B.

The x-rays travel along an enclosed, evacuated path for both safety and to reduce attenuation. For hard x-rays, however, it is easier to work with samples outside vacuum, and this is accomplished within a hutch designed to keep people from directly interacting with incoming x-rays. Within this last leg of the beamline a series of slits are used to achieve the desired level of collimation and keep the incident beam contained within the sample boundaries. One or more high voltage ion chambers also sample the charged particles produced by the passing beam. This provides a means to measure the incident intensity prior to interacting with the sample in order to normalize incident intensity fluctuations. Additionally, absorption for a transmission sample may be measured between the ion chambers. Standard foils may also be used in this manner for energy calibration based on the unique absorption edges of a selected element.

For samples supported by an impenetrable wafer (at least on the energy range used for these experiments of no more that 19 keV) reflectivity, fluorescence, or electron yield are the primary methods of measurement. For extended x-ray absorption fine structure acquired at X6B this was accomplished by measuring a sample in grazing incidence with a detector positioned at $\frac{\pi}{2}$ radians from the incident beam along the horizontal plane so as to effectively cut any elastic scattering, while still observing the isotropic fluorescence signal. For diffraction and specular reflectivity measurements at X6B, X16B, and 6-ID-B the sample was mounted on a Huber diffractometer with various degrees of freedom. The sample tilt along the beam axis is referred to as θ, the vertical detector angle with respect to the incident beam as 2θ which is not necessarily set equal to twice θ. The tilt perpendicular to the beam axis is χ, and the remaining "in-plane" sample rotation is ϕ, Figure 2.10. The motion of χ allows non-specular Bragg peaks to be probed. At X16C only the detector has motion along two-theta while sample placement and tilt are set manually.

For extended x-ray absorption fine structure and anomalous diffraction at X6B a solid state, Si, photon-counting Ketek detector with energy discrimination on the order of 200 eV was used to reduce background fluorescence and higher-order diffraction. At X23A a photon-counting Si Canberra detector was used in conjunction with a higher harmonic rejecting rhodium plated mirror. The remaining detectors used include an ion chamber at X16B for non-resonant specular reflectivity and diffraction, a Bruker Smart 1000 CCD for texture analysis at X6B, a photodiode for limited diffraction work at X16C, and a Cyberstar energy-sensitive (also to 200 eV) solid state photon-counting detector for additional anomalous diffraction at 6-ID-B. Additionally, slits in front of the detectors were used to select the angular measurement per point. These were generally set to 0.04 $\AA^{-1}$ for specular reflectivity and to 0.1 $\AA^{-1}$ for broadened polycrystalline Bragg diffraction peaks.

Finally, we turn to the soft, x-ray circularly polarized beamline at U4B. As noted the polarization was selected to be either linear (center of emitted beam) or set to 90 ± 5 % circular polarization by virtue of selecting the portion of beam above the synchrotron orbit plan with a vertically tunable mirror. Instead of using a Si [111] crystal monochromator as before, this experiment completed in the 700 to 900 eV range (covering the Co, Ni, and Cu L-edges) utilized a grating made of gold coated Si crystal holographically etched with 600 lines/mm, providing an energy resolution of up to $\frac{\Delta E}{E} = 10^{-4}$ to 10^{-3}. Entrance and exit slits were opened to 50 microns to increase flux. This set the final energy resolution to 0.42 eV for the Co L-edges, and 0.50 eV for the Ni L-edges.

At U4B three beam line chambers are available for electron yield measurement, scattering, and magnetic transmission. The last endstation located 20.8 m from the source was used for all x-ray magnetic circular dischrosim measurements. The spot

Table 2.1: Summary of x-ray beamlines used in data collection

Beamline	Techniques	Unique Features
X6B	Diffraction, EXAFS, Texture	CCD Camera Option
X16B	Specular Reflectivity	
X16C	Diffraction	
X23B	EXAFS	High harmonic mirror rejection
U4B	XMCD	Circular Pol., Magnetic Field
6-ID-B	Anomalous Diffraction	High photon flux (10^{12} ph/s)

size at the sample position was about 1 mm wide by 0.25 mm high. The samples all had transmission windows of 1 mm^2 Si_3N_4. Transmission was measured with a photodiode place just behind the samples, and beam normalization was acquired by measuring the current generated on a gold mesh grid placed within the beam path, approximately 0.5 m before the sample. Samples nominally normal to the incoming beam could be rotated freely within the horizontal plane as well as translated vertically. Magnetic fields could be pulsed up to 8.3 kG and continuously generated up to 6 kG by means of water-cooled electromagnets. These fields could be produced either along the beam direction or rotated horizontally by 45^o, for perpendicular and in-plane (sample also rotated by 45^o in the latter case) magnetization, respectively. In the 45^o geometry a correction of $\sqrt{2}$ was applied to the circularly polarized data in relation to any non-polarized measurement in order to rectify the geometry with the perpendicular case. For all geometries instead of changing circular polarization helicity, magnetic fields were switched back and forth by reversing the flow of applied current in order to collect magnetic dichroism.

Chapter 3

Multi-wavelength Overlapping and Interfering Diffraction Separation (MOIDS)

The magnetic behavior and anisotropy of ultra-thin films and nanoscale structures often varies dramatically with thickness and/or shape. The extent to which these magnetic changes are dependent on the surface to bulk ratio (Neel-type interface effects) versus strain induced changes of magnetic orbital moments and related spin-orbit coupling (magneto-elastic anisotropy energy) is often influenced by subtle structural details. Unlike magnetic spectroscopy for which there are many techniques available (x-ray magnetic circular dichroism, ferromagnetic resonance, magneto optical Kerr effect, super conducting quantum interference, *etc.*), detailed structural techniques that probe beyond the surface become difficult to perform in ultra-thin regions. Situations in which the layer of interest is buried, for example whenever transition metals are capped to prevent oxidation, and cannot be reached by surface limited imaging methods such as transmission electron microscopy and photo emission electron microscopy motivate further development of element specific x-ray diffraction.

3.1 Thin Film Challenges

Beyond simply decreasing the amount of material present, thereby decreasing the intensity proportional to the number of scattering centers squared, ultra-thin films and nanostructures face several unique obstacles in applying diffraction to solve their crystalline structures. The first is that an ultra-thin region is at high risk of undergoing strain induced structural modification arising from increased contact with neighboring layers. This is especially relevant in situations where these neighboring layers are chosen such that in their bulk form they nearly lattice match that of the ultra-thin region, and some degree of lattice matching can occur in one or both of the regions involved. The result is that the signature Bragg peaks used in structure determination may become so overlapped that they can no longer be resolved into their individual components.

The second challenge involves the smearing out of diffracted intensity over an increased area in reciprocal space with decreasing thickness. This effect is particularly

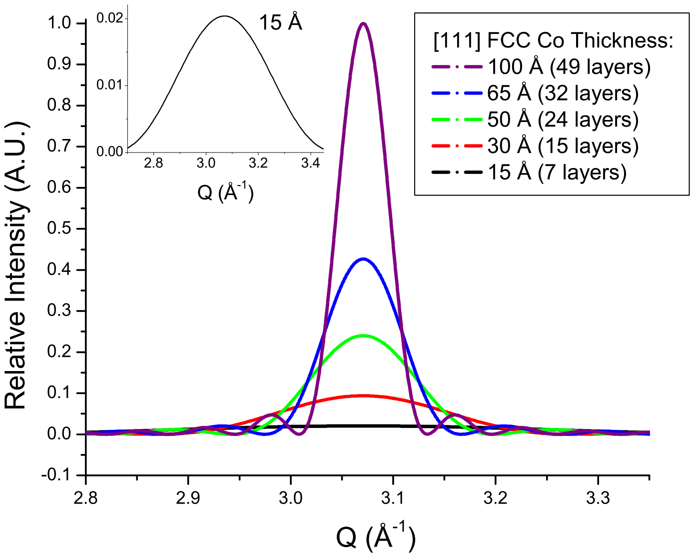

Figure 3.1: Simulated Debye broadening from the [111] face centered cubic Co reflection in specular reflection geometry for a range of thicknesses. The inset demonstrates that although the 15 $\AA$ layer appears almost flat in comparison with diffraction profiles from thicker regions, it is in fact nearly Gaussian, just stretched out in reciprocal space.

prominent for layers of 50 $\AA$ or less. In films it is known as Debye broadening [62], and it's a geometrical result of combining spherical waves from a limited number of scattering centers. Figure 3.1 illustrates this effect by simulating scattering from Co planar films of 100 $\AA$ and less. The resulting diffraction profiles are derived from a bulk, unstrained [111] face-centered cubic layer probed in specular reflection geometry.

The third and most difficult challenge to ultra-thin films arises from interlayer interference as will be discussed next in detail.

3.2 Mechanics of Interference

Whenever coherent scattering from multiple centers exist the superposition of their wave fronts, running the gambit from constructive to destructive interference, provides indirect information about their spatial distribution. In diffraction this is precisely what accounts for the characteristic Bragg scattering peaks at specific reciprocal space values. The placement of the peak center reflects the average spacing between scattering centers (whether from atoms or nanostructures), while the width of the peak is defined by the spatial extent over which the scattering centers form continuous regions of periodic structure. Interference is therefore not only commonplace, but is in fact the very basis of x-ray structural probes.

In macro-sized systems interference arising from the interaction between heterogeneous regions of different lattice spacing is typically negligible. In such cases the total diffracted intensity is well represented as a sum of intensity profiles from each constituent jth region as

$$I_{\text{noninterference}} = \sum_j I_j \prec \sum_j |f_j \mathbb{S}_j|^2 \tag{3.1}$$

where the individual intensity profiles are defined by equations 2.7, 2.22, and 2.24. If by some mechanism, such as Debye broadening, the scattering from one or more distinct homogeneous regions considerably weakens, this opens the door for interference between heterogeneous regions to assume a more prominent role. Under these circumstances the full form of the scattering must be employed as

$$I_{\text{total}} \prec |\sum_j f_j \mathbb{S}_j|^2. \tag{3.2}$$

This results in an additional two interference terms between each inter-region pair, I_{int1} and I_{int2}. If we denote two interfering regions x and y then the interference terms become

$$I_{\text{int1}} = 2|f'_x f'_y + f''_x f''_y|^2 |\mathbb{S}'_x \mathbb{S}'_y + \mathbb{S}''_x \mathbb{S}''_y|^2 \equiv |f_{\text{int1}}|^2 |\mathbb{S}_{\text{int1}}|^2 \tag{3.3}$$

and

$$I_{\text{int2}} = 2|f'_x f''_y - f''_x f'_y|^2 |\mathbb{S}''_x \mathbb{S}'_y - \mathbb{S}'_x \mathbb{S}''_y|^2 \equiv |f_{\text{int2}}|^2 |\mathbb{S}_{\text{int2}}|^2. \tag{3.4}$$

As discussed in chapter 2 single primes denote the real part and double primes the imaginary part of the atomic scattering factors, f, and of the structure factor, $\mathbb{S}$.

To illustrate how inter-region interference works in conjunction with Debye broadening a second, adjacent layer of [111] face centered cubic Cu is added into the simulation discussed above. Co and Cu have naturally similar face centered cubic lattices of 3.544 and 3.6147 $\AA$, respectively. In reciprocal space their unstrained [111] face centered cubic orientations reside at 3.07 and 3.01 $\AA^{-1}$, respectively, a separation easily resolved with diffraction for films of moderate thickness. Figure 3.2 shows through simulation how the Cu-Co thin film interference evolves as the constituent Cu and Co layers are simultaneously decreased from 1000 to 10 $\AA$. For 10 $\AA$ films the individual Bragg peaks are no longer resolvable and the observed intensity is dominated by interference.

Interference is largely dependent on the reciprocal space overlap of its contributing regions, and therefore strain induced lattice matching also increases interlayer interference in much the same way that increasing overlap though Debye broadening does. This is depicted in Figure 3.3 for 100 $\AA$ each of face centered cubic [111] Co and Cu simulated at an off-resonance energy of 7.3 keV. The peak height of the Co is smaller than the Cu of equivalent thickness primarily because the Co has fewer scattering electrons per atom than does Cu. As the [111] lattice spacing of the Co is varied from its bulk value to that of unstrained Cu, the interference between the two is enhanced correspondingly.

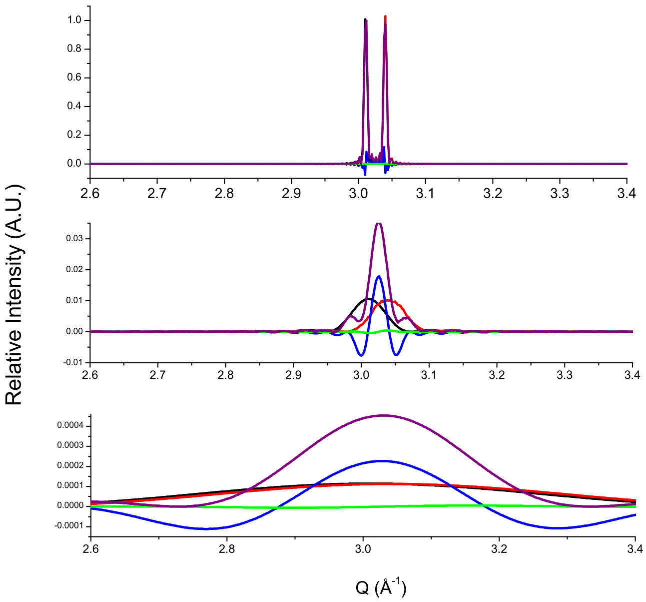

Figure 3.2: Simulated interference as a function of face centered cubic Co and Cu thickness probed along the [111] orientation. Black curves show the pure Cu diffraction, red the pure Co diffraction, blue the first interference term, green the second interference term, and purple the total diffraction pattern as would be measurable in experiment. The three panels show Co and Cu scattering thicknesses of 1000 $\mathring{A}$ (top), 100 $\mathring{A}$ (middle), and 10 $\mathring{A}$ (bottom). Notice that in all cases the first interference (blue) dominates the second interference (green) to such a degree that the latter could be neglected entirely.

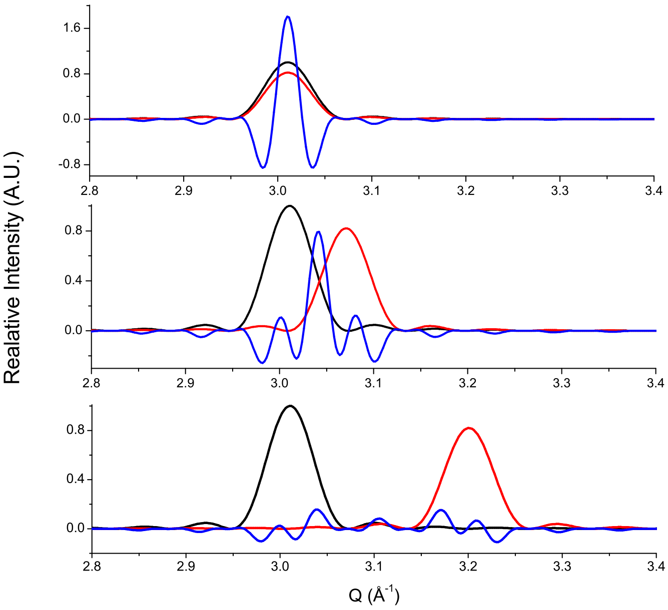

Figure 3.3: Simulated interference as a function of face centered cubic Co and Cu lattice spacing differences probed along the [111] orientation for 100 $\AA$ layers. Black curves show the pure Cu diffraction, red the pure Co diffraction, blue the combined interference terms. The three panels show Co lattices fully lattice matched to the Cu (top), midway between the nominal Co and Cu [111] values, and compressed by 4% such that the Co and Co have negligible overlap (bottom). As the lattices become more closely matched the interference increases correspondingly.

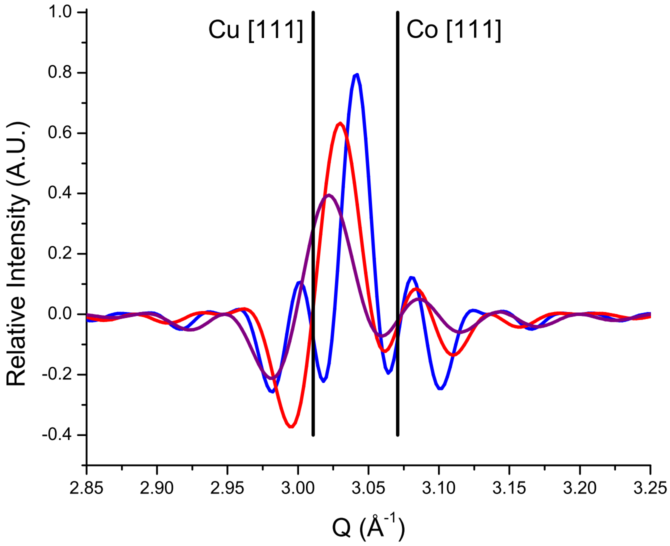

Figure 3.4: Simulated interference as a function of relative thicknesses for unstrained Co and Cu probed along the [111] face centered cubic orientation. The Cu is held at a fixed 100 $\AA$, while the Co is set at 100 $\AA$ (blue), 50 $\AA$ (red), and 25 $\AA$ (purple). All curves reflect the total interference generated from the Co and Cu layers. Notice how the the placement of the interference shifts away from the Co and toward the nominal Cu lattice spacing, depicted by black vertical lines.

Additionally, the location of the interference peak is highly variable and is a function of the relative coherent size of each contributing region. This is simulated in Figure 3.4 for decreasing Co thicknesses combined with constant Cu layers of 100 $\AA$. Here each layer spacing is held constant at its nominal, unstrained [111] value. As the Co is thinned relative to the Cu layer, the interference peak shifts toward the more dominant Cu diffraction, as intuitively expected. The dependence of the interference height and placement on the coherent thickness and spacing of the constituent scattering layers makes identifying and subsequently removing it that much more difficult.

Given the influence on the observable diffraction pattern that interference can have, observing a single peak where two would nominally be expected could be attributable to a host of conditions. It might reflect a change in one or more lattice spacings, the disappearance of a weak peak resulting from a high degree of Debye broadening, or an overwhelmingly large interference contribution. Thus, it can be quite difficult to quantify the structure of an ultra-thin, buried layer when nearly epitaxially matched to thicker neighboring region(s) since little can be assumed *a priori* about the ultra-thin layer strain, roughness, or even coherent thickness.

3.3 Roughness

In the simulations presented thus far, idealized smooth interfaces and fully coherent regions without defects, intermixing, or roughness have been used. It is a fair question to ask if such prominent interferences exist in real world ultra-thin layers, especially when these regions undergo disproportionate induced strain and often form polycrystalline regions. While it is true that any roughening mechanism does reduce diffraction intensity from all constituent regions involved, the underlying question becomes what is the magnitude of the interlayer reduction in comparison with the amount that the intralayer peaks experience. The short answer is that interference is fairly resilient to internal roughness, but not so to interlayer defects.

To illustrate the roughness characteristics, the use of adjacent [111] face centered cubic Cu and Co layers of 100 $\AA$ each continues to be a reasonable choice. The case in which each layer is continuously varied in spacing from being fully lattice matched at the Cu-Co interface (to an average Co and Cu spacing value) to reaching their respective nominal bulk values at the opposite free sides is shown in Figure 3.5, top. In the lower panel a per layer roughness equal to one third the nominal lattice spacing is applied to unstrained Cu and Co layers. The middle panel of Figure 3.3 by comparison shows what full interference from equivalent, unstrained Co and Cu layers without any roughness would be. In both roughening examples the total scattering intensity and interference effect are reduced, but the relative importance of interference within the observable diffraction is by no means diminished.

Under conditions of reasonably large strain it may become energetically favorable for a layer to break into smaller crystallite regions. Polycrystalline, ultra-thin films are not uncommon and result in the redistribution of diffracted intensity out in reciprocal space into a diffuse spots or rings. Concurrently the inter-layer interference becomes effectively limited to adjacent crystallites. While the interference in fact becomes magnified in proportion to the scattering from any single crystallite due to decreased coherent thickness and increased Debye broadening, the shear number of contributing crystallites, most of which don't participate in interlayer interference, also increase within a given region as their crystallite size decreases. The result of these two competing effects is shown for the 100 $\AA$ Co and Cu layers broken into chucks of 50 (top) and 33 (bottom) $\AA$ crystallites in Figure 3.6. A decreasing crystallite size (of a constant total layer thickness) does attenuate the relative magnitude of interference peaks. Even for a 100 $\AA$ layer broken into chunks one third its total thickness, the interference remains non-negligible.

The most detrimental effect on interference comes from the variation between regions. This can't be too pronounced if neighbor induced straining occurs (a typical thin-film outcome), but over a large number of crystallites, possibly with various degrees of texturing, slight interface roughness could occur. Even the deposition process itself in which there may be a 20 or 30 second delay between switching of depositing materials allows for additional oxygen displacements to form preferentially between heterogeneous regions. The average spacing between crystallites at an interface may then vary on the order of up to the lattice spacing itself. The average of small in-

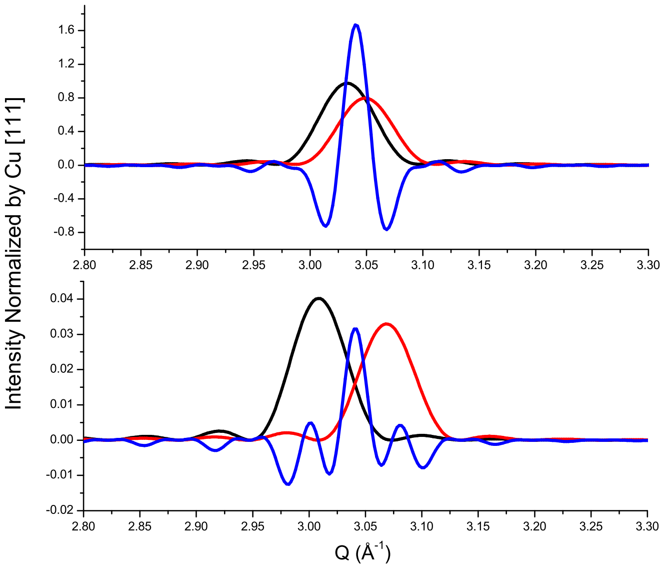

Figure 3.5: Effect of Intrinsic Roughness on Interference. Top panel simulated a situation in both layers fully lattice match to a common value at their interface and smoothly relax to their bulk values by the other edge. Bottom panel show the effect of an internal roughness equal to one third the nominal lattice spacing. In both cases the interference remains a significant contributor.

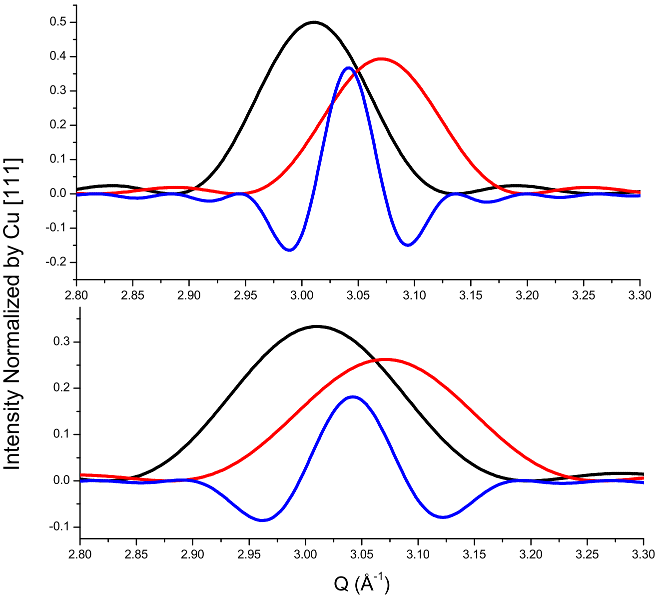

Figure 3.6: 100 $\mathring{A}$ Co and Cu layers broken into chucks of 50 (top) and 33(bottom) $\mathring{A}$ crystallites. A decreasing crystallite size (at a constant total thickness) does attenuate the relative magnitude of interference peak to some degree.

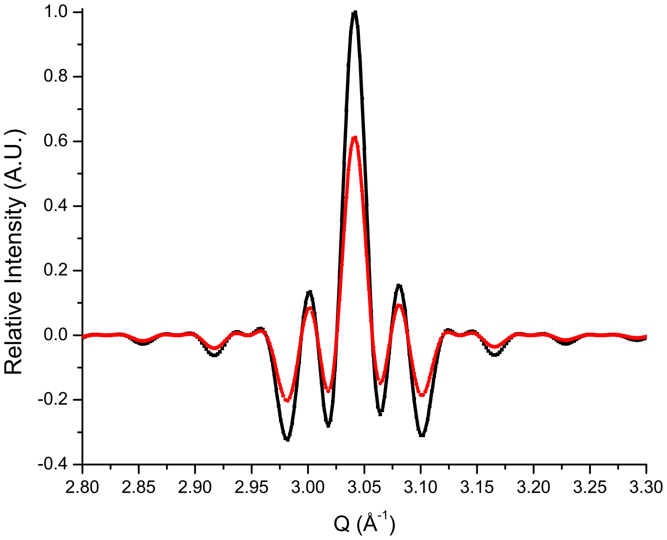

Figure 3.7: Interlayer roughness can cause a major decrease in interference. Black curve simulates the full interference from 100 $\mathring{A}$ each of Co and Cu. Red curve shows the effect of adding interlayer shifts of just ± 0.3 $\mathring{A}$. The shape is conserved, but the magnitude of the interference is diminished, while the diffraction of the pure material remains nearly constant.

terlayer shifts on the order of ± 0.3 $\mathring{A}$ is shown in Figure 3.7 compared to a single interference without any disorder. While the same interference shape is retained, the magnitude is noticeably decreased. By ± 0.5 $\mathring{A}$ shifts the interference becomes negligible.

Although the effects shown here by no means encompass all roughening mechanisms or possible combinations thereof, these simulations give a flavor of how interference behaves. Through interlayer roughness and breaking of layers into crystallites interference may be damped to some degree, but it is still likely to play a significant role in ultra-thin films. This finding will be confirmed in the next chapter via experiment on polycrystalline ultra-thin films.

3.4 Anomalous Diffraction

The idea behind anomalous diffraction, *i.e.* scattering immediately around an absorption edge of interest, is to obtain a maximal change in scattering intensity for one atomic species over a short span of energy, while the rest of the atomic scattering factors remain nearly constant. The working assumption is that any change in the total scattering can to a very good approximation be attributed solely to the resonant atom. Thus, anomalous diffraction works best when all of the following conditions

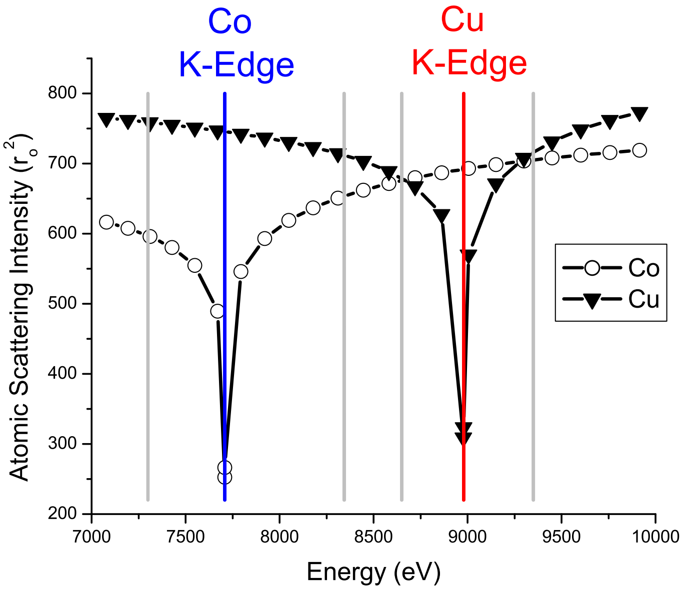

Figure 3.8: Anomalous Scattering of Co and Cu about their K-edges.

are met: A) an absorption edge unique to the material of interest is available and the diffraction at this energy falls into an appropriate range of reciprocal space, B) the slight scattering changes associated with any dominant and overlapping, but non-resonant regions are negligible compared to the change in resonant material to be probed, and C) interlayer interference features involving the resonant material are also negligible compared with the pure signal to be extracted.

A model system comprised of non-interfering 80 $\AA$ Cu and 65 $\AA$ Co meet all the above criteria for anomalous diffraction. Figure 3.8 demonstrates how their respective scattering factors change as a function of energy. Figure 3.9 displays the simulated net scattering at 7.3 and 7.709 keV (below and at the Co K-edge absorption edge), while the inset shows the difference in scattered intensity between these energies. Without interference the original Co peak profile (see inset) is easily extracted.

The addition of interlayer interference, however, changes the outcome completely. Figure 3.10 shows the net scattering of the Cu, Co, and their interference over the same energies as chosen above. Subtraction of the Co K-edge diffraction from the non-resonant energy shows a double peaked feature (see inset). Even if one understood that the lower Q peak was a derivative of interference, it would be easy to mistake the second, smaller feature for the pure Co scattering. Fitting the double featured anomalous difference with two Gaussians, Figure 3.11, appears to provide a reasonable fit. However, the extracted Co in this scenario is shifted to a higher Q region than truly represents reality. The key to notice is that its full width half maximum (FWHM) is smaller than what would be expected from Debye broadening and, therefore, cannot

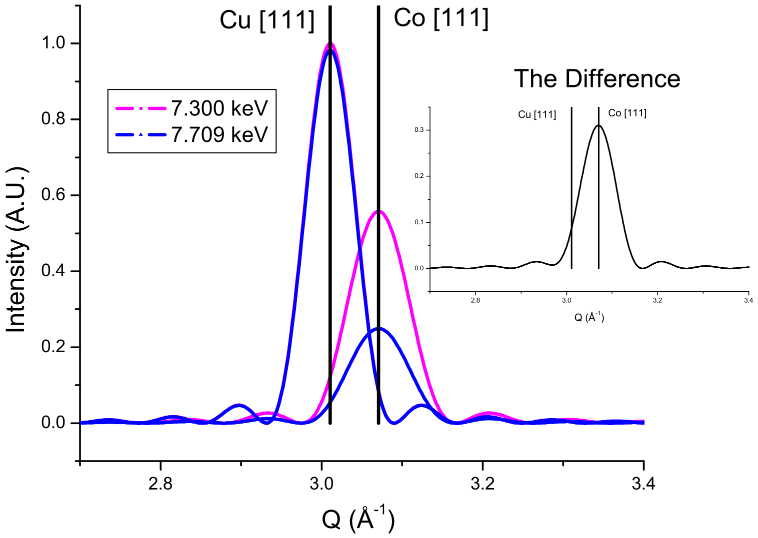

Figure 3.9: Scattering from 80 $\mathring{A}$ Cu and 65 $\mathring{A}$ Co are shown off-resonance at 7.3 keV (pink curve) and on the Co K-edge (blue curve). Without interference the difference between the two diffraction patterns easily reconstructs the pure Co scattering shape (inset) even though substantial overlap between the Co and Cu was observed.

be taken at face value. In fact, the period of an interference is shorter than either of its two contributing layers. Therefore, if overly large it has the tendency to decrease the apparent FWHM of the pure peaks as well. Thus, the FWHM serves as a good marker as to whether an interference and pure peaks can be well approximated by two Gaussians or not.

3.5 Mathematical Details of MOIDS

Given the spatially diverse systems one might encounter, a general purpose method is desired that would yield a unique solution for all scattering regions of interest, while not requiring *a priori* knowledge about crystalline structure or spatial distribution. The technique would ideally be applicable to seemingly different situations as those involved in crystalline structure and strain (angstroms), nanoparticle shapes (nanometers), and nearest-neighbor nanostructure packing (nanometers to microns). It also should not be limited to surface structure for which adequate structural techniques already exist. Most importantly it would fully account for and separate the energy-dependent scattering changes from all contributing regions and their interferences. One response is to solve directly for the scattering profiles of each and every material-defined region and accompanying interferences by taking into account a sufficient number of energy-dependent diffraction patterns simultaneously.

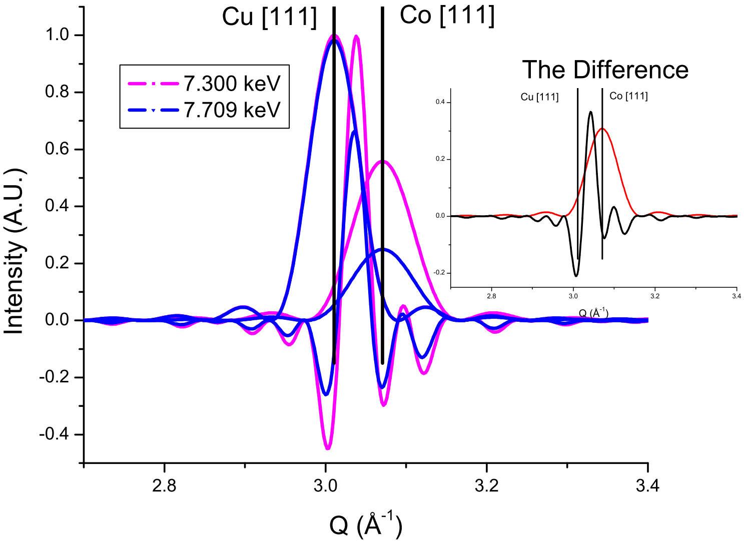

Figure 3.10: Scattering from 80 $\mathring{A}$ Cu, 65 $\mathring{A}$ Co, and their interference are shown off-resonance at 7.3 keV (pink curve) and on the Co K-edge (blue curve). The difference between the two diffraction patterns (inset) clearly indicates that contributions from both the desired pure Co (red) and the undesired Co-Cu interference (black) are extracted. Here it is easy to tell them apart, but combined as would be observed in an experiment would make it more difficult to distinguish them.

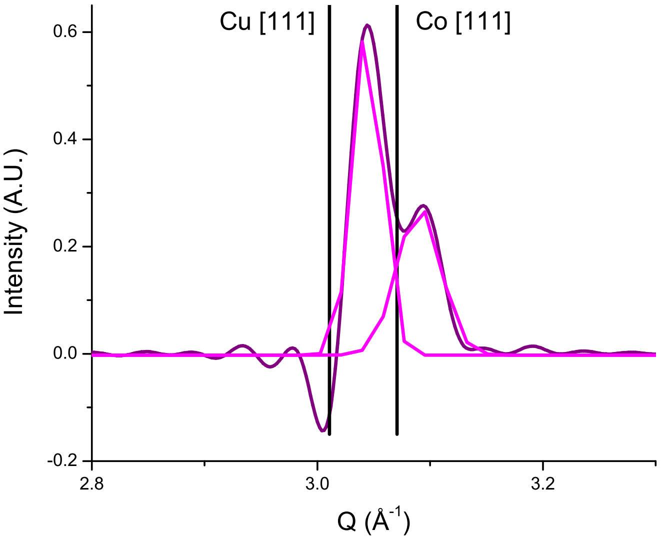

Figure 3.11: The total anomalous difference as given in Figure 3.10 is displayed in purple. Even if an observer realized it contained both an interference term as well as the pure Co scattering, fitting the anomalous difference with two Gaussian peaks (pink curves) would not be a good solution. The interference is so intense here that this method would shift the "Co" peak to higher Q than it actually sits at.

The idea is similar to Multi-wavelength Anomalous Diffraction (MAD) [63, 64] in that it incorporates multiple energy-dependent scattering patterns in order to separate the real and imaginary element-dependent contributions. In the case of MAD this is done in order to retrieve both amplitude and phase of the scattering regions from which reconstructed images of the scattering regions can be made. In the current application the multiple diffraction patterns are used for both element specificity and to separate real and imaginary scattering components. However, instead of concerning ourselves with the relative phase differences, the real and imaginary separation provides information necessary to determine interference contributions which may positively or negatively impact on the total scattering profile. A major difference, however, is that the MAD technique must sample over a sufficiently large area in reciprocal space in order to reconstruct a two dimensional image, while the current method has an averaged, stand-alone solution for every point in reciprocal space. The experimental challenge of this new adaptation lies in applying it to ultra-small systems of low intensity where interference may far outweigh the peaks we desire to measure.

From here on the method developed within this dissertation will be termed MOIDS for Multi-wavelength Overlapping and Interfering Diffraction Separation. Each energy-dependent diffraction scan that differs significantly in at least one atomic scattering factor contained anywhere within the sample that contributes in a meaningful way to the scattering region of interest can be thought of as an additional linearly independent equation. That is, the energy-dependent, known atomic scattering factors are the coefficients, the structural factors the variables to be solved, and the experimentally measured diffraction intensities are the numerical inputs which depend on both energy and reciprocal space position.

To illustrate this more clearly let's start with the simplest case where more than one material involved undergoes a scattering change around an edge of interest. Instead of Co and Cu, a system could have some oxidation containing Co and CoO for instance. Or in the Co-Cu system the Co scattering may be so weakened from Debye broadening in comparison to the Cu that even very small changes in the Cu scattering dominates. In these cases a reasonable response would be to approach the problem algebraically at each point in reciprocal space from the following equations,

$$f_{\mathrm{Co}}\left(E_1\right) * \mathbb{S}_{\mathrm{Co}}\left(Q\right) + f_{\mathrm{other}}\left(E_1\right) * \mathbb{S}_{\mathrm{other}}\left(Q\right) = I\left(Q, E_1\right) \tag{3.5}$$

and

$$f_{\mathrm{Co}}\left(E_2\right) * \mathbb{S}_{\mathrm{Co}}\left(Q\right) + f_{\mathrm{other}}\left(E_2\right) * \mathbb{S}_{\mathrm{other}}\left(Q\right) = I\left(Q, E_2\right). \tag{3.6}$$

As long as the energy-dependent scattering factor behavior for each material are known, $\mathbb{S}_{\mathrm{Co}}$ and $\mathbb{S}_{\mathrm{other}}$ could both be solved.

For cases involving more than two scattering terms, a better strategy would be to employ matrix algebra. Scattering contributions from two materials, say Co and Cu, and their interferences, could be solved by four diffraction equations taken at four distinct energies, E_1-E_4, as:

$$\underbrace{\begin{bmatrix} f_{\text{Co}}(E_1) & f_{\text{Cu}}(E_1) & f_{\text{Int}_1}(E_1) & f_{\text{Int}_2}(E_1) \\ f_{\text{Co}}(E_2) & f_{\text{Cu}}(E_2) & f_{\text{Int}_1}(E_2) & f_{\text{Int}_2}(E_2) \\ f_{\text{Co}}(E_3) & f_{\text{Cu}}(E_3) & f_{\text{Int}_1}(E_3) & f_{\text{Int}_2}(E_3) \\ f_{\text{Co}}(E_4) & f_{\text{Cu}}(E_4) & f_{\text{Int}_1}(E_4) & f_{\text{Int}_2}(E_4) \end{bmatrix}}_{Known\ Coefficients} \underbrace{\begin{bmatrix} \mathbb{S}_{\text{Co}}(Q) \\ \mathbb{S}_{\text{Cu}}(Q) \\ \mathbb{S}_{\text{Int}_1}(Q) \\ \mathbb{S}_{\text{Int}_2}(Q) \end{bmatrix}}_{Variables\ To\ Solve} = \underbrace{\begin{bmatrix} I(Q,E_1) \\ I(Q,E_2) \\ I(Q,E_3) \\ I(Q,E_4) \end{bmatrix}}_{Numerical\ Inputs} \tag{3.7}$$

Parentheses indicate energy and/or reciprocal space dependence. Upon reduction to a diagonal matrix the material-specific structure factors can be read off numerically. Each structure factor distribution contains the location and shape of the Bragg peaks of a given material, which in turn contains information about the lattice structure, average directionally-dependent strain, effective coherence of crystallites, and/or size-shape defined scattering from nanoparticles, depending on the system being studied.

Additional materials or non-negligible interference terms may be accounted for by addition of more independent, energy-based diffraction patterns, expanding the matrix by that many more dimensions. Although a multilayer and all its possible interference terms may seem to require an unwieldy number of energies, rarely would more than a couple of the layers have meaningful diffraction changes in any small region in reciprocal space. As will be shown in the following sections a background comprised of materials that vary little over the range of energies used will have minimal affect on the extracted profiles, and in most cases can simply be ignored without consequence.

3.6 Reconstruction and Noise

With adequate machinery in place, let us now return to the most challenging situation for which direct anomalous subtraction failed – the case in which Co and Cu produced significant interference. To fully account for the Co, Cu, and both resulting interferences four energy-dependent diffraction patterns are needed, and this requirement could be fulfilled by the energies 7.3, 7.709, 8.650, and 8.979 keV, for example. Simulated input diffraction scans for a 80 $\AA$ Cu | 65 $\AA$ Co | 80 $\AA$ Cu sample are shown in Figure 3.12. To better simulate experimental data (next section) each layer was broken into crystallites of 50 $\AA$. Interference between the Co and Cu was reduced by a factor of three by interlayer roughness. Applying MOIDS without noise of course results in the perfect reconstruction of each structure factor, as shown in the top section of Figure 3.13. Note that the differences in peak height from the full diffraction pattern are the result of removing the energy-dependent scattering factors (known coefficients) during the reconstruction process.

In order to access the robustness of the method, statistical uncertainty should be included as well as some inevitable background contamination. Adding a constant background of 20% of the maximum diffraction peak results in the reconstruction shown in the bottom panel of Figure 3.13. Although the resulting structure factors are shifted vertically, their main features and peak placement remain unaffected.

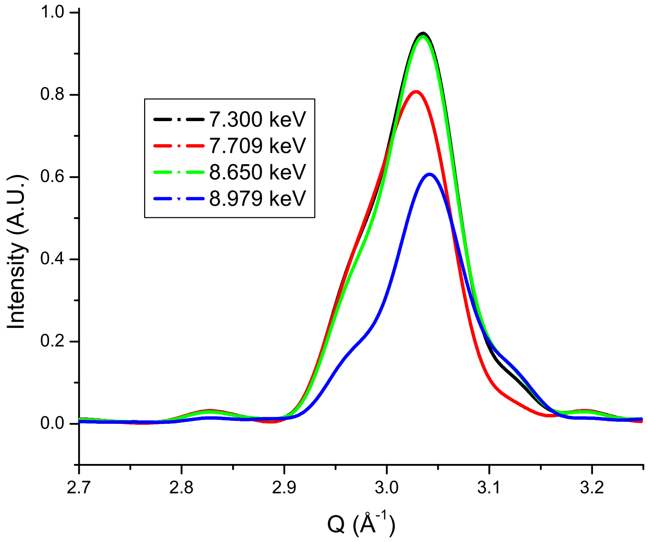

Figure 3.12: Simulated input anomalous diffraction patterns generated from a 80 $\AA$ Cu | 65 $\AA$ Co | 80 $\AA$ Cu sample with each layer broken into crystallites of 50 $\AA$. Co-Cu interference was suppressed by a factor of three with the inclusion of interlayer roughness.

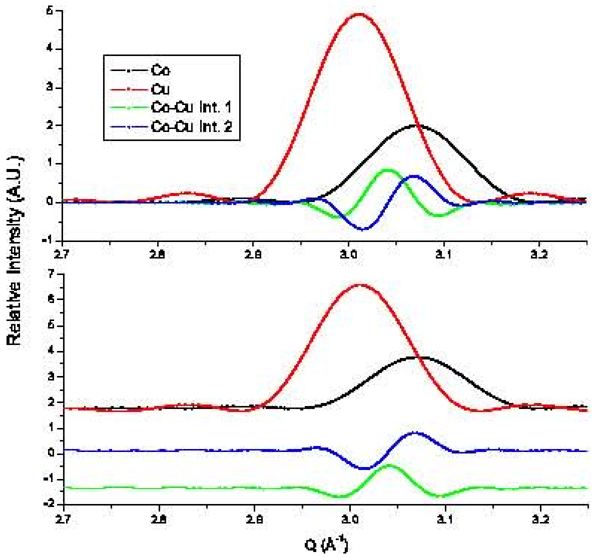

Figure 3.13: The four-energy MOIDS reconstruction of the Cu (red), Co (black), and their interference terms (blue and green). Note that the relative peak heights do not correspond to the diffraction patterns observed in Figure 3.12 as the atomic scattering factors have been removed during the reconstruction. Peak placement and distribution, however, are unaffected. Top panel shows a reconstruction from perfect input diffraction set, while the bottom panel includes an offset that is 20% the maximum diffraction height. Even with a large linear offset, reconstructed peak shape and placement are relatively unaffected.

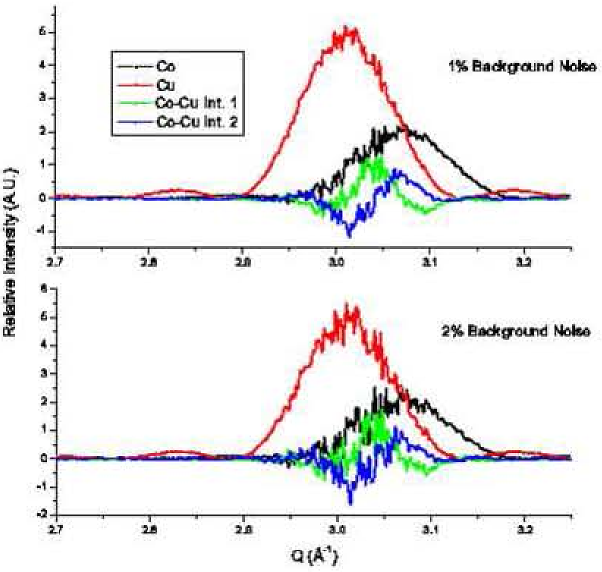

Figure 3.14: Simulated reconstruction as shown in the top panel of Figure 3.13, but with added statistical fluctuations of 1% (top) and 2% (bottom) on the total diffracted intensity inputs before reconstruction. The extracted structure peaks are still recognizable, although noisy, indicating the MOIDS method is fairly robust.

This explains why ignoring diffraction from layers which do not undergo significant energy changes or participate in interference with a resonant layer has little effect on the final result. Even including an unusually high statistical fluctuation of 1 or 2% of the total diffraction patterns does not cause the reconstruction to fail and still produces recognizable Co and Cu peaks, as shown in Figure 3.14. Thus, the reconstruction is relatively robust. However, care should be taken when working with weakly scattering, ultra-thin layers to reduce background noise to below that of the thin film Bragg peaks.

3.7 Including Too Few Terms

Including more scattering or interference terms generally is not a problem unless these extra terms also happen to undergo anomalous changes within the energy range used. If non-anomalous in nature, extra terms simply act like small linear offsets as shown in the bottom panel Figure 3.13. This further justifies neglecting terms that are relatively constant and do not participate in interference with an anomalous sources.

Obtaining high quality experimental data, especially for ultra-thin films, is a challenge experimentally with today's synchrotron sources. Therefore, the more realistic issue is what happens when too few energy-dependent diffraction scans are obtained. For instructive purposes, a simulation involving 50 $\AA$ Pt | 85 $\AA$ Cu | 65 $\AA$ Co | 85 $\AA$

Cu | 50 $\AA$ Pt samples of face centered cubic layers probed along the [111] orientation of each will be used. As in the previous simulation the layers are further broken into crystallites 50 $\AA$ thick such that the interference between the Pt and Co layers is negligible. The Pt-Cu and Cu-Co interferences are reduced by a factor of three as described in section 3.3 by inter-layer roughness. (These particular values are chosen to produce similar results to what was observed experimentally, as will be shown in the following section.)

If, for example, there were only three energy-dependent diffraction scans available, as simulated in Figure 3.15, then a full MOIDS simulation accounting for the Pt, Cu, Co, two Pt-Cu interferences, and two additional Cu-Co interferences clearly could not be performed. On the other hand, an approximate version of MOIDS, assuming the interference terms weren't too large, could be done. The best fit would redistribute the unaccounted changes in diffraction from interference terms into the material profiles that have the most similar changes with respect to energy. That is, the Pt-Cu interferences would be redistributed into the Pt and Cu reconstructed profiles, while the Cu-Co interferences would be placed with the reconstructed Cu and Co terms. An example of such an energy-limited reconstruction for the Co is shown in the bottom panel of Figure 3.16 using the input simulated diffraction profiles of Figure 3.15. Although the extracted "Co" profile doesn't completely match the true Co plus Cu-Co interference profiles (top panel), it produce a close version. In general, the less interference present, the better the reconstruction will be.

It is instructive to compare the limited reconstruction described above with more conventional anomalous diffraction in which one energy diffraction is simply subtracted from another. In both cases the tacit assumption of non-interference places actual interference contributions into the reconstructed profiles of the materials that undergo the most similar changes with energy. Therefore, the two methods should produce similar results, and in fact this is exactly what happens as modeled in Figure 3.16. This means the energy-limited MOIDS worked just as it should have within the (incorrect) assumption of no interferences. It also demonstrates once again that interference terms aren't necessarily negligible even in polycrystalline, thin films and must accounted for in some manner in order to get at the structure of thinner layers. Clearly, a full MOIDS reconstruction would be preferable when experimentally possible, but, as will be shown in chapter 4, simpler anomalous diffraction with interference explicitly accounted for can also provide useful structural information.

3.8 Experimental Verification

With knowledge of how the simulations should behave it is time to try the method out on real data. Three energy diffraction scans (7.300, 7.709, and 8.979 keV) were taken on two samples of 50 $\AA$ Pt|85 $\AA$ Cu|12 or 65 $\AA$ Co|85 $\AA$ Cu|50 $\AA$ Pt at the Advanced Photon Source, Mu-CAT 6-ID-B beamline with a flux of 10^{12} photons/second at 8 keV. Figure 3.18 shows the resulting energy-dependent scattering profiles for the thinner Co sample in specular geometry. This and in all other such energy-varied

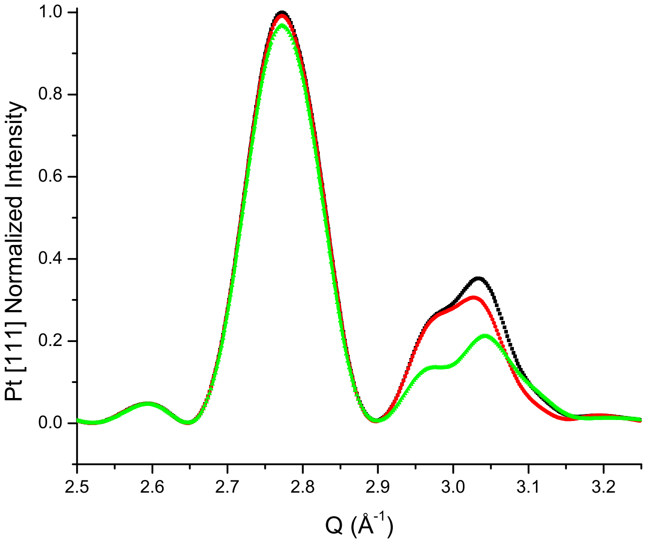

Figure 3.15: Simulated diffraction profiles for 50 $\AA$ Pt|85 $\AA$ Cu|65 $\AA$ Co|85 $\AA$ Cu|50 $\AA$ Pt broken into 50 $\AA$ crystallites. Interference terms have been additionally suppressed by a factor of three. Input energies used are 7.300 (black), 7.709 (red, Co *K*-edge), and 8.979 (green, Cu *K*-edge) keV.

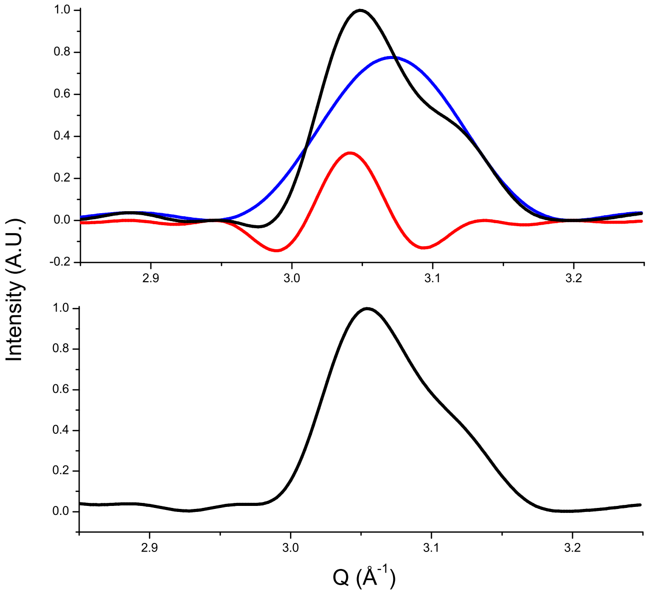

Figure 3.16: Simulated three energy-limited MOIDS reconstruction using the diffraction inputs given in Figure 3.15. Bottom panel shows the MOIDS reconstruction of Co within a non-interference assumption. In reality, the profile reflects both the pure Co scattering (blue curve, top panel) as well as the interference (red curve, top panel). If the interference and the pure Co contribution were simply combined (purple curve, top panel) it comes remarkably close to matching the energy-limited MOIDS reconstruction (bottom panel).

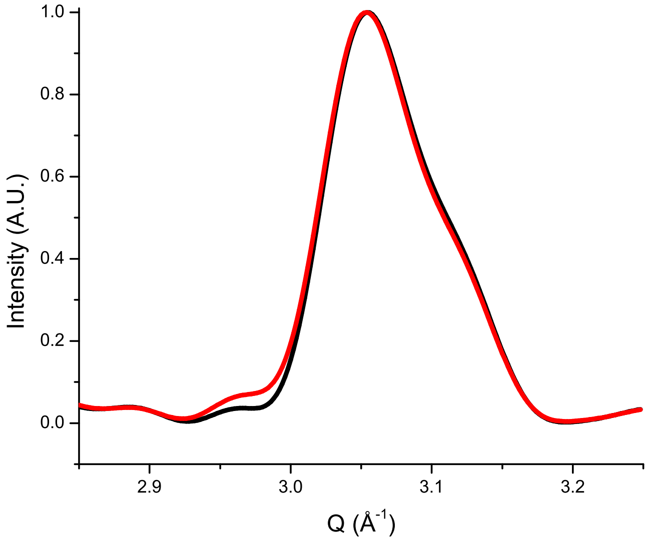

Figure 3.17: The energy-limited MOIDS Co reconstruction of Figure 3.16 is given in black, compared with anomalous subtraction of the Co K-edge (7.709 keV) from the non-resonant 7.300 keV diffraction profile as shown in Figure 3.15. The two are remarkably similar indicating that within the less-than-ideal non-interference assumption, the MOIDS again works properly.

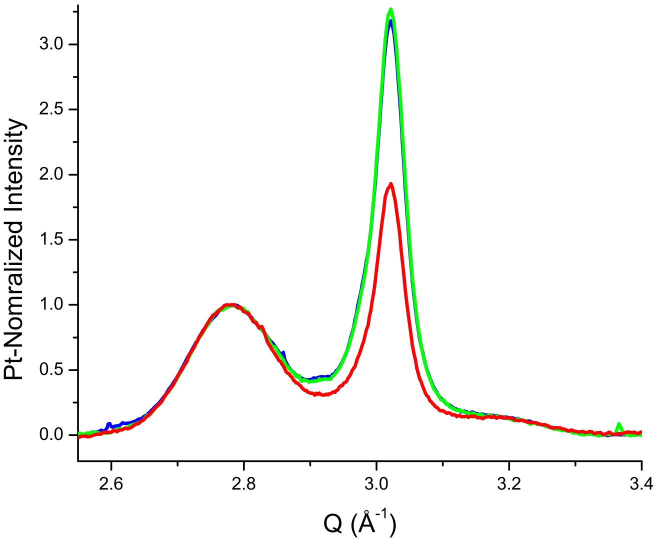

Figure 3.18: Experimental diffraction profiles for a 50 $\mathring{A}$ Pt|85 $\mathring{A}$ Cu|23 $\mathring{A}$ Co|85 $\mathring{A}$ Cu|50 $\mathring{A}$ Pt sample. Energies at which the diffraction measurements were performed are 7.300 (green), 7.709 (blue, Co K-edge), and 8.979 (red, Cu K-edge) keV. The blue and green curves are almost identical as the Co has little impact here. Notice how much larger the drop in diffracted intensity is at the Cu K-edge, indicative of how dominate the Cu and its interference terms are.

diffraction scans, the Pt [111] and [200] peaks with minimally changing, yet well defined scattering factors, serve as a convenient standard to which the spectra are normalized. Table **??** provides the new Pt-normalized Co and Cu scattering factors as reference, where the apparent drop in magnitude from the non Pt-normalized values arises from the fact that Pt is a very intense scatterer. Originally, a Kapton foil which scattered a small portion of the incident light into a second photon-counting detector was to be used for absolute beam normalization, but during the course of the week-long experiment at the Advanced Photon Source it appears to have been damaged by the intense beam. In principle, beam-monitoring ion chambers could have been used for normalization, but in order to account for energy-dependent efficiency changes the temperature, pressure, and fill gas would all have had to be carefully monitored and controlled. Therefore, a reference signal from within the sample was found to be the most convenient and reliable calibration standard available. Table 3.1 lists the Pt-normalized scattering factors, corresponding to the vertical lines in Figure 3.8, which will be utilized in MOIDS reconstruction.

It's worth mentioning that in anomalous-based scattering experiments locating the transition edges accurately is of the utmost importance if the scattering factors will be used in a quantitative manner because they change so rapidly near absorptions.

Table 3.1: Pt Normalized Co and Cu Scattering Factors

factor	7.300 keV	7.709 keV	8.344 keV	8.650 keV	8.979 keV	9.350 keV
Co f'	0.3277	0.2138	0.3435	0.3508	0.3568	0.3623
Co f''	7.101E^{-3}	0.05109	0.04575	0.04346	0.04119	0.03884
Co $\lvert f\rvert^2$	0.1074	0.04833	0.1201	0.1249	0.1290	0.1328
Cu f'	0.3694	0.3675	0.3616	0.3542	0.2399	0.3637
Cu f''	9.737E^{-3}	8.854E^{-3}	7.704E^{-3}	7.229E^{-3}	0.05261	0.04983
Cu $\lvert f\rvert^2$	0.1366	1352	0.1308	0.1255	0.06034	0.1348
Pt f'	0.9936	0.9946	0.9957	0.9961	0.9965	0.9969
Pt f''	0.1131	0.1042	0.09268	0.08789	0.08320	0.07845
Pt $\lvert f\rvert^2$	1	1	1	1	1	1

In this work, the desired transition edges were located by taking the derivative of the measured absorption from the constituent sample elements of interest. A double-check involved verifying that the diffuse scattering of the resonant atom was indeed at a minimum.

A double-check was performed by verifying at an area in reciprocal space away from any Bragg peaks that the energy selected indeed corresponded to a minimum in diffuse diffracted intensity.

As in the simulation of section 3.6, three energies can be used to solve for the Pt, Cu, and Co, while lumping the Pt-Cu and Cu-Co interferences into the structure factors of the materials with the most similar energy-dependence. Figure 3.19 shows the result of solving with an energy-limited MOIDS, assuming no interference is present. While MOIDS seems to do a reasonable job of reconstructing the Pt and Cu profiles, the Co is clearly dominated by Cu-Co interference given the sharp FWHM of its extracted peak. An up-close view of the extracted region, Figure 3.20, shows that is can be decomposed into two Gaussians, the latter of which has a FWHM expected for a 23 $\AA$ thick layer.

It is interesting to compare the energy-limited MOIDS with simple anomalous subtraction of the Co K-edge diffraction (7.709 keV) from the non-resonant 7.3 keV diffraction. As expected figure 3.21 shows the two return nearly the same results since both make the assumption of non-interference. Additionally, performing a similar procedure on the thicker Co sample of 65 $\AA$ also shows the three-energy MOIDS and anomalous subtraction again provide similar results and yield two Gaussian-like, overlapped peaks. The result is very much like the simulation created for a similar thickness of Co shown in Figure 3.16. As will be continued in chapter 4, a good check on the higher Q peak as a measure of the pure Co scattering is to make sure the FWHM is at least as wide as defined by Debye broadening, possibly larger if the sample is particularly rough or polycrystalline.

As a final note, a second week-long experiment at Mu-Cat 6-ID-B was conducted on similar samples using a full five energies (7.300, 7.709, 8.344, 8.979, and 9.350 keV) in order to account for the Pt, Cu, Co, and first interference terms of the Pt-Cu

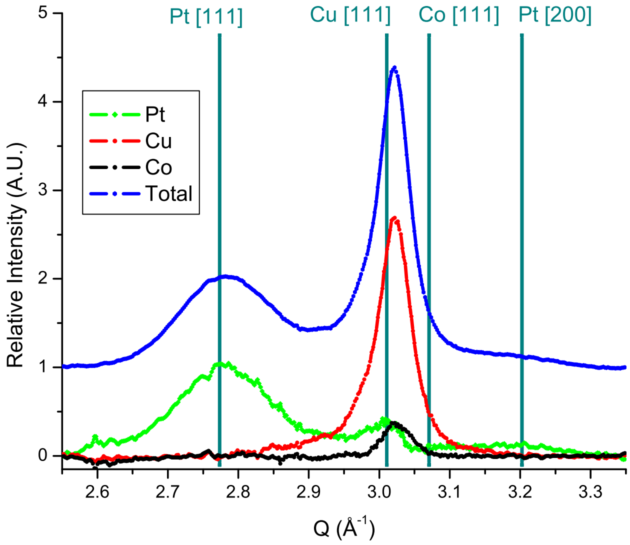

Figure 3.19: Energy-Limited MOIDS Reconstruction of 23 Å Co. Green illustrates the extracted Pt profile, red the Cu profile, and black the Co profile in which each extracted structure factor has been multiplied by its unique scattering factor at 8.344 keV. The blue curve is the sum of these extracted profiles, shifted up one unit for clarity, and matches the experimental input diffraction of this energy. The FWHM of the extracted Co, however, is too sharp to be attributable to a 23 Å layer alone.

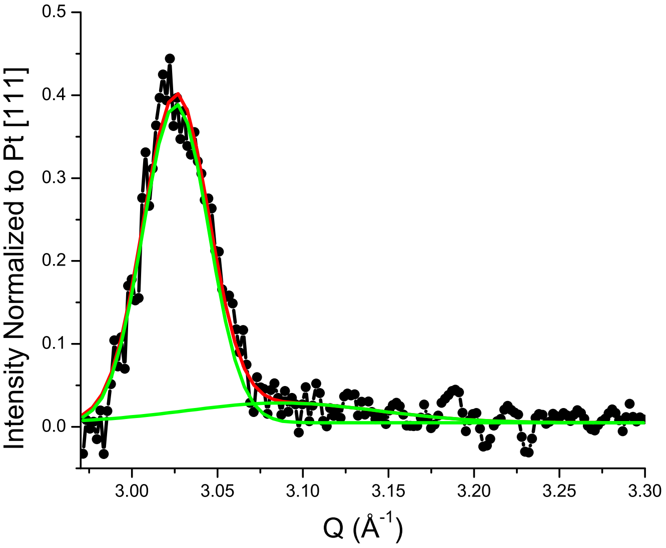

Figure 3.20: A close-up of experimentally extracted 23 $\AA$ Co peak shows that it can in fact be well fit with two Gaussians. The Gaussian at higher Q in fact has a FWHM consistent with a 23 $\AA$ layer.

and Cu-Co. Unfortunately, several days into the experiment the computer-controlled, beam-defining slits at times became ”glitchy” and would intermittently wander. The difficulty was overcome by eliminating computer control of the slits, and instead they were positioned manually by running a short intensity maximization program between each and every scan. This solution worked reasonably well, but small intensity fluctuations during the course of a single scan (on the order of 45 minutes) turned out to have as much variation as the difference in signal between the 7.3 and 7.709 keV scans. The root of the problem then was not that the sample was too thin to be well characterized, but rather the slit-to-beam drift was too large during the duration of a scan. Additionally, even after a linear background subtraction correction had been applied to energy 9.350 keV, a Bragg tail coming from the substrate became an issue. Due to limited beam time and slit issues, the experimental time was focused on determining in and out of plane strain differences using a less-than-ideal number of input energies. However, a future experiment involving a complete MOIDS reconstruction would be beneficial as a means to fully test the method's applicability in reconstructing ultra-thin, multilayered systems without any interference fitting required.

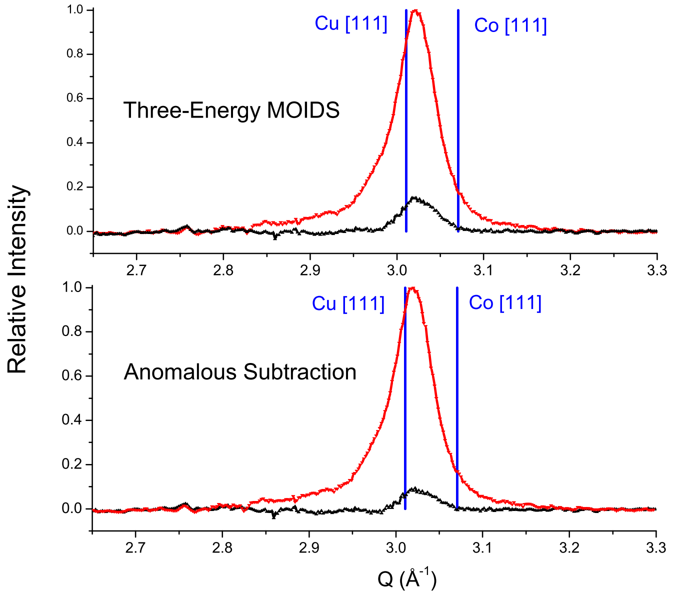

Figure 3.21: The three-energy MOIDS and the anomalous subtraction (8.344 - 7.709 keV for Co, 8.344 - 8.979 keV for Cu) look quite similar as predicted by simulation. Cu profiles are given in red; Co profiles in black. Although the Co appears to be lattice strained to the Cu on first glance, the majority of the extracted Co peak is in fact a Cu-Co interference.

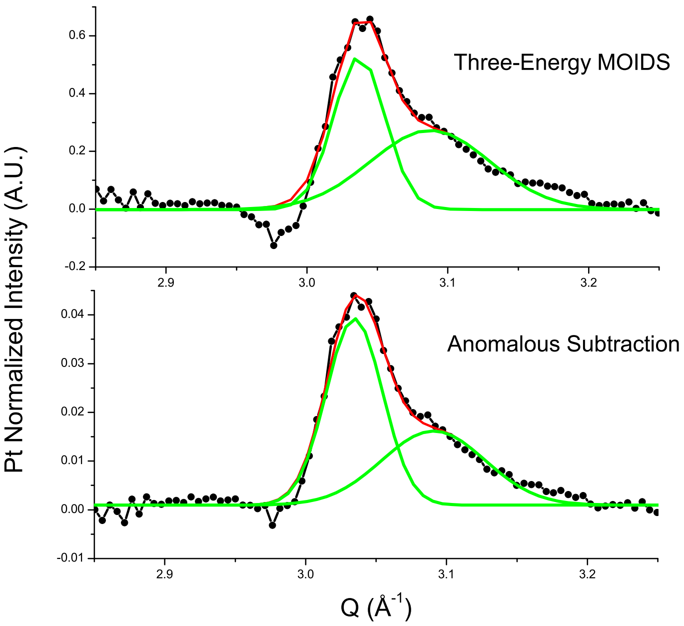

Figure 3.22: The three-energy MOIDS (7.300, 7.709, and 8.979 keV) and the anomalous subtraction (7.300 - 7.709 keV for Co) reproduce similar Co profiles for a 65 $\mathring{A}$ Co layer. The interference isn't as dominant as in the 23 $\mathring{A}$ example, Figure 3.21, but it is still clearly present. The FWHM of the wider Gaussian also matches the expected width for a 65 $\mathring{A}$ Co layer, indicating the latter probably well represents the true Co layer structure factor.

3.9 Can Interference Peaks Be Used Directly?

As has been observed via simulation and experiment, an interference involving a weak-scatterer can indeed be far stronger than the pure signal from weak-scatterer. In situations where the experimental signal is too noisy to obtain a direct reconstruction of the weak scatter it would be useful to be able to extract the information from the interference peak and the second (presumably stronger) interfering layer. Referring to equations 3.3 and 3.4 it becomes evident that the sum of each structural interference term squared is equal to a multiplication of the two interfering regions. In the case of Co and Cu, for example, this becomes

$$\mathbb{S}^2_{\mathrm{Int}_1} * \mathbb{S}^2_{\mathrm{Int}_2} = \mathbb{S}^2_{\mathrm{Co}} * \mathbb{S}^2_{\mathrm{Cu}}. \tag{3.8}$$

If one could measure both interferences and the larger of the pure regions, then solving for the remaining weaker Co peak would be easy.

The problem is that while the second structural interference is as large as the first interference (and can't be neglected for this application), the observed diffraction from the second interference is typically quite small due to its atomic scattering pre-factors (refer to equations 3.3 and 3.4 for details). Even in simulation, the second interference diffraction is always significantly weaker than the first interference due to that factor of $|f'_x f''_y - f''_x f'_y|^2$. There may be cases in which both interferences are observable while a weak peak is not, but for the majority of experiments reconstruction of a weak scatter from interferences does not appear to be a viable option. Thus, the current bottom-line limitation for MOIDS is that the experimental noise ,must be less than the peak to be extracted.

3.10 Summary

There are some key features to remember when employing MOIDS:

(A) In using MOIDS multiple layers of material X are treated completely analogously to a single layer of X since they both contain exactly the same scattering factors. This means that any distribution of material X, whether continuous or not, requires exactly the same number of independent energy scans to solve, and this is precisely what is meant when the method is said to be parameter-fitting free.

(B) No *a priori* knowledge about the shape or distributions of a given material is needed, just that it exists and how its scattering factors vary with energy. The upshot is that core-shell nanoparticles, for example, would be just as good candidates for the MOIDS technique as layered films. Conversely, an average diffraction profile is reconstructed for each material, and is not easily broken down into multiple distinct scattering regions even if they are spatially separated.

(C) The number of energy-varying diffraction scans (accompanied by significant change in one or more atomic scattering factors) dictates the number of scattering regions that may be solved for.

(D) If coherent interference between two regions is expected additional terms can be readily added to account for this.

(E) If enough terms plus an equal number of diffraction patterns are included to cover every material and interference, then a unique solution is ensured.

(F) The method is not based on isolating the change from a single scattering element so it's perfectly acceptable (even advantageous) to choose a wider range of energies over which many scattering atoms may experience significant cross-section changes. By choosing appropriate energies over a wider range this can allow relaxation of knowing exactly where one sits about a sharply changing absorption edge of potentially unknown shape.

(G) Each point in reciprocal space provides a self-consistent independent result, and the smoothness of the scattering profiles over a range on reciprocal space can be used to gauge the quality of the fits.

(H) Absolute beam normalization is not required. However, it is imperative to obtain a relative measure of incident intensity independent of energy in order to take full advantage of this quantitative method.

(I) Background noise and statistical fluctuation of a reasonable level expected under normal experimental conditions do not typically prevent reconstruction. In extracting very small signals from weakly scattering regions, however, this noise needs to be reduced such that it is lower than the diffraction to be measured.

Chapter 4

Ultra-Thin Film Structure and Strain

As discussed in section 1.4 both an elevated orbital to spin moment ratio and increased Gilbert damping with decreased sample thickness were observed on ultra-thin Cu|Co|Cu spin-transfer samples using ferromagnetic resonance [22]. In order to explain these results from a structural standpoint, and to check on the assumption that thinning of the Co layers did not affect their intrinsic atomic structure, needed for properly extracting the extrinsic Gilbert damping, a thin film application of anomalous diffraction was developed in chapter 3. By careful fitting of both the Co scattering contribution and a non-negligible Cu-Co interference, extraction of the buried, ultra-thin Co Bragg peaks was achieved. A check on the accuracy of the method involves comparing the full width half maximum of the extracted peaks with thickness-determined Debye broadening. If interference is overly dominant, the extracted pure peaks would appear overly sharp.

4.1 Non-resonant description

The nonmagnetic Cu spacers were chosen both for their long spin diffusion lengths of 250 nm, and for their structural similarly to Co in the face centered cubic form. The Pt caps were added for their tendency to act as perfect spin sinks. Two Pt caps show heightened damping compared with just one, but no additional yield were observed beyond Pt thicknesses of 15 $\mathring{A}$ [22].

The series of samples studied in this work consist of sputter-deposited films of 15 or 50 $\mathring{A}$ Pt|100 $\mathring{A}$ Cu|15, 30, or 60 $\mathring{A}$ Co|100 $\mathring{A}$ Cu|50 $\mathring{A}$ Pt grown on top of a [100] GaAs wafer. The samples were grown in 10^{-8} Torr vacuum. The nominal thicknesses listed above were determined by the NYU Kent group sample providers using calibrated piezoelectric thickness monitors. Specular reflectivity performed at 7.5 keV at beam line X16C (on the 15 $\mathring{A}$ Pt capped samples) and 9.66 keV at beam line X6B (on the 50 $\mathring{A}$ Pt capped samples), assuming nominal lattice face centered cubic lattices of 3.9239, 3.6147, and 3.5440 $\mathring{A}$ for the Pt, Cu, and Co, respectively, indicate that the Pt and Cu thickness vary little from sample to sample. The Cu layers, however, are slightly thinner, on average ≈ 81 $\mathring{A}$, than anticipated. The results of the specular reflectivity fitting are given below in Table 4.1 with an uncertainty of $\pm$ 5 $\mathring{A}$,

Table 4.1: Specular Reflectivity Fit Results

sample	nominal thicknesses ($\mathring{A}$)	measured thicknesses (± 5 $\mathring{A}$)
	Pt (top), Co	Pt (top), Cu, **Co**, Cu, Pt (bottom)
S1	50, 15	47, 84, **11**, 78, 45
S2	15, 15	11, 83, **23**, 81, 40
S3	50, 30	50, 89, **35**, 89, 41
S4	50, 60	57, 70, **65**, 76, 59
S5	15, 60	9, 72, **65**, 83, 42

while the final models and experimental data are shown in Figure 4.1. All specular fitting within this thesis utilizes the program Parratt32 [55] for fitting of the dynamic scattering profiles. Henke scattering factors are sufficiently good to be used directly, especially away from any resonances where the specular reflectivity measurements were conducted.

Non-resonant diffraction taken at 19 keV on beamline X6B indicates that the films are textured such that the [111] Pt and Cu face centered cubic lattice orientation is preferentially aligned along the sample normal. All samples behave similarly, and a representative scans taken on S4 are displayed in Figure 4.2. This texturing explains the peak intensity changes seen as a function of angle, χ, formed by the sample normal and $\hat{k}$. Note how the brightest diffraction spots, [111] and [200], become more pronounced at χ's of 0^o and 55^o, respectively, which can be explained by the unstrained, [111] textured, face centered cubic model given in Figure 4.3. Although preferentially oriented, these films are still polycrystalline in the sense that they scatter isotropically within the sample plane as evidenced by the CCD image, shown in Figure 4.4. The brightness appears heightened along the central vertical direction, but this is an effect of background scattering. Rotation of the sample about ϕ shows no observable changes in intensity.

With conventional diffraction, as employed thus far, the general Pt and Cu atomic arrangements are obvious. The structure of the Co, however, is not clear as its signal is overwhelmed by Cu of similar lattice spacing. What is observable from Figure 4.5 is that there exists some Co reflection containing a lattice spacing between 2.046 and 2.087 $\mathring{A}$ along the sample normal. This is evidenced from the combined Cu-Co peak shift from the nominal face centered cubic Cu spacing toward nominal face centered cubic Co spacing with increasing Co thickness.

Co is capable of assuming different structural forms at room temperature including hexagonal close pack with lattice constants $a = b =$2.507 $\mathring{A}$; $c =$4.069 $\mathring{A}$, face centered cubic of 3.544 $\mathring{A}$, and even the less common body centered cubic of 2.82 $\mathring{A}$ [65]. Assuming a powder sample (to allow for all possible orientations) and retaining only reflections of 1.25 $\mathring{A}$ spacing or more, the possible signature peaks are presented in Table 4.2. Without additional information [111] face centered cubic, distorted [002] hexagonal close pack, or very strained [110] body centered cubic reflections could all potentially account for the observed Co contribution to the Cu/Co out-of-plane peak.

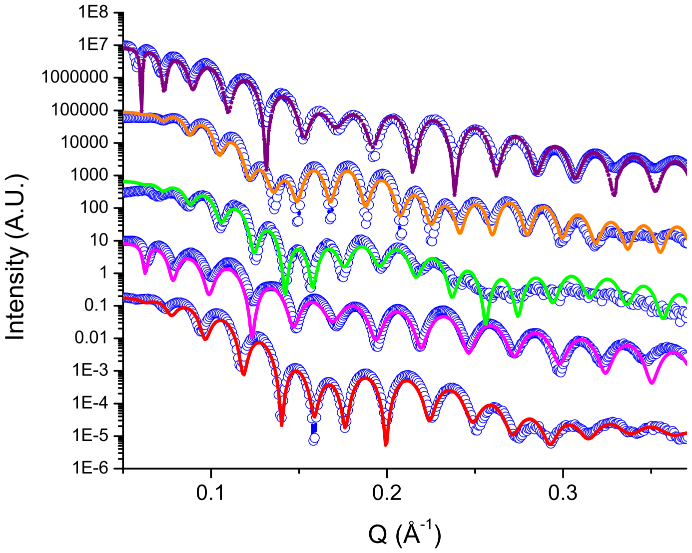

Figure 4.1: All data is shown in blue, while the corresponding fits are shown in purple (S5), orange (S4), green (S3), pink (S2), and red (S1). Intensity shifts are arbitrarily used to separate data for clarity.

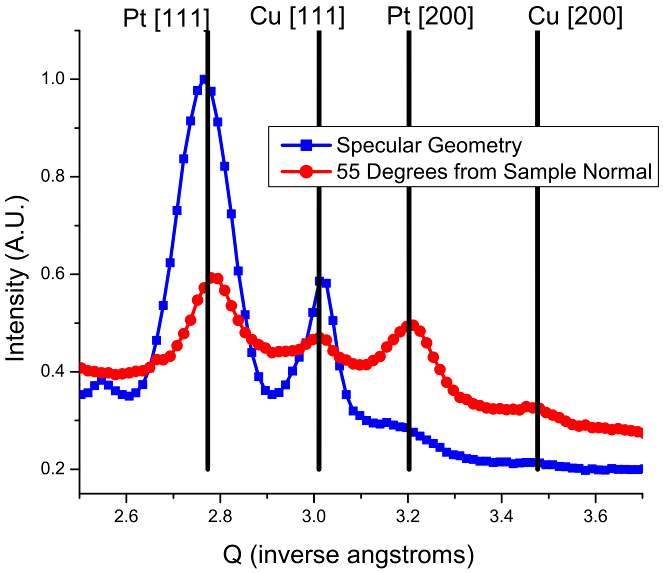

Figure 4.2: Texture of Pt and Cu/Co Face-Centered Cubic Structures

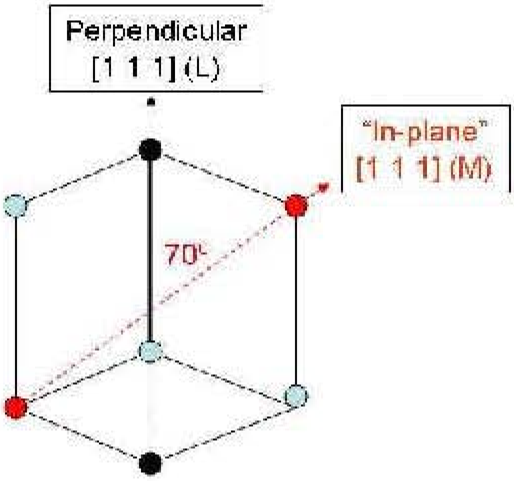

Figure 4.3: Model of Unstrained [111] Textured Face-Centered Cubic Structure

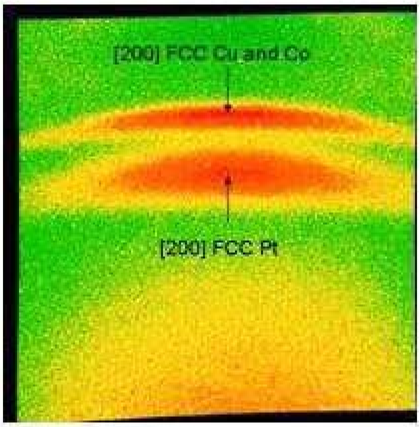

Figure 4.4: CCD Imaging of In-Plane Homogeneity within Textured, Polycrystalline Pt, Cu, Co layers. Rotation about ϕ shows no change in intensity and indicates the samples are homogeneous within the sample plane.

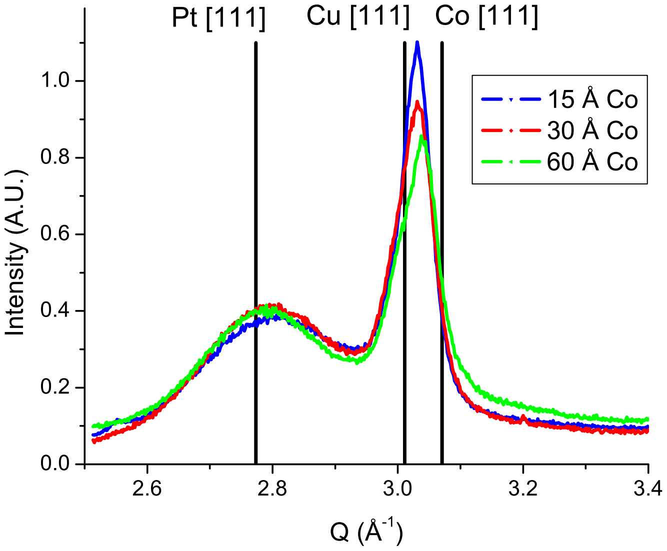

Figure 4.5: Peak Shift of Cu/Co Oriented Along Sample Normal with Co Thickness

Therefore, the tasks at hand are to locate a second, non-collinear Co reflection as a function of χ by which to determine the basic Co lattice structure, and to measure the in and out-of-plane strain changes (if any) as a function of Co thickness. To proceed further the element specificity of anomalous scattering is required.

4.2 Cobalt Thickness Changes

As demonstrated in chapter 3 the difference in anomalous diffraction intensity on and before the Co K-edge can be fit by two Gaussians representing the Cu-Co interference and the pure Co scattering, as long as the interference isn't overly influential. Evidence for this comes in the form of an extracted Co peak with the correct Debye broadening width. Figure 4.6 displays the individual Gaussian fits, and the resulting FWHM fits are reasonable for the Co layer thicknesses. Like the fit of 65 $\AA$ Co, the 35 $\AA$ has a FWHM of 0.15 $\AA^{-1}$ which is quite close to the Debye thickness limited width of 0.13 $\AA^{-1}$. The thinnest sample of 12 $\AA$ Co, however, has an experimental width of only 0.29 $\AA^{-1}$, but a predicted width of 0.385 $\AA^{-1}$. This could be due to an uncertainty in measured thickness from specular reflectivity fitting of ± 0.5 $\AA$ combined with sharply changing widths as a function thickness at ultra-thin sizes, or the Gaussian fit may not be quite correct due to Co-Cu interference dips that could potentially shorten the apparent width. At this ultra-thin level it is very hard to separate the two as specular reflectivity thickness measurements are simply not all that precise. Sample S2 of 23 $\AA$ Co, (fit shown in chapter 3) made in a different sample

Table 4.2: Possible Co Reflections of 1.25 $\mathring{A}$ or Wider Spacing

crystal	reflection	relative intensity (%)	spacing $\mathring{A}$
FCC	[111]	100	2.0461
FCC	[200]	50	1.7720
FCC	[220]	34	1.2530
HCP	[102]	24	2.1711
HCP	[002]	26	2.0345
HCP	[101]	100	1.9155
HCP	[102]	16	1.4846
HCP	[110]	18	1.2535
BCC	[110]	100	1.994
BCC	[200]	18	1.410

Table 4.3: Cobalt Sample-Normal Strain from Anomalous Diffraction

Sample	Interference ($\mathring{A}^{-1}$)	Co Peak ($\mathring{A}^{-1}$)	Co FWHM ($\mathring{A}^{-1}$)	Expected FWHM ($\mathring{A}^{-1}$)
S4 (65 $\mathring{A}$)	3.03422 ± 0.00096	3.08977 ± 0.00781	0.07439 ± 0.01094	0.070
S3 (35 $\mathring{A}$)	3.03954 ± 0.00057	3.09044 ± 0.00824	0.15122 ± 0.01143	0.13
S1 (12 $\mathring{A}$)	3.02227 ± 0.00094	3.09366 ± 0.01181	0.28928 ± 0.02775	0.38(5)
Average	3.032	3.091		

batch, has not been included in the averaged values because its Cu-Co interference peak appears to dominate to such an extent that anomalous subtraction is no longer as reliable in extracting the comparatively smaller Co signature. The reduced pure Co scattering here may be attributable to a roughened sample, having seen more beam and spent more time in atmosphere than the other three Co samples examined. Its Co extraction and best Gaussian fits are still, however, within the uncertainty consistent with the other samples. The lattice values determined from the Co fits of the samples are surprisingly constant and point to an average lattice spacing of 2.033 ± 0.01 $\mathring{A}$ with an average compressive strain of 0.64 %. Within uncertainty of measurement, no strain changes are detected as a function of Co thicknesses of 12 to 65 $\mathring{A}$, and therefore the single in-plane lattice measurement taken on S4 should be representative of all thicknesses within the range examined. The numerical results of these sample-normal [111] lattice measurements are summarized in Table 4.3.

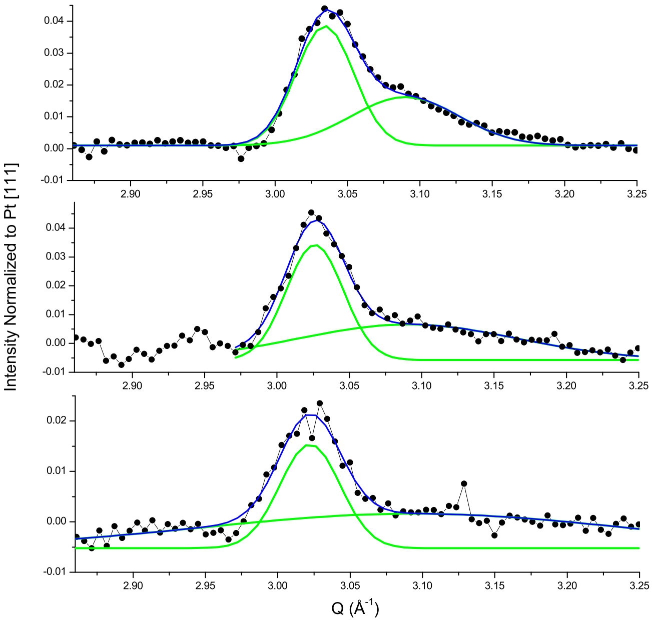

Figure 4.6: Extracted Co-Based Peaks as a Function of Thickness. (Top) 65 $\AA$ Co, (middle) 35 $\AA$ Co, and (bottom) 12 $\AA$ Co.

Table 4.4: [111] Co Spacing Along Sample Normal as a Function of Thickness

Sample	[111] Spacing $\AA$
65 $\AA$ Co	2.031 ± 0.016
35 $\AA$ Co	2.033 ± 0.011
12 $\AA$ Co	2.034 ± 0.011
Average	2.033

4.3 Decreased Interference Within the Sample Plane

Figure 4.3 depicts an unstrained face centered cubic lattice with one of its three [111] orientations aligned along the z-direction. Although Pt and Cu have both been determined to be textured face centered cubic cubic, a second peak of decidedly Co contribution must be located in order to verify if Co is also textured face centered cubic. The next brightest unstrained face centered cubic reflections are a [200] at 55° from the sample normal and a second [111] at 70° from the sample normal. Although the sample may in fact be tetragonally distorted, small changes in bond angles shouldn't make much difference for diffraction purposes given the polycrystalline nature of the sample. In-plane homogeneity causes both reflections to scatter into rings so the main concern with regard to sample rotation is to avoid substrate Bragg tails which can extend over large areas in reciprocal space. Experimentally, the in-plane [111] peak appeared brighter than the [200] so the sample was tilted such that the $\vec{k}$ would probe at 70° from the sample normal, from here on referred to as the "in-plane" [111] orientation.

Figure 4.7 shows both the perpendicular and in-plane [111] features of S2 taken at an off-resonance energy of 8.344 keV. The beam normalized in-plane peaks were universally lower in intensity as expected from homogeneous, in-plane, ring-like scattering, but with the Pt peaks normalized to unity a noticeable relative decrease in the Cu-Co peaks is observed. This might be attributable to a lower Cu-Co interference which now probes over many more crystallites (a factor of $\cos(70^{\circ})^{-1} \approx 3$ times larger) resulting in a relatively lower interface contribution. Additionally, since the sample was grown along the z-direction in-plane crystallites are likely to have less neighbor-to-neighbor coherence than along the sample normal, resulting in additional Cu-Co in-plane interference loss. The in-plane Cu-Co peaks also show a shift toward lower Q (larger spacing), while the Pt does not show any lattice spacing changes.

As discussed previously, S2 has a limited number of diffraction energies to use as inputs. Incorporating the same three diffraction based energies into MOIDS shows a distinctive shift between the extracted Cu and Co peaks, Figure 4.8. The Co-based peak, although noisy, is substantially wider than the out-of-plane counterpart, Figure 3.19. These are strong indications of reduced in-plane Cu-Co interference compared with that in the out-of-plane case.

Moving on to a thicker Co sample, S5, in-plane anomalous subtraction in Figure 4.9 shows a Co-based Gaussian with a FWHM corresponding to crystallites of approximately 50 $\mathring{A}$. A small, but sharp secondary peak might be attributable to Cu-Co interference, but it is a very minor contribution. The in-plane Co peak is clearly shifted to a wider lattice spacing than it has along the sample normal which stems from approximate volume conservation. As the lattice in expanded in-plane by the wider Cu template, the out-of-plane Co lattice responds by compressing slightly.

For the 65 $\mathring{A}$ sample (S4) the extracted out-of-plane Co peak was centered at a spacing of 2.031 $\mathring{A}$, and for 65 $\mathring{A}$ sample (S5) the extracted in-plane Co peak was found to have a spacing of 2.074 $\mathring{A}$. Together the two Co [111] lattice spacings confirm that the Co forms a tetragonally strained face centered cubic crystal. Body centered

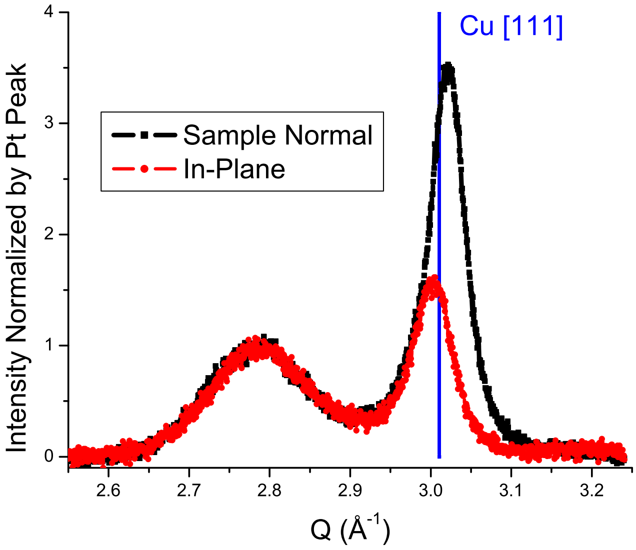

Figure 4.7: Shift in [111] Face centered cubic Cu-Co Peak at χ of 0 and 70^o

cubic and hexagonal close packed crystal structures can now be excluded as volume conservation would be badly violated in both cases. The argument that a single peak diffracting in a powder-like manner could be responsible for these observed Co peaks does not hold when isotropic strain is observable.

4.4 Copper Structure

The extracted Cu-based profiles of Figure 4.10 all display a double peak feature to various degrees. As demonstrated in section 3.2 this could be accounted for by Pt-Cu (left hand side) and Cu-Co (right hand side) interferences. It is interesting to note that some degree of pre-Cu peak oscillations still remain even after subtraction about the Cu K-edge, but not about the Co K-edge, indicating a Cu or Cu-Pt origin. Although it is tempting to place the Cu peak center at the average maximum (3.025 $\mathring{A}^{-1}$) with a corresponding lattice spacing of 2.077 $\mathring{A}$, this may not be entirely valid due primarily to the presence Cu-Co interference (Pt-Cu interference would only shift the apparent peak in the other direction). In both the Co-based and Cu-based extractions there appears to be a combined Cu-Co peak of constant spacing, except for the 65 $\mathring{A}$ case where the net peak shifts slightly toward bulk face centered cubic Co value. As all three right hand side peaks for the 12, 23, and 35 $\mathring{A}$ Co samples do not shift as a function of Co thickness they may have already reached their limiting values which coincide with the Cu peak for vanishing amounts of Co. Additionally, the sharp peak portion is in fact best fit with two Gaussians of nearly

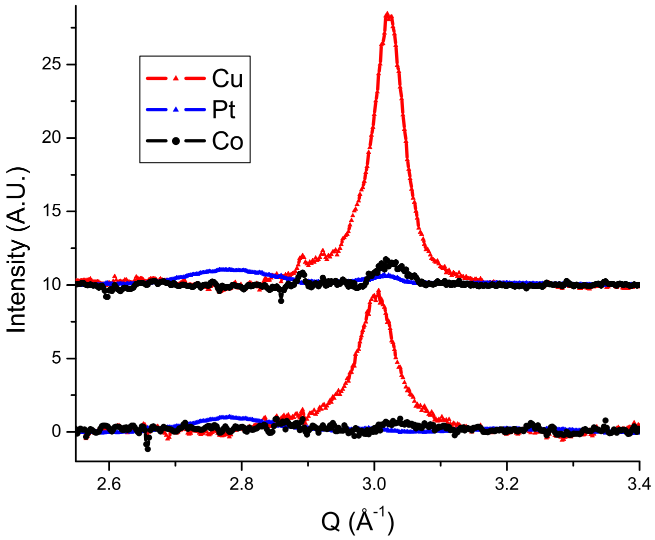

Figure 4.8: Comparison of In and Out-of-Plane Three Energy MOIDS Reconstruction of Sample S2.

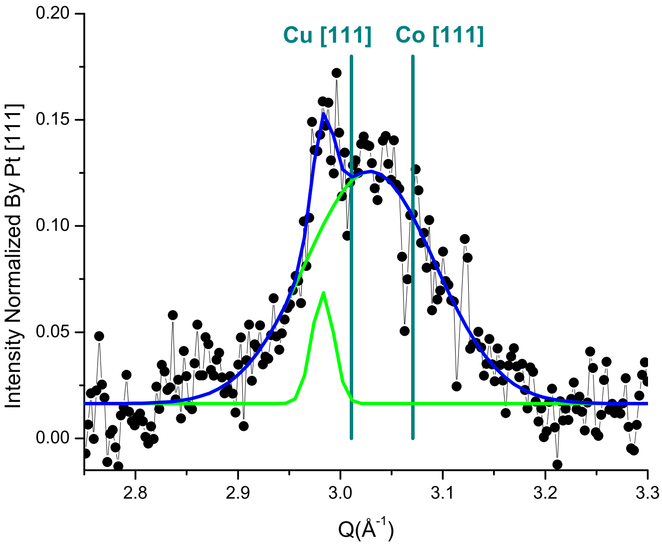

Figure 4.9: Extracted Co in-plane [111] face centered cubic lattice.

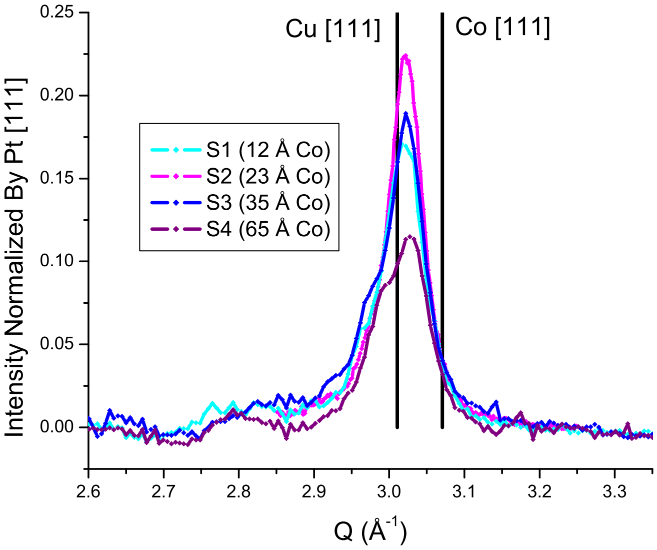

Figure 4.10: Extracted Cu out-of-plane [111] face centered cubic lattice and interference

the same lattice spacing, but different widths, especially true for the thinnest sample, S1. Therefore, the out-of-plane Cu spacing is tentatively pegged at a constant lattice of about 2.077 $\AA$, overlapping with the Cu-Co interference peak, with an approximate compressive strain of -0.5 percent. Again, applying the a more sophisticated analysis such as MOIDS if more energy-dependent scans were available would remove the need interpretive fitting and its associated uncertainty.

Like the in-plane Co, the in-plane Cu appears almost single peaked with a [111] lattice spacing 2.092 $\AA$, Figure 4.11. Based on the extracted FWHM values the Co and Cu appear to form ”in-plane” crystallite widths of roughly 50 and 100 $\AA$, respectively.

4.5 Strained Model

Table 4.5 summarizes the Co and Cu [111] lattice measurements along the in- and out-of-plane orientations, but displays them as *three* times the [111] real-space lengths, denoted from here on as L and M, respectively. (The reason for including the factor of three is that this describes the distance between opposite corner atoms within the strained face centered cubic lattice, rather than the nearest-plane spacing measured by diffraction.) With L and M values in hand plus the assumption of in-plane homogeneous strain (supported by CCD imaging as shown in Figure 4.4) all the remaining positions of atoms can be assigned within the unit cell.

An unstrained face centered cubic crystal oriented with [111] along the z-axis has

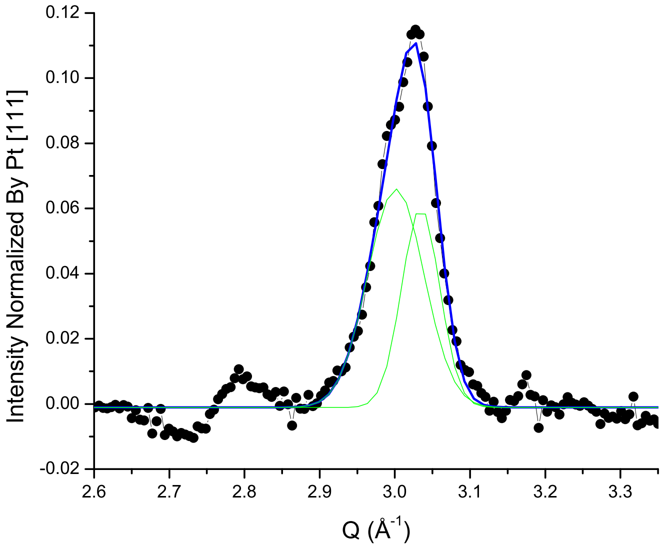

Figure 4.11: Extracted Cu in-plane [111] face centered cubic lattice and interference

Table 4.5: Cumulative Anomalous Diffraction Results

Layer	L ($\mathring{A}$)	M ($\mathring{A}$	Percent Volume Change
Cobalt	6.099 ±0.03	6.222 ±0.03	+2.6
Copper	6.231 ±0.03	6.275 ±0.03	-0.15

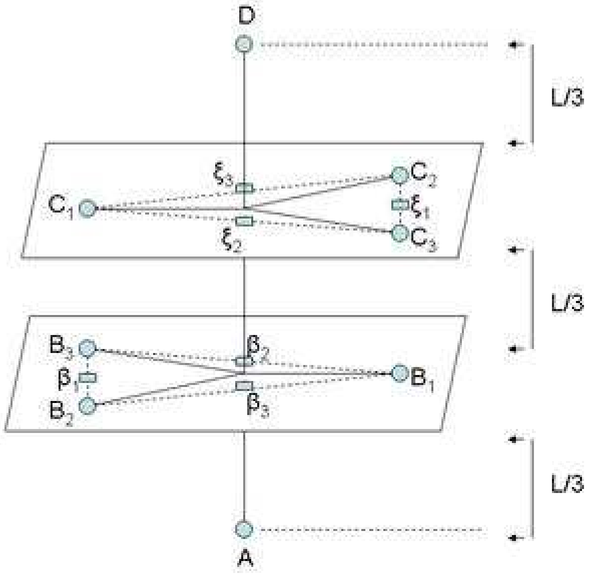

Figure 4.12: Strained Lattice Model

four distinct xy-planes containing all constituent atoms at z positions of 0, L/3, 2L/3, and L. Homogenous in-plane strain dictates that although the magnitude of L may change, the z-positions of these four planes in terms of L won't. The strained crystal can now be redrawn where A, B's, C's, and D are corner atoms, and β's and ξ's refer to those atoms centered within a lattice face. In an unstrained, crystal atoms B_1, B_2, B_3, β_1 ,β_2, and β_3 take up positions at 60^o from each other about the z-axis. The same holds for the C_1, C_2, C_3, ξ_1, ξ_2, and ξ_3 with a universal 180^o rotation about the z-axis between corresponding B and C pairs. By the same argument of homogeneous in-plane strain these angles are invariant. Vectors locating all lattice atoms with respect to atom A within one unit cell oriented along the z-axis, corresponding to Figure 4.12, is provided in Table 4.6. All remaining near-neighbor atoms residing in adjacent lattices oriented within the x-y plane and along the negative z-axis can be expressed similarly by combinations of L and M (79 atoms total within single unit cell distance). This provides the basis for calculating multi-atom scattering path lengths (as required in the next section for EXAFS analysis).

Approximate volume conservation predicts that the strained Co and Cu lattice volumes should not vary substantially from their bulk values of $(3.544\AA)^3$ and $(3.6147\AA)^3$, respectively. In our strained model the volume, V, is given by equations 4.1 and 4.2. The copper volumes are consistent, but the strained cobalt appears to exhibit a 2.6 percent volume expansion. Since in-plane Co extraction shows much less Cu-Co interference than along the sample normal it is better candidate for limited energy MOIDS and anomalous subtraction. Although the out-of-plane Co lattice spacing are consistent and in general have the expected FWHMs for the contributing Co thickness, they

Table 4.6: Atomic Positions in Terms of L and M

Atom	X	Y	Z	Bond Length from A
β_1	$-\sqrt{(M^2-L^2/9)}/4$	0	L/3	$\sqrt{(9M^2+15L^2)}/12$
β_2	$\sqrt{(M^2-L^2/9)}/8$	$\sqrt{(3M^2-L^2/3)}/8$	L/3	$\sqrt{(9M^2+15L^2)}/12$
β_3	$\sqrt{(M^2-L^2/9)}/8$	$-\sqrt{(3M^2-L^2/3)}/8$	L/3	$\sqrt{(9M^2+15L^2)}/12$
B_1	$\sqrt{(M^2-L^2/9)}/2$	0	L/3	$\sqrt{(M^2+L^2/3)}/2$
B_2	$-\sqrt{(M^2-L^2/9)}/4$	$-\sqrt{(3M^2-L^2/3)}/4$	L/3	$\sqrt{(M^2+L^2/3)}/2$
B_3	$-\sqrt{(M^2-L^2/9)}/4$	$\sqrt{(3M^2-L^2/3)}/4$	L/3	$\sqrt{(M^2+L^2/3)}/2$
ξ_1	$\sqrt{(M^2-L^2/9)}/4$	0	2L/3	$\sqrt{(M^2+7L^2)}/4$
ξ_2	$-\sqrt{(M^2-L^2/9)}/8$	$-\sqrt{(3M^2-L^2/3)}/8$	2L/3	$\sqrt{(M^2+7L^2)}/4$
ξ_3	$-\sqrt{(M^2-L^2/9)}/8$	$\sqrt{(3M^2-L^2/3)}/8$	2L/3	$\sqrt{(M^2+7L^2)}/4$
C_1	$-\sqrt{(M^2-L^2/9)}/2$	0	2L/3	$\sqrt{(M^2+5L^2/3)}/2$
C_2	$\sqrt{(M^2-L^2/9)}/4$	$\sqrt{(3M^2-L^2/3)}/4$	2L/3	$\sqrt{(M^2+5L^2/3)}/2$
C_3	$\sqrt{(M^2-L^2/9)}/4$	$-\sqrt{(3M^2-L^2/3)}/4$	2L/3	$\sqrt{(M^2+5L^2/3)}/2$
D	0	0	L	L

are probably slightly less reliable due to the usual limitations of properly accounting for Cu-Co interference without a full-energy MOIDS diffraction set.

$$V = \frac{1}{2} * \overline{AB_1} * \overline{AC_1} * \overline{C_1C_2} \tag{4.1}$$

$$V = \frac{1}{16} * \sqrt{(M^2+L^2/3)} * \sqrt{(M^2+5L^2/3)} * \sqrt{(M^2-L^2/3)} \tag{4.2}$$

4.6 EXAFS Comparison

An alternative anomalous method, EXAFS, though not as model independent as diffraction, can be used to extract crystalline structure. Here we shall explore how it performs on thin films S2 and S5, both as a check on the current work and as a means to see how it compared with anomalous diffraction. Fluorescence-yield absorption data was collected in nearly grazing incidence to achieve maximum signal from such the ultra-thin Co layers. The collection times were set to collect more than 350,000 and 150,000 counts per point up to 8.2 keV for samples S5 and S2, respectively, the results of which are given in Figures 4.13. The oscillations of interest are on the order of 1/20 the total absorption which yields uncertainties of ≈ 3 and 5%, respectively. Absorption taken in the same geometry on the Cu K-edge of S2 and at 45^o reflection for a Cu foil did not produce the same rounding-slope features after the absorption edge indicating the effect is primarily an artifact of the ultra-thin films. Athena was used to fit the location of the edge jump, the overall background shape, μ_o, and transform the remaining oscillations into interchangeable functions of k (equivalent

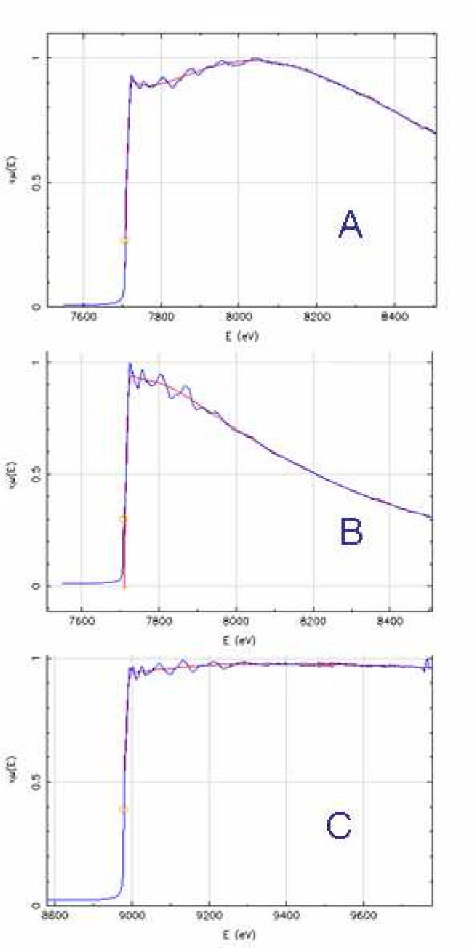

Figure 4.13: Normalized absorption used in EXAFS analysis. (A) 23 $\mathring{A}$ Co, (B) 65 $\mathring{A}$ Co, and (C) 80 $\mathring{A}$ Cu

to Q) and effective path lengths, R_{eff}, after element-dependent phase shifts had been accounted for. These fits are displayed in red in Figure 4.13.

Using the strained, [111] textured, face centered cubic model of the previous section as input, FEFF6 was used to compute all 70 potential scattering paths (of up to 4 legs) from the 79 nearest neighbor atoms present within a 6 $\mathring{A}$ effective distance. Corresponding amplitudes and phase shifts were calculated by assuming in both the Co and Cu models that all scattering atoms are identical to the original absorbing source atom. This is a good approximation as even in the thinnest layer, the 23 $\mathring{A}$ Co of S2, the ratio of interior to interface scattering is better than 10:1. All non-zero paths were used in the Co models, and the most intense 16 paths in the Cu models with importance dictated by their calculated amplitudes.

It is has been stated in literature that linearly-polarized EXAFS taken with $\hat{\epsilon}$ oriented along and perpendicular to the sample surface preferentially probes the in and

Table 4.7: Scattering Pathlengths in Terms of L and M

Example	Multiplicity	Amplitude	Pathlength
$A \rightarrow \beta_3 \rightarrow A$	6	100 %	$\sqrt{(3M^2 + 5L^2)/48}$
$\beta_3 \rightarrow B_2 \rightarrow \beta_3$	6	97 %	$\sqrt{(9M^2 - L^2)/48}$
$D \rightarrow C_3 \rightarrow D$	6	45 %	$\sqrt{(3M^2 + L^2)/12}$
$A \rightarrow \xi_2 \rightarrow A$	6	28 %	$\sqrt{(M^2 + 7L^2)/16}$
$\xi_2 \rightarrow B_2 \rightarrow \xi_2$	12	54 %	$\sqrt{(7M^2 + L^2)/16}$
$\beta_3 \rightarrow B_3 \rightarrow \beta_3$	6	27 %	$\sqrt{(9M^2 - L^2)/16}$
$D \rightarrow B_2 \rightarrow D$	6	19 %	$\sqrt{(3M^2 + 5L^2)/12}$
$A \rightarrow C_1 \rightarrow B_2 \rightarrow A$	12	51 %	$\sqrt{(3M^2 + 5L^2)/12}$
$A \rightarrow \beta_1 \rightarrow A \rightarrow -\beta_1 \rightarrow A$	6	10 %	$\sqrt{(3M^2 + 5L^2)/12}$
$A \rightarrow \beta_1 \rightarrow C_1 \rightarrow \beta_1 \rightarrow A$	6	41 %	$\sqrt{(3M^2 + 5L^2)/12}$
$C_1 \rightarrow C_3 \rightarrow C_1$	6	18 %	$\sqrt{(9M^2 - L^2)/12}$
$B_1 \rightarrow -2 * B_1 \rightarrow \beta_1 \rightarrow B_1$	12	48 %	$\sqrt{(9M^2 - L^2)/12}$
$\beta_1 \rightarrow B_2 \rightarrow \beta_1 \rightarrow B_3 \rightarrow \beta_1$	12	10 %	$\sqrt{(9M^2 - L^2)/12}$
$C_1 \rightarrow \xi_3 \rightarrow C_2 \rightarrow \xi_3 \rightarrow C_1$	6	39 %	$\sqrt{(9M^2 - L^2)/12}$
$A \rightarrow B_2 + \beta_3 \rightarrow A$	12	28 %	$\sqrt{(21M^2 + 19L^2)/48}$
$A \rightarrow \beta_2 - 2 * B_1 \rightarrow A$	12	27 %	$\sqrt{(39M^2 + L^2)/48}$

out-of-plane directions, respectively. While this is a true statement as the probability of scattering goes as the $\cos(\Upsilon)^2$, where Υ is the angle made by the beam polarization and the scattering vector, the idea can be overly exaggerated. As demonstration the top L and M determined path lengths probed with an in-plane $\hat{\epsilon}$ x-ray source are presented in Table 4.7 along with their calculated multiplicities and amplitudes which govern their relative importance. From this it becomes obvious that "in-plane" EXAFS, even with L completely aligned along the z-axis, is heavily dependent on both variables. (Any deviation from the textured model would only reduce the relative contribution differences.) It is interesting to note that if L and M were the same in several instances two distinct paths would combine into one. This explains why the first-shell experimental Co EXAFS peaks from S2 and S5 (which will be presented shortly) are less sharp than predicted from unstrained face centered cubic models, and reaffirms the non-equivalence of L and M.

The textured model should include in-plane homogeneity, but FEFF6 only accepts one crystalline structure with a single orientation at a time. The solution is to make $\hat{\epsilon}$ (in the model) circularly polarized within the xy-plane which was done for the above calculations. In cases where a powder model (all crystal orientations of equal probability) are desired the trick is to simulate with an unpolarized $\hat{\epsilon}$. The powder models have L and M based path lengths identical to those in Table 4.7, but the relative amplitudes vary.

Artemis is used to find the best match between model and experimental results by varying user-specified fitting parameters. Beam line X6B, NSLS at which the

Table 4.8: EXAFS Results

Sample	Edge	Model	L (Å)	M (Å)
S5	Co	**Powder**	**5.9625 ± 0.0550**	**6.1901 ± 0.0299**
		Texture	—	—
S2	Co	Powder	5.9914 ± 0.0783	6.2128 ± 0.0349
		Texture	5.9384 ± 0.1141	6.1642 ± 0.0175
		Pow-Tex Ave	**5.9649 ± 0.0265**	**6.1885 ± 0.0243**
Foil	Cu	**Powder (L=M)**	**6.2591 ± 0.0153**	—
		Powder	6.1272 ± 0.0583	6.3096 ± 0.0252
		Texture	6.1552 ± 0.1618	6.2686 ± 0.0203
S2	Cu	Powder (L=M)	6.2657 ± 0.0214	—
		Powder	6.0571 ± 0.0325	6.3716 ± 0.0220
		Powder (1-3 Å)	**6.2162 ± 0.9649**	**6.2698 ± 0.4541**
		Texture	6.1380 ± 0.2728	6.2794 ± 0.0304

EXAFS data was acquired typically varies by less that a few eV within a several keV range, thus, only one universal energy shift was allowed to account for monochromator miscalibration and any misalignment in the assignment of the transition edge jump. The relative amplitudes as calculated were preserved, but more distance path lengths were allowed to subside in four distance-defined regions as a function of roughness, σ^2. Finally, all the effective path lengths were recast in terms of L and M, and these were allowed to vary from their diffraction-based values. Although the EXAFS fit could have been further constrained by requiring the volume of the strained lattice to be equal to the corresponding unstrained volume, this author feels it was preferable to let L and M vary independently and then use the resulting volume change as a check on the reliability of the fit.

The best-fit parameters are given in Table 4.8 for both fully textured and the powder-like models, while the overall best fits (bold in Table) are displayed in Figures 4.14 (Co-edge) and 4.15 (Cu-edge). The 65 Å Co sample was only well modeled by the powder set-up, with the resulting L and M lattices slightly reduced from those measured by diffraction. However, the EXAFS powder model reproduces the expected unstrained face centered cubic volume within 0.2 percent. The 23 Å Co could be fit almost equally well by the texture or powder models, the values of which average out to that of the 65 Å case. Neither full powder nor texture models reproduce the expected volume conservation, but an average of the two does. Thus, a hybrid seems the to be the best description with L and M lengths. Within experimental uncertainty both **EXAFS and diffraction do not reveal any change in strain as a function of Co thickness**. A pure Cu foil, used as a check, was best fit with a powder face centered cubic model with an L-M value consistent with unstrained Cu, as expected, although it did produce differing L and M values in the constrains of a texture model which makes the differing L and M values found in the other samples somewhat less credible. The Cu within S2 could only be reasonably matched using a limited R_{eff} range of 1-3 $\AA$. With a powder model, though, its L and M values were found to match those obtained by anomalous diffraction.

Additionally, a fully textured hexagonal close pack Co model with the c-axis oriented along the z-axis has been examined for comparison on sample S2. As in the face centered cubic models the same parameters were allowed to vary, except the lattice parameters were given as functions of the typical a- and c-axes of a hexagonal close pack lattice, preserving the usual bond angles. This model, however, did not fit the data well and was discarded. A body centered cubic model, being both a fairly exotic form of Co and having a very different EXAFS profile from either face centered cubic or hexagonal close pack, was not considered further. Although EXAFS modeling was not found to be overly sensitive to texture in the polycrystalline films, like the diffraction it effectively excluded the hexagonal close pack and body centered cubic forms of Co.

4.7 Summary

The structure of ultra-thin (12 - 65 $\AA$), buried layers of sputter deposited Co within a [111] textured face centered Cu sandwich was successfully determined to be a trigonally strained form of face centered cubic. In and out-of-plane [111] lattice parameters were determined to be 2.074 ± 0.01 $\AA$ and 2.033 ± 0.01 $\AA$, respectively. The key was that interlayer interference, even in polycrystalline films, had to be taken in to consideration during the fitting process.

As determined by experiment both anomalous diffraction subtraction and EXAFS provided complementary information. Diffraction provides unique information about the coherence between layers, while EXAFS is experimentally easier to perform. For the Cu samples EXAFS and diffraction agree well on the lattice spacing of a semi-textured sample, but EXAFS alone could not distinguish between powder and texture forms. EXAFS lattice values for the Co layers, however, more closely reproduce the unstrained cubic volume than diffraction does. The in-plane lattice expansion between the two experiments agree within uncertainty, but the out-of-plane measurements are less sensitive in the EXAFS model. Both methods agree that the Co structure did not change with thickness within ± 0.01 $\AA$. This in turn means that varying the thickness of Co layers in order to access Gilbert damping and surface:bulk changes is indeed valid for these samples.

Since the the structure did not change within uncertainty limits this implies the observed increase in Lande g-values with decreasing thickness appears to be related to an increased interface. If one assumes that total Co spin moments do not substantially change in the presence of a Co-Cu interface, this implies an enhancement in orbital moment for all thicknesses studied. This correlates well with the fact that all thicknesses examined structurally were found to be significantly trigonally strained. Therefore, the baseline enhancement of the Lande g-factor is attributed to strain-induced trigonal distortion.

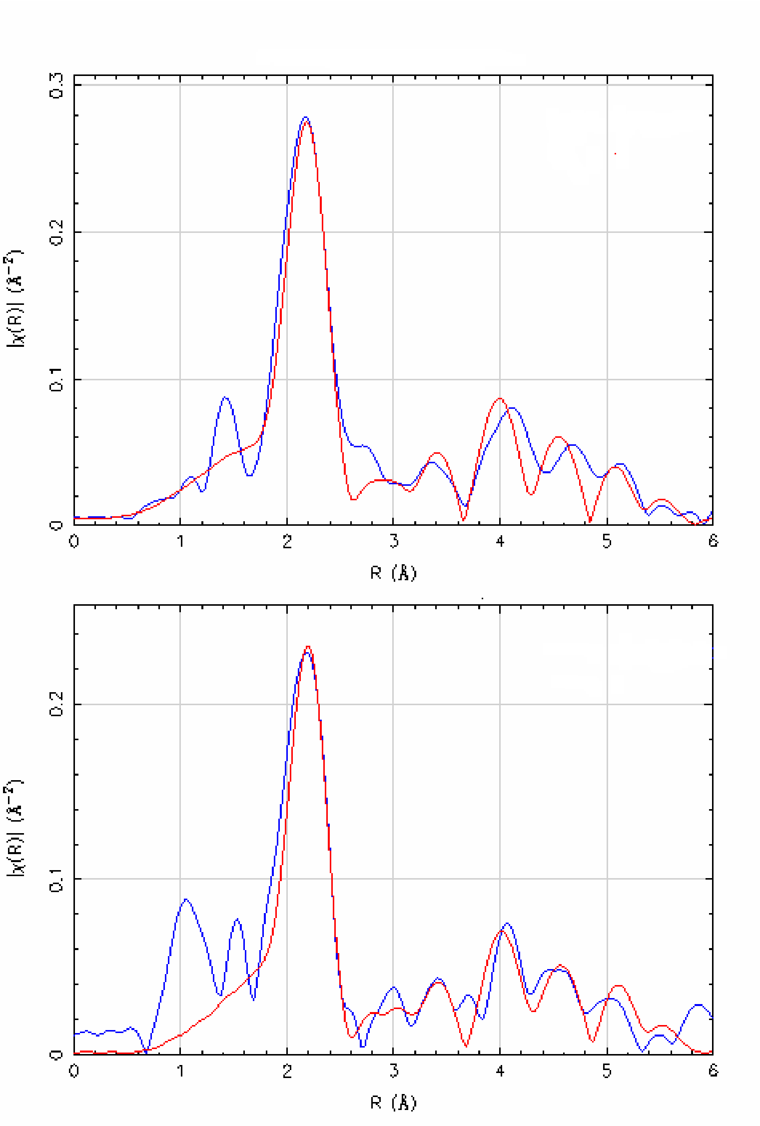

Figure 4.14: Cobalt EXAFS experiment and modeling. Blue curve displays data, while the red curve shows the best fit. Top panel corresponds to 23 $\mathring{A}$ Co; bottom panel to 65 $\mathring{A}$ Co.

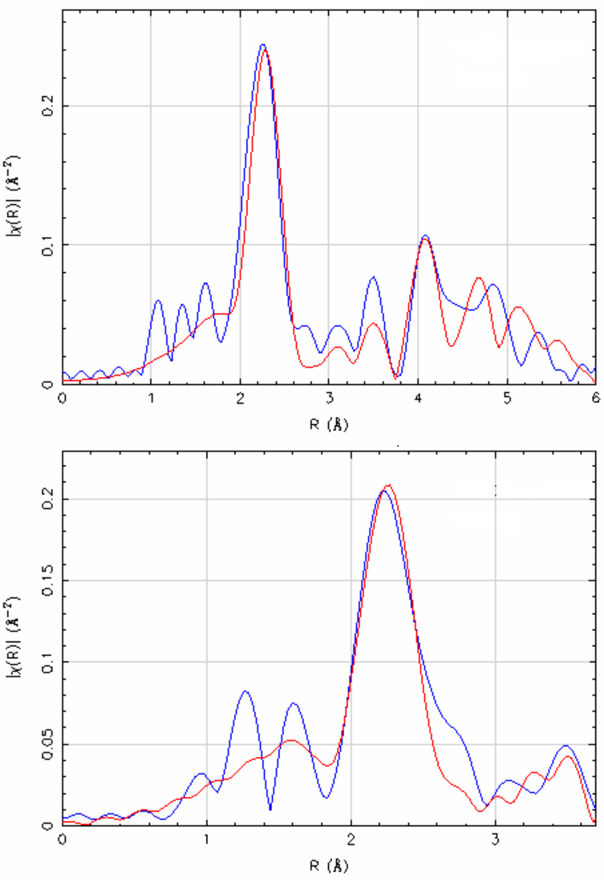

Figure 4.15: Copper EXAFS Experiment and Modeling
[Copper EXAFS experiment and modeling. Blue curve displays data, while the red curve shows the best fit. Top panel corresponds to Cu from sample S2; bottom panel to a Cu foil.]

Chapter 5

Magnetic Properties of Ultra-Thin Co|Ni Multilayered Films

In the interest of achieving perpendicular magnetic anisotropy, repeating multilayers consisting of a given thickness of Co, t, and twice that thickness of Ni, $2t$, were substituted for the pure Co ferromagnetic layers of the previous chapter. The shorthand notation used will be [t Co|$2t$ Ni] x n, where n is the number of repeats and set to twelve for purposes of increasing the signal level. The individual Co layer thicknesses, t, range from 1 to 6 $\AA$, all layers being equal within a given sample. The particular ratio of t Co:$2t$Ni was calculated to have maximal anisotropy arising from both Co|Ni interface anisotropy and from a Fermi energy shift that positions the Fermi energy close to $3d$ $x^2 - y^2$ and xy bands. With z defined to be along the surface normal, the spin-orbit interaction favors out-of-plane magnetization. For thicknesses of $t = 4$ $\AA$ or less this out-of-plane anisotropy was predicted to overcome the in-plane dipole-dipole shape anisotropy, resulting in net perpendicular magnetization [24].

5.1 Basic Structure

Two sets of evaporated samples (t ranging from 1 to 6 $\AA$), identical except for base substrate of either SiO_2 atop Si wafer or 100 $\AA$ Si_3N_4 membrane supported by Si wafer cut-out, were grown for ferromagnetic resonance/x-ray diffraction and x-ray magnetic circular dichroism studies, respectively. The former samples without a membrane were both more stable and were deposited over a wider surface on the order of cm^2, while the Si_3N_4 membrane was stability-limited to a region of mm^2. The later allowed soft x-ray (700 to 950 eV photons covering the L-edges of Co and Ni) transmission measurements to be performed for optimal dichroism data acquisition. Initial electron-yield was attempted on similar wafer samples, but the Pt caps, even thinned to 15 $\AA$, were found to attenuate the signal too greatly in comparison with the small dichroism signal arising from the thin films. Thus, transmission was found to be a far more desirable route even with the base substrate change. Additionally, two background samples were grown to contain either 39 $\AA$ Co or 78 $\AA$ Ni (corresponding to the average amounts in all the multilayers) in place of the Co|Ni multilayers.

Non-resonant diffraction performed at NSLS beam line X16B at 7.6 keV (Figure

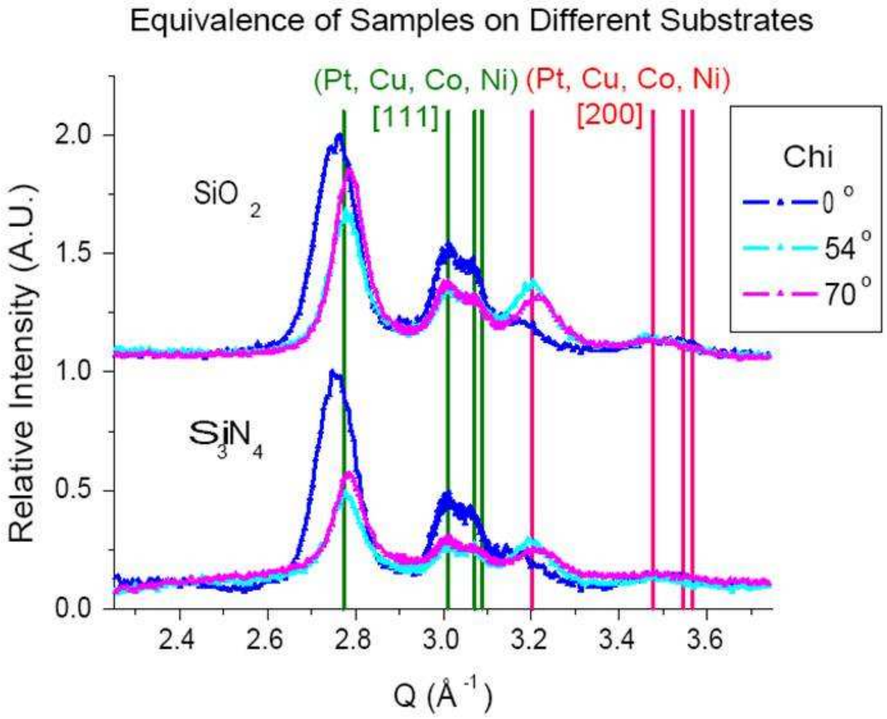

Figure 5.1: Equivalence of Co|Ni Samples Grown Atop SiO_2 and Si_3N_4 Bases

5.1) indicates that for both sets of substrate all Pt layers assume a typical, non-strained [111] textured face centered cubic structure oriented along the sample normal. The Cu, Co, and Ni also continue this textured [111] structure, very much like that of the Cu|Co|Cu series explored in the previous chapter. Ni naturally forms face centered cubic lattices in its ground state, and unstrained it has a cubic lattice just slightly shorter than that of Co, 3.524 $\AA$ compared with 3.544 $\AA$. Due to their extremely thin individual layers the Co and Ni are expected to form a single textured crystalline region sharing common bond lengths similar to that of pure Co (measured up to thicknesses of 65 $\AA$) when bordered by thicker Cu layers. Low intensity anomalous diffraction performed as a double check about the Ni K-edge at X16C on a sample with $t = 4$ $\AA$ confirms a joint Co-Ni out-of-plane [111] lattice of 3.09 $\AA^{-1}$, Figure 5.2. This is consistent with the findings for the pure Co in a similar environment as determined in chapter 4.

5.2 Hysteresis

By adjusting the height of the refocusing mirror different portions of the synchrotron beam with varying degrees of circular polarization are selected at NSLS beamline U4B. At a vertical height above the emergent beam corresponding to a 0.70

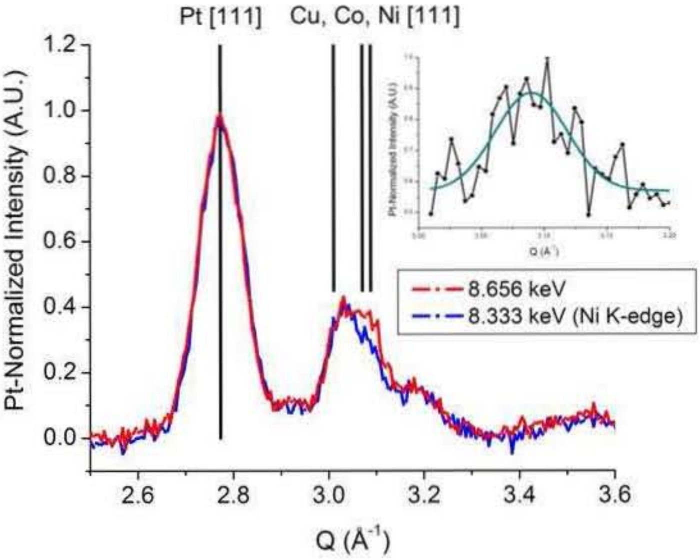

Figure 5.2: Anomalous diffraction about Ni K-edge on CoNi multilayer. The inset shows the anomalous difference. This is well fit with a single Gaussian at 3.095 ± 0.006 $\mathring{A}^{-1}$, which translates in real space to 2.030 ± 0.01 $\mathring{A}$

.

reduction in intensity, a 90 % circular beam polarization is obtained. In measuring magnetic spin to orbit moment ratios the precise polarization value isn't overly important, but for the full sum rules the linear x-ray absorption spectra (XAS) must be renormalized by the circular polarization value in order to reconstruct a situation corresponding to 100% circular polarization measurement as required for use of orbital and spin sum rules [47].

In transmission only the component of magnetization along the beam direction is detected by x-ray magnetic circular dichroism. Out-of-plane magnetization of samples normal to incident beam are an ideal geometry, but to access the in-plane magnetic features samples are rotated by 45° from the incident beam, requiring normalization by an additional factor of cosine(45°). In-plane magnetic saturation was easily obtained with an electromagnetic operated at 0.2 Amps (0.03 kG) for all multilayered samples. Perpendicular magnetization required larger magnetization and, therefore, larger applied currents. With water cooling, the field could be temporarily pulsed to 8.3 kG, but run continuously without overheating at only 6 kG. Hysteresis measurements were performed for both the Co and Ni edges by tuning energy to the maximum dichroism at the L_3 edges of each. The transmission signal collected from a photodiode placed several cm behind the sample was normalized by a gold-coated wire grid measured in electron yield, located about 0.5 meters in front of the sample. Co and Ni x-ray magnetic dichroism was performed in both in-plane and perpendicular magnetization for every sample.

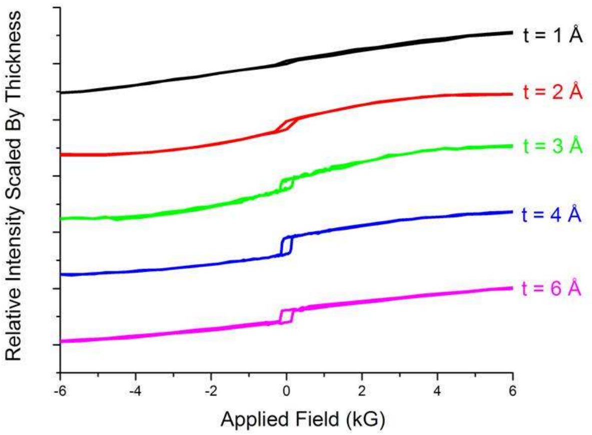

Figure 5.3: Co Multilayer Hysteresis Loops

The relative hysteresis loops are shown for the Co L_3-edge in Figure 5.3. Nickel hysteresis, identical in shape for each sample and magnetic orientation, and differing from the Co hysteresis only in total magnitude, is not explicitly shown. The magnitude of the hysteresis has been normalized by the sample thickness, and vertical shifts are used for clarity. Figure 5.3 reveals that although out-of-plane magnetic saturation became easier with decreasing sample Co|Ni multilayer thickness, except for the very thinnest sample, none of the samples actually came close to achieving perpendicular magnetic anisotropy

5.3 Structure and Roughness

Both samples from the literature [24] in which perpendicular magnetic anisotropy was achieved and our own samples consisted of polycrystalline, face centered cubic Co and Ni layers textured with the [111] orientation aligned along the sample perpendicular. However, in the literature the multilayers were grown atop [111]-textured Au grown with e-beam evaporation, while our samples were grown atop [111]-textured Cu over Pt by the NYU Kent group using a sputtering technique [25]. The observed differences in perpendicular magnetic anisotropy could then potentially be due to either differences in strain or to variations in roughness between sample sets.

Reflectivity from the thickest sample taken at 7.3 keV on NSLS beamline X16B was already used as demonstration for the specular reflectivity method in Figure 2.4. The point to notice from this Figure is that like the other multilayer thicknesses the reflectivity pattern petered out around 0.7 $\mathring{A}^{-1}$, which is not at all unexpected. Although specular reflectivity can in principle be used to determine roughnesses less than the individual layer thicknesses, the difficulty in ultra-thin films is measuring a signal far enough out in reciprocal space where changes between a layered and an

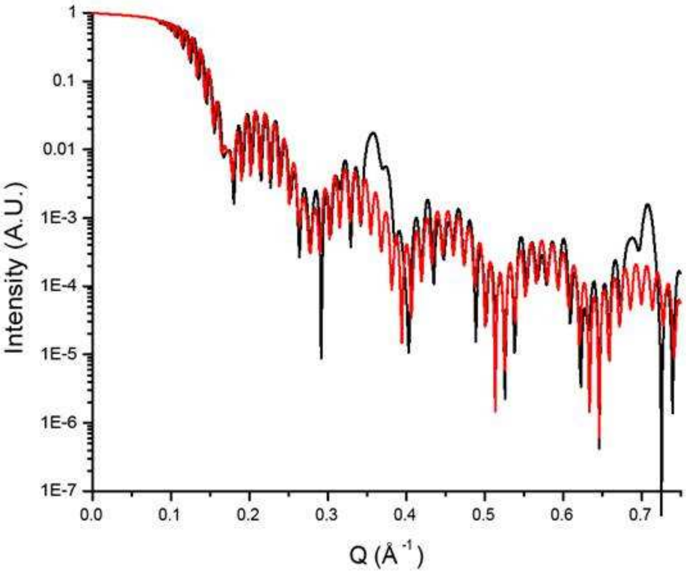

Figure 5.4: Simulated reflectivity differences for a Co|Ni multilayer (red curve) and an alloy (black curve) where Co layer thicknesses = 6 $\AA$.

alloyed sample would be observable. For example, using Parratt32 the calculated difference in a perfectly layered sample versus a complete alloy for the thickest sample, $t = 6$ $\AA$, is shown in Figure 5.4. As expected features between the two extremes are observed in the corresponding experimental measurement of Figure 2.4. However, for thinner samples the differences between layered and alloyed samples, stemming from a thinner interlayer interference, are pushed to higher Q where experimentally little reflectivity signal remains. In the case of the thinnest sample, for example, a simulation given in Figure 5.5 shows no difference would be detectable in the area of reciprocal space up to 0.7 $\AA^{-1}$. The same is true for all remaining samples up to $t = 4$ $\AA$ which is on the borderline for achieving perpendicular magnetic anisotropy. Therefore, in the samples with the most potential for perpendicular magnetic anisotropy a roughness could not be easily determined.

On the other hand, a base of [111] Au with a face centered cubic lattice of 4.0783 $\AA$ would be even less likely to epitaxially match the Co or Ni than [111] Cu with a 3.6147 $\AA$ face centered cubic lattice. In the interest of measuring structure and especially strain, directional extended x-ray absorption fine structure (EXAFS) set to preferentially probe both the in-plane and out-of-plane lattice spacings was performed on NSLS beamline X23A for the thinnest sample. The sample was placed in grazing incidence geometry with the sample normal perpendicular to and aligned with the horizontal beam polarization vector, respectively. Due to the presence of the Ni K-edge, only energies up to 624 eV beyond the Co K-edge could be probed. Regardless,

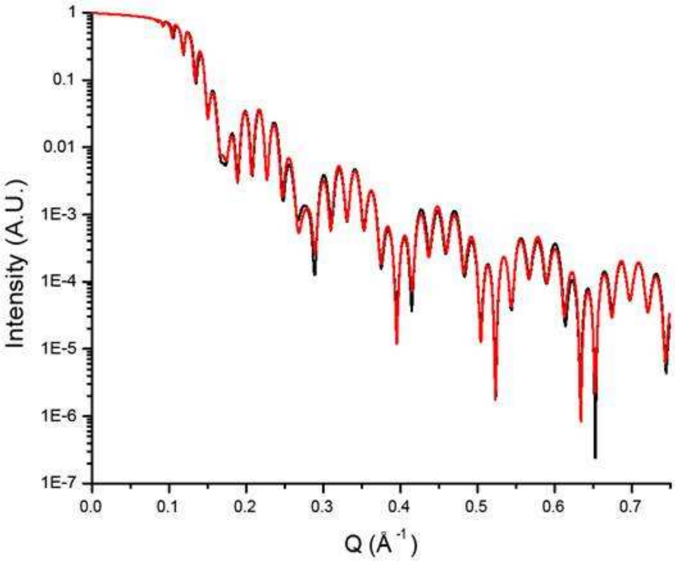

Figure 5.5: Simulated reflectivity differences for a Co|Ni multilayer (red curve) and an alloy (black curve) where Co layer thicknesses = 1 $\AA$.

a clean signal was obtained. Both the in-plane and perpendicular oriented EXAFS measurements appeared very similar, Figure 5.6. They also appeared structurally similar to the EXAFS performed in chapter 4 on trigonally strained Co samples, Figure 4.14. Together these findings suggested the use of a trigonally strain face centered cubic model, allowed to rotate in all orientations. As before it is based on fitting the in and out-of-plane [111] face centered cubic directions. Additionally, Co and Ni, with almost the same number of electrons, have very similar backscattering profiles so they can be treated on equal footing in the EXAFS model.

The EXAFS fit is shown in Figure 5.7 along with the experimental "in-plane" EXAFS data. The fit suggests that the Co (and therefore Ni) has an in-plane [111] spacing of 2.052 ± 0.019 $\AA$ and a perpendicular [111] spacing of 1.984 ± 0.043 $\AA$. These measurement certainly represent a trigonally strained structure, very similar to that of pure Co in a Cu|Co|Cu sandwich, except that the lattices are just slightly shorter. This is also expected as bulk Ni naturally has a slightly shorter face centered cubic lattice than Co. For comparison bulk [111] Co and Ni are 2.046 and 2.034 $\AA$, respectively.

5.4 Strain Model

With an idea of how the Co|Ni multilayer behaves, the resulting strain that may have on magnetic orientation can be examined. Burket *et al.* [23] defines trigonal

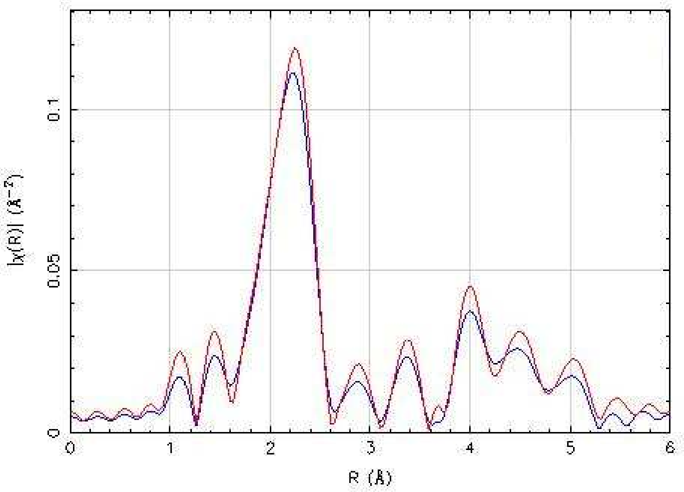

Figure 5.6: Directionally dependent Co|Ni multilayer EXAFS taken on the Co K-edge for the thinnest sample. Red curve represents the case where the beam polarization was oriented along the sample normal, blue curve the case where beam polarization was aligned with the sample plane. Both orientations appear similar, prompting the use of a powder model where the crystals are allowed to vary some in orientation.

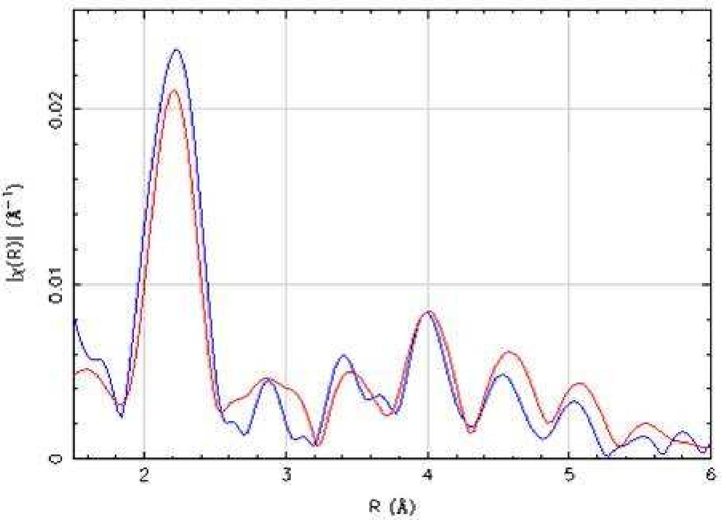

Figure 5.7: EXAFS fit of thinnest Co|Ni multilayer, red curve, compared with the experimental data, blue curve. Although not perfect, the model indicates trigonal strain is present.

strain as distortion along the [111] and [110] orientations in the case of face centered cubic structures. If $\kappa = (\frac{[110]}{[111]})^2 - 1$, then κ of 0.5 would be equal to an unstrained face centered cubic lattice. Combining the anomalous diffraction and EXAFS results the sample κ appears to be in the range of 0.55 to 0.62 (the latter taken only from EXAFS in which the out-of-plane compression tend to look more compressed than what is measured with diffraction). Even using the lower value of 0.55 this would cause the Co and Ni to favor [110] magnetization, which happens to be in-plane for our samples, by about 0.15 and 0.20 meV per layer. The multilayer magnetic anisotropy calculated by Daalderop *et al.* [24] also happens to be 0.2 meV in favor of perpendicular magnetization, which in our samples lies collinear with the [111] orientation. Add to this a slight dipole-dipole shape anisotropy also pulling the magnetization in-plane and it seems plausible that the strain could well account for the lack of perpendicular magnetic anisotropy observed. Perhaps the Cu being more epitaxially matched to the Co and Ni does a better job of inducing strain than does the Au with a larger lattice. Of course, more structural work would need to be performed on both types of samples to reach a solid conclusion whether strain was the only factor at work in the lack of perpendicular magnetic anisotropy, but these findings highlight the magnetic importance that strain, though often unmeasured, can have.

5.5 X-Ray Magnetic Circular Dichroism Processing

With our picture of uniaxial strain in mind, it would be interesting to look for any observable x-ray magnetic circular dichroism (XMCD) changes with direction and/or sample thickness. A general procedure for the magnetic measurement of the samples, however, must first be explained.

Samples magnetized along their surface plane were switched magnetically between magnetic fields held at ± 0.3 kGauss (fully saturating) during the course of each absorption scan. Perpendicularly magnetized measurements were taken at magnetic fields of ± 6 kGauss, the maximum field at which the magnetic could be sustained without overheating. Only samples St2(T) and St3(T) were fully saturated in this configuration. The Co and Ni L edges were probed over a ranges of roughly 750 to 840 and 830 to 920 eV, respectively. The transmission signal was collected by a photodiode placed several cm behind the sample and normalized by a gold-coated wire grid measured with electron yield, located several just upstream of the UHV-preserving aluminum window. Background scans were taken using Co and NI reference samples.

Repeated absorption curves were collected for improved statistics. Over time small energy shifts occurred so in order to align the samples consistently the transmission L_3 dichroism was used as a reference with its maxima defined as the nominal edge-jump corresponding Co or Ni transition energy. Transmission, however, as measured in experiment (Figure 5.8, top panel) is not a direct measure of absorption, μ, as given in equation 2.8. Yet, the natural logarithm of even a small linear offset can become an exponentially varying background once transformed into absorption. Therefore, a linear fit was obtained from the pre-edge and tail (that is, below 772 eV and above 820 eV for Co) where the dichroism vanishes. The small linear offset was then subtracted out (see Figure 5.8, second panel down).

Reference scans taken with an average amount of Co or Ni within the usual Pt, Cu structure on Si_3N_4 (for the Ni and Co regions, respectively) were aligned to the transmission pre-edge region adding offset and altering slope as required (equivalent to adding a linear offset). The scaled background (Figure 5.8, blue curve of top panel) was then used to normalize the sample transmission signal before it was transformed into μ^+ and μ^- absorption (plus and minus indicate opposite magnetization which is entirely equivalent to changing circular polarization) and scaled to match corresponding theoretical Henke absorption curves. This is shown Figure 5.8, middle panel, where green curves are Henke background. The Henke absorption edges were rounded at each transition edge with an arc tangent function mimicking a finite core-hole lifetime while still preserving the total area under the curve. Subtraction of this theoretical absorption essentially removes photoelectron transitions to the continuum, while retaining the desired transitions into the valance band.

XMCD is the difference in intensity between the μ^+ and μ^- absorption, while x-ray absorption (XAS) is equivalent to the sum of the two circular polarizations (linear absorption) minus Henke absorption. The integrated intensity of the XMCD, and the total number of valance-band transitions (XAS) are given in Figure 5.8, bottom panels. P, Q, and R values are drawn in and correspond the equations 2.17, 2.18, and 2.19. From these measured values is possible to obtain the long-range spin and orbital moments per atom if the number of 3d valance holes are known. In cases where the hole number is expected to differ from that of the pure metal values (known) the orbit to spin ratio can still be obtained. Additionally, changes in the ratio of the integrated XAS L_3:L_2 transitions, can in principle, provide local magnetic information. All the data shown in 5.8 were taken on the second to thinnest Co|Ni multilayer of $t = 2\mathring{A}$ performed using in-plane magnetization.

5.6 X-Ray Magnetic Circular Dichroism Results

The first interesting thing to do is to compare the in-plane magnetized XMCD results with in-plane ferromagnetic resonance. This can be done be using the relationship between orbital and spin moments with the Lande g-factor in equation 2.33. Additionally, ferromagnetic resonance is not element specific like XMCD. However, an effective net Lande g-factor as probed with ferromagnetic resonance, taking into account the relative proportions of Co and Ni, is given by

$$g_{\text{eff}} = \frac{M_{\text{sat}}^{\text{Co}} + 2M_{\text{sat}}^{\text{Ni}}}{\frac{M_{\text{sat}}^{\text{Co}}}{g_{\text{Co}}} + 2\frac{M_{\text{sat}}^{\text{Ni}}}{g_{\text{Ni}}}}. \tag{5.1}$$

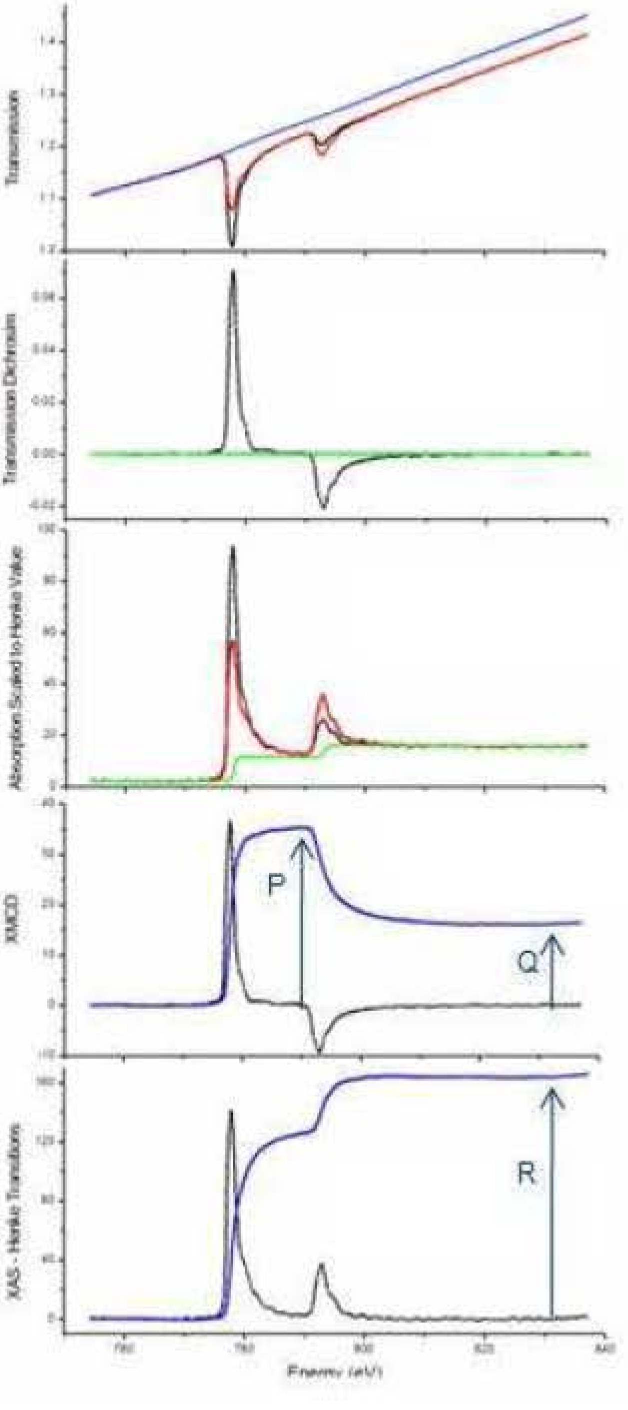

Figure 5.8: Outline of steps required to obtain the full sum rules from XMCD data.

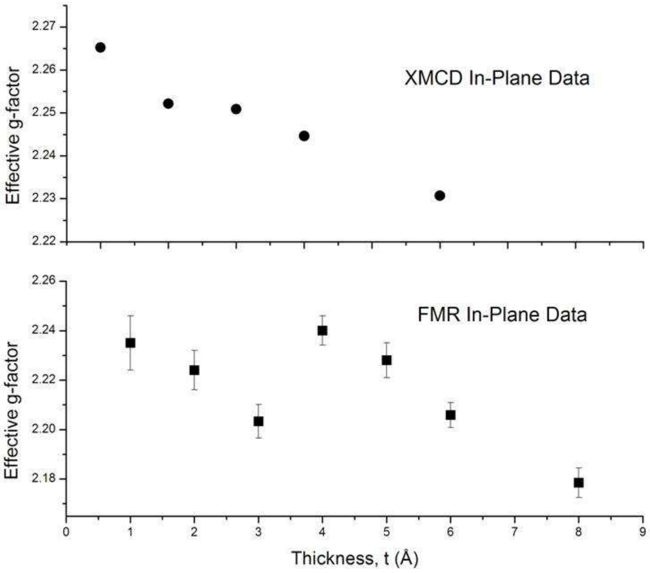

Figure 5.9: Comparison of XMCD and FMR in-plane Lande g-values.

The magnetic saturation of the Co and Ni have been measured by the NYU Kent group as 1408 $\frac{\text{emu}}{\text{cm}^2}$ for the Co, and 416 $\frac{\text{emu}}{\text{cm}^2}$ for the Ni. The Ni XMCD was weaker than the Co as expected, so the average Ni in-plane Lande g-factor of 2.244 was used for all sample thicknesses. Putting in the measured Co g-values as a function of thickness produces the results of Figure 5.9.

While the XMCD and ferromagnetic resonance measurements aren't in complete agreement about the magnitude of the g-value, the trends observed as a function of thickness are similar. In both cases there appears to be an inflection point around the thickness of $t = 3\mathring{A}$. Additionally, the measured g-value increases with declining sample thickness. Until further structural studies are conducted on these samples it is unclear if changing structure or changing interface to bulk ratio is responsible for this trend.

Returning to the g-values of the pure Co, differences in spin and orbital moments as a function of magnetic direction may be examined. The working assumption is that spin moments do not depend greatly on the direction of an applied saturating magnetic field, but orbital moments might well experience anisotropic changes being more dependent on three dimensional structure and orientation. In-plane and perpendicular magnetization g-values are plotted together in Figure 5.10. Both orientations show an increase with diminishing sample thickness, but the effect is particularly strong when the magnetization is oriented along the sample normal. Although structural changes as a function of thickness can't be ruled out. If one uses the findings of the very similarly structured and textured Cu|Co|Cu as a guide, structural changes

Table 5.1: Co Multilayer Moments for $t = 2$ Å

Results for $t = 2$Å	In-Plane Co	Perpendicular Co
Lande g-factor	2.257 ± 0.02	2.284 ±0.01
Spin Moment	1.613	1.636
Orbital Moment	0.2039	0.2382

Table 5.2: Co Multilayer Moments for $t = 3$ Å

Results for $t = 2$Å	In-Plane Co	Perpendicular Co
Lande g-factor	2.262 ± 0.02	2.274 ±0.01
Spin Moment	1.696	1.568
Orbital Moment	0.2222	0.2146

could not be detected for ferromagnetic thicknesss of 12 to 65 Å. Treating the Co and Ni ultra-thin layers as a single ferromagetic unit, this range of thicknesses is nearly equivalent to Co|Ni mutlilayers with t of 1 and 2 Å. Given the sharp increase in g-values for the thinnest sample, this implies the change might be a result of increased Co|Ni interface and associated perpendicular magnetic anisotropy preference rather than from structural changes alone.

Finally, full sum rules were performed on multilaters with $t = 2$ and 3 Å in which full magnetic saturation was achieved in both in-plane and along the perpendicular magnetization with a 6 kG magnetic field. The results of extracted spin and orbital moments are given in Tables 5.1 and 5.2, assuming a bulk 3d hole value of 2.45 for the Co.

The measurement is not precise enough to detect any differences in spin or orbital moments as a function of magnetic direction, but they do allow a rough quantification whether the spin or orbital moment is likely to be the primary cause of the increased orbit to spin ratio ($\prec$ g-value). Bulk face centered cubic Co has a spin moment of 1.56 μ_L [15], and reported bulk g-value of 2.15 [22]. Together, these would peg the bulk orbital moment at 0.1 μ_B. Comparison with the results in Tables 5.1 and 5.2 it appears the orbital moment is enhanced, while the spin moment is much more similar to bulk. Of course, the total number of holes could be reduced some by the presence of Ni, but it would be hard to account for such large Lande g-values based solely on a 3d hole depletion.

5.7 Summary

Combining limited structural characterization, based in part on the findings of the similarly structured Cu|Co|Cu samples of the previous chapter, with element specific magnetic measurement has brought out several new correlations. The lack of predicted perpendicular magnetic anisotropy may well be explained by induced trigonal strain that theoretically should increase the preference for [110], in-plane

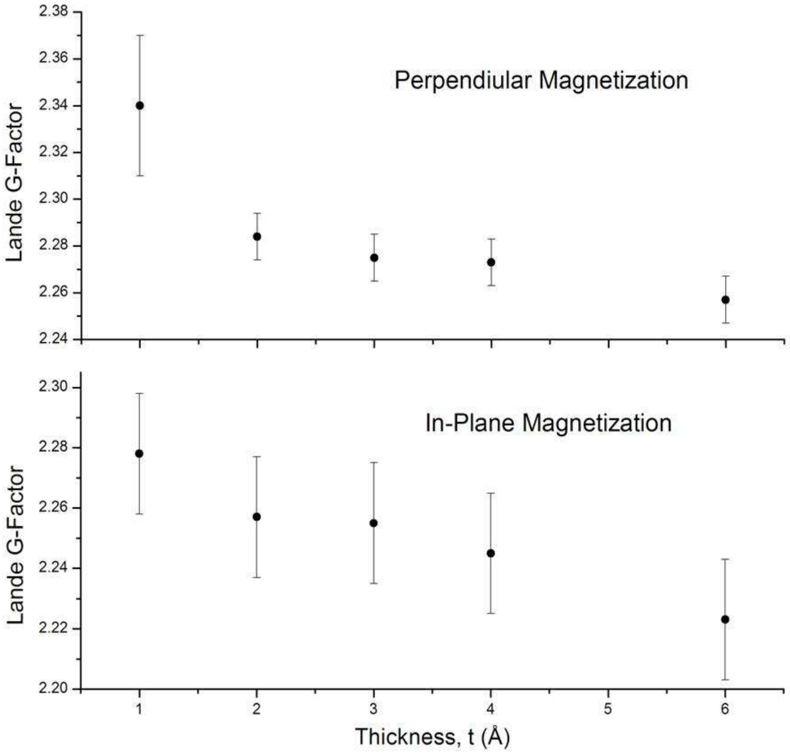

Figure 5.10: Comparison of In-Plane and Perpendicular Magnetization on Co|Ni Multilayers

magnetization. The strain measured was by no means small being compressed along the sample normal by approximately 0.3 %, and expanded along the [110] direction by 1 %.

From ferromagnetic resonance it was known ahead of time that decreasing the ferromagnetic thickness lead to increased orbit to spin ratios. The X-ray magnetic circular dichroism was able to show that the effect was enhanced along the sample perpendicular, and the primary source of the increased Lande g-factors appears to come from an enhanced orbital moment. This could again be tied into structure if more detailed structural measurement were to be performed.

In all cases the magnetism and structure are intimately related. In order to fully understand the magnetic processes, detailed structural characterization, although not easy, would be highly recommended.

Chapter 6

Summary of Accomplishments

6.1 Development of Anomalous Diffraction for Interference Applications

Interlayer interference was found to have a significant impact on ultra-thin film diffraction, even if the film was polycrystalline and broken into crystallites. This lead to the development of Multi-wavelength Overlapping and Interfering Diffraction Separation (MOIDS) which could account for and separate the anomalous diffraction of the pure material and its interference(s). The beauty of the technique is that it could be applied to any diffraction pattern, from ultra-thin films to core-shell nanoparticles. No *a priori* knowledge of spatial distribution is required. The only requirement is that the constituent materials and the value of their scattering factors as a function of photon energy are known.

The method proved to be robust and was successfully applied to separate diffraction profiles from overlapping Pt, Cu, and Co ultra-thin film layers of 12 to 100 $\AA$ thickness. Experimentally, there were not enough energy-based diffraction scans taken in order to separate the Co from the Co-Cu interference directly. With additional energies a full MOIDS reconstruction of an ultra-thin layer sample is planned as a proof of principle.

Even with a limited number of anomalous diffraction scans interference terms were separated from the pure Bragg peaks by careful fitting of the interference terms. The full width half maximum of the extracted peak serves as a good indicator of whether an accurate extraction took place. If the interference term is overly dominant the width of the pure peak becomes compresses relative to what thickness-dependent Debye broadening dictates.

Using the anomalous procedure described the structure of ultra-thin Co layers buried between thicker [111] face centered cubic Cu layers was determined to be trigonally strained face centered cubic. The in-plane [111] lattice was determined to be expansively strained to 2.074 ± 0.01 $\AA$, while the perpendicular [111] lattice was compressed to 2.033 ± 0.01 $\AA$. Using these two measurement, plus the assumption of in-plane homogeneity, a three dimensional model locating each constituent atom was constructed and tested with EXAFS. The uncertainty of the anomalous diffraction rivaled that of EXAFS and provided additional information about the sample texturing. To the knowledge of this author this is the first, element specific structural characterization of buried, polycrystalline Co ultra-thin films within the Cu|Co|Cu configuration.

6.2 Spin-Torque, Ultra-Thin Cobalt Structure

The structure of the ultra-thin Co layers described above was found not to vary as a function of thickness within experimental uncertainty of ± 0.01 $\AA$ for Co thicknesses of 12 to 65 $\AA$. This finding means that the ferromagnetic resonance procedure of varying the ferromagnetic thickness in order to study the interface-dependent Gilbert damping and surface anisotropy was indeed valid for these samples.

The increased orbit to spin magnetic moments obtained by ferromagnetic resonance for all ultra-thin film Co thicknesses measured can, therefore, be correlated with the induced trigonal strain. This in turn has implications in tailoring future spin-torque devices since an increase of spin-orbit coupling has the tendency to increase the amount of intrinsic magnetic damping.

6.3 Cobalt | Nickel Multilayer Magnetic Correlation with Structure

Using the general structure of the ultra-thin Co as a guide, the structure of the Co|Ni multilayers was determined using EXAFS and diffraction. Like the Co spin-torque samples the Co|Ni was found to trigonally strain with the in-plane [110] lattice expanded by 0.3%, and the perpendicular [111] spacing compressed by 1%. These strains were compared to theoretical predictions on the preferential magnetization of trigonally strain Co and Ni films [23], and the preference for in-plane magnetization nearly matched the preference for perpendicular magnetic anisotropy arising for the multilayer interfaces as predicted by [24]. Therefore, this could well account for the lack of observable perpendicular magnetic anisotropy. It also underscores the importance that strain-induced changes can have on magnetic anisotropy, even for polycrystalline films.

Using x-ray magnetic circular dichroism it was also determined that increase in orbital moments, rather than changes in spin moments, appear to have the most significant impact on the observed Lande g-factor increase over bulk. Like the Co samples, this increase in orbital moment likely originates from the strain-induced trigonal strain, and has implications for intrinsic magnetic damping.

Lande g-factors were also found to increase more along the sample perpendicular than in-plane. Assuming that net spin moments under the condition of magnetic saturation are not dependent on the direction, this means that for each sample a larger out-of-plane orbital moment was observed than in-plane. Additionally, an increase in the Lande g-factor with decreasing sample thickness illustrates the tendency of the ultra-thin films to gain preference for perpendicular magnetic anisotropy as predicted [24]. If the lack of structural thickness-dependence for the Co films of similar thickness serves as model, then the Co|Ni increased perpendicular Lande g-factor enhancement could be attributed to an interface effect.

Bibliography

[1] I. Zutic, J. Fabian, and S. Das Sarma. Spintronics: Fundamentals and applications. *Reviews of Modern Physics*, 76(2):323, 2004.

[2] J. C. Slonczewski. Current-driven excitation of magnetic multilayers. *Journal of Magnetism and Magnetic Materials*, 159(1-2):L1–L7, 1996.

[3] L. Berger. Emission of spin waves by a magnetic multilayer traversed by a current. *Physical Review B*, 54(13):9353–9358, Oct 1996.

[4] R. Urban, B. Heinrich, G. Woltersdorf, K. Ajdari, K. Myrtle, J. F. Cochran, and E. Rozenberg. Nanosecond magnetic relaxation processes in ultrathin metallic films prepared by mbe. *Physical Review B*, 65(2):020402, Dec 2001.

[5] S. I. Kiselev, J. C. Sankey, I. N. Krivorotov, N. C. Emley, R. J. Schoelkopf, R. A. Buhrman, and D. C. Ralph. Microwave oscillations of a nanomagnet driven by a spin-polarized current. *Nature*, 425(6956):380–383, Sept 2003.

[6] I. N. Krivorotov, N. C. Emley, J. C. Sankey, S. I. Kiselev, D. C. Ralph, and R. A. Buhrman. Time-Domain Measurements of Nanomagnet Dynamics Driven by Spin-Transfer Torques. *Science*, 307(5707):228–231, 2005.

[7] A. A. Kovalev, A. Brataas, and G. E. W. Bauer. Spin transfer in diffusive ferromagnet˘normal metal systems with spin-flip scattering. *Physical Review B*, 66(22):224424, Dec 2002.

[8] R. Arias and D. L. Mills. Extrinsic contributions to the ferromagnetic resonance response of ultrathin films. *Physical Review B*, 60(10):7395–7409, Sep 1999.

[9] G. Bochi, O. Song, and R. C. O'Handley. Surface magnetoelastic coupling coefficients of single-crystal fcc co thin films. *Physical Review B*, 50(3):2043–2046, Jul 1994.

[10] N. Majlis. *The Quantum Theory of Magnetism.* World Scientific, 2000.

[11] A. J. Freeman and R. E. Watson. Theory of direct exchange in ferromagnetism. *Physical Review*, 124(5):1439–1454, Dec 1961.

[12] R. Shankar. *Principles of Quantum Mechanics.* Plenum Press, second edition, 1994.

[13] G. H. O. Daalderop, P. J. Kelly, and M. F. H. Schuurmans. Magnetic anisotropy of a free-standing co monolayer and of multilayers which contain co monolayers. *Physical Review B*, 50(14):9989, Oct 1994.

[14] D. Bagayoko, A. Ziegler, and J. Callaway. Band structure of bcc cobalt. *Physical Review B*, 27(12):7046–7049, Jun 1983.

[15] D. G. Laurent, J. Callaway, J. L. Fry, and N. E. Brener. Band structure, fermi surface, compton profile, and optical conductivity of paramagnetic chromium. *Physical Review B*, 23(10):4977–4987, May 1981.

[16] G. van der Laan. Magnetic linear x-ray dichroism as a probe of the magnetocrystalline anisotropy. *Physical Review Letters*, 82(3):640–643, Jan 1999.

[17] P. Bruno. Tight-binding approach to the orbital magnetic moment and magnetocrystalline anisotropy of transition-metal monolayers. *Physical Review B*, 39(1):865–868, Jan 1989.

[18] J. Stohr. Exploring the microscopic origin of magnetic anisotropies with x-ray magnetic circular dichroism (xmcd) spectroscopy. *Journal of Magnetism and Magnetic Materials*, 200(1-3):470–497, Oct 1999.

[19] V. Iota, J-H. P. Klepeis, C-H. Yoo, J. Lang, D. Haskel, and G. Srajer. Electronic structure and magnetism in compressed 3d transition metals. *Applied Physics Letters*, 90:042505, Jan 2007.

[20] R. Sabirianov. Magnetic anisotropy and anisotropic ballistic conductance of thin magnetic wires. *Journal of Magnetism and Magnetic Materials*, 300(1):136–139, May 2006.

[21] M. A. Zimmler, B. Özyilmaz, W. Chen, A. D. Kent, J. Z. Sun, M. J. Rooks, and R. H. Koch. Current-induced effective magnetic fields in co/cu/co nanopillars. *Physical Review B*, 70(18):184438, 2004.

[22] J-M. L. Beaujour, J. H. Lee, A. D. Kent, K. Krycka, and C-C. Kao. Magnetization damping in ultrathin polycrystalline co films: Evidence for nonlocal effects. *Physical Review B*, 74(21):214405, 2006.

[23] T. Burkert, O. Eriksson, P. James, S. I. Simak, B. Johansson, and L. Nordström. Calculation of uniaxial magnetic anisotropy energy of tetragonal and trigonal fe, co, and ni. *Physical Review B*, 69(10):104426, 2004.

[24] G. H. O. Daalderop, P. J. Kelly, and F. J. A. den Broeder. Prediction and confirmation of perpendicular magnetic anisotropy in co|ni multilayers. *Physical Review Letters*, 68(5):682–685, Feb 1992.

[25] J-M. L. Beaujour, W. Chen, K. Krycka, C-C. Kao, J. Z. Sun, and A. D. Kent. Ferromagnetic resonance study of sputtered co|ni multilayers. *European Physical Journal B*, (in press), Mar 2007.

[26] J. Als-Nielsen and D. McMorrow. *Elements of Modern X-Ray Physics.* Wiley Publishing, 2001.

[27] J. J. Sakurai. *Modern Quantum Mechanics.* Addison-Wesley Publishing, 1994.

[28] B. L. Henke, E. M. Gullikson, and J. C. Davis. X-ray interactions: Photoabsorption, scattering, transmission, and reflection at E=50–30,000 eV, Z=1–92. *Atomic Data and Nuclear Data Tables*, 54:181–342, 1993.

[29] B. L. Henke, 1996. The data set of Henke *et al.* [28] can be obtained on Internet using `http://www-cxro.lbl.gov/optical_constants`.

[30] F. E. Low. Scattering of light of very low frequency by systems of spin . *Physical Review*, 96(5):1428–1432, Dec 1954.

[31] M. Gell-Mann and M. L. Goldberger. Scattering of low-energy photons by particles of spin . *Physical Review*, 96(5):1433–1438, Dec 1954.

[32] P. M. Platzman and N. Tzoar. Magnetic scattering of x rays from electrons in molecules and solids. *Physical Review B*, 2(9):3556–3559, Nov 1970.

[33] F. De Bergevin and M. Brunel. Observation of magnetic superlattice peaks by x-ray diffraction on an antiferromagnetic nio crystal. *Physics Letters A*, 39(2):141–142, April 1972.

[34] F. de Bergevin and M. Brunel. Diffraction of x-rays by magnetic materials. i. general formulae and measurements on ferro- and ferrimagnetic compounds. *Acta Crystallographica Section A*, 37(3):314–324, May 1981.

[35] M. Blume and Doon Gibbs. Polarization dependence of magnetic x-ray scattering. *Physical Review B*, 37(4):1779–1789, Feb 1988.

[36] S. W. Lovesey and S. P. Collins. *X-Ray Scattering and Absorption by Magnetic Materials.* Oxford Science Publications, 1996.

[37] K. Namikawa, M. Ando, T. Nakajima, and H. Kawata. X-ray resonance magnetic scattering. *Journal of the Physical Society of Japan*, 54(11):4099, Aug 1985.

[38] B. T. Thole, G. van der Laan, and G. A. Sawatzky. Strong magnetic dichroism predicted in the $m_{4,5}$ x-ray absorption spectra of magnetic rare-earth materials. *Physical Review Letters*, 55(19):2086–2088, Nov 1985.

[39] Gerrit van der Laan, Bernard T. Thole, George A. Sawatzky, Jeroen B. Goedkoop, John C. Fuggle, Jean-Marc Esteva, Ramesh Karnatak, J. P. Remeika, and Hanna A. Dabkowska. Experimental proof of magnetic x-ray dichroism. *Physical Review B*, 34(9):6529–6531, Nov 1986.

[40] G. Schütz, W. Wagner, W. Wilhelm, P. Kienle, R. Zeller, R. Frahm, and G. Materlik. Absorption of circularly polarized x rays in iron. *Physical Review Letters*, 58(7):737–740, Feb 1987.

[41] Doon Gibbs, D. R. Harshman, E. D. Isaacs, D. B. McWhan, D. Mills, and C. Vettier. Polarization and resonance properties of magnetic x-ray scattering in holmium. *Physical Review Letters*, 61(10):1241–1244, Sep 1988.

[42] J. P. Hannon, G. T. Trammell, M. Blume, and Doon Gibbs. X-ray resonance exchange scattering. *Physical Review Letters*, 61(10):1245–1248, Sep 1988.

[43] D. B. McWhan, C. Vettier, E. D. Isaacs, G. E. Ice, D. P. Siddons, J. B. Hastings, C. Peters, and O. Vogt. Magnetic x-ray-scattering study of uranium arsenide. *Physical Review B*, 42(10):6007–6017, Oct 1990.

[44] C. Kao, J. B. Hastings, E. D. Johnson, D. P. Siddons, G. C. Smith, and G. A. Prinz. Magnetic-resonance exchange scattering at the iron l_{II} and l_{III} edges. *Physical Review Letters*, 65(3):373–376, Jul 1990.

[45] C. T. Chen, F. Sette, Y. Ma, and S. Modesti. Soft-x-ray magnetic circular dichroism at the $L_{2,3}$ edges of nickel. *Physical Review B*, 42(11):7262–7265, Oct 1990.

[46] B. T. Thole, P. Carra, F. Sette, and G. van der Laan. X-ray circular dichroism as a probe of orbital magnetization. *Physical Review Letters*, 68(12):1943–1946, Mar 1992.

[47] C. T. Chen, Y. U. Idzerda, H.-J. Lin, N. V. Smith, G. Meigs, E. Chaban, G. H. Ho, E. Pellegrin, and F. Sette. Experimental confirmation of the x-ray magnetic circular dichroism sum rules for iron and cobalt. *Physical Review Letters*, 75(1):152–155, Jul 1995.

[48] Sarnjeet S. Dhesi, Gerrit van der Laan, Esther Dudzik, and Alexander B. Shick. Anisotropic spin-orbit coupling and magnetocrystalline anisotropy in vicinal co films. *Physical Review Letters*, 87(6):067201, Jul 2001.

[49] S. S. Deshi, G. van der Laan, and E. Dudzik. Determining element-specific magnetocrystalline anisotropies using x-ray magnetic linear dichroism. *Applied Physics Letters*, 80(9):1613–1615, Mar 2002.

[50] J. Kirz, D. T. Attwood, B. L Henke, M. R. Howells, K. D. Kennedy, K-J. Kim, J. B. Kortright, R. C. Perera, P. Pianetta, J. C. Riordan, J. H. Scofield, G. L.

Sradling, A. C. Thompson, J. H. Underwood, D. Vaughan, G. P. Williams, and H. Winick. *X-Ray Data Booklet.* Center for X-Ray Optics, 1986.

[51] P. James, O. Eriksson, B. Johansson, and I. A. Abrikosov. Calculated magnetic properties of binary alloys between fe, co, ni, and cu. *PPhysical Review B*, 59(1):419–430, Jan 1999.

[52] G. Van der Laan. Sum rule practice. *Journal of Synchrotron Radiation*, 6(3):694–695, May 1999.

[53] B. E. Warren. *X-Ray Diffraction.* Dover Publications, Inc., 1990.

[54] L. G. Parratt. Surface studies of solids by total reflection of x-rays. *Physical Review*, 95(2):359–369, Jul 1954.

[55] C. Braun. *Parratt32 or The Reflectivity Tool.* Hann-Meitner-Institute, Berlin, 1997-1999.

[56] B. Ravel and M. Newville. *ATHENA*, *ARTEMIS*, *HEPHAESTUS*: data analysis for X-ray absorption spectroscopy using *IFEFFIT*. *Journal of Synchrotron Radiation*, 12(4):537–541, Jul 2005.

[57] J. J. Rehr and R. C. Albers. Theoretical approaches to x-ray absorption fine structure. *Reviews of Modern Physics*, 72(3):621–654, Jul 2000.

[58] Dale E. Sayers, Edward A. Stern, and Farrel W. Lytle. New technique for investigating noncrystalline structures: Fourier analysis of the extended x-ray¯absorption fine structure. *Physical Review Letters*, 27(18):1204–1207, Nov 1971.

[59] M. Newville. Ifeffit : interactive xafs analysis and feff fitting. *Journal of Synchrotron Radiation*, 8(2):322–324, Mar 2001.

[60] C. Kittel. *Introduction to Solid State Physics.* John Wiley and Sons Inc., 7th edition, 1996.

[61] Michael Farle. Ferromagnetic resonance of ultrathin metallic layers. *Reports on Progress in Physics*, 61(7):755–826, 1998.

[62] A. Guinier. *X-Ray Diffraction In Crystals, Imperfect Crystals, and Amorphous Bodies.* Dover Publications, Inc., 1994.

[63] J. Karle. Some developments in anomalous dispersion for the structural investigation of macromolecular systems in biology. *International Journal of Quantum Chemistry: Quantum Biology Symposium*, 7:357–367, 1980.

[64] W. A. Hendrickson. Analysis of protein structure from diffraction measurement at multiple wavelengths. *Transactions of the American Crystallography Association*, 21:11, 1985.

[65] Y. U. Idzerda, W. T. Elam, B. T. Jonker, and G. A. Prinz. Strucuture determination of metastable cobalt films. *Physical Review Letters*, 62(21):2480, 1989 May.